



저작자표시-비영리-변경금지 2.0 대한민국

이용자는 아래의 조건을 따르는 경우에 한하여 자유롭게

- 이 저작물을 복제, 배포, 전송, 전시, 공연 및 방송할 수 있습니다.

다음과 같은 조건을 따라야 합니다:



저작자표시. 귀하는 원저작자를 표시하여야 합니다.



비영리. 귀하는 이 저작물을 영리 목적으로 이용할 수 없습니다.



변경금지. 귀하는 이 저작물을 개작, 변형 또는 가공할 수 없습니다.

- 귀하는, 이 저작물의 재이용이나 배포의 경우, 이 저작물에 적용된 이용허락조건을 명확하게 나타내어야 합니다.
- 저작권자로부터 별도의 허가를 받으면 이러한 조건들은 적용되지 않습니다.

저작권법에 따른 이용자의 권리는 위의 내용에 의하여 영향을 받지 않습니다.

이것은 [이용허락규약\(Legal Code\)](#)을 이해하기 쉽게 요약한 것입니다.

[Disclaimer](#)

Ph.D. DISSERTATION

**Effect of photo-bias stress and crystallinity of
channel layer on the instability of In-Zn-O
thin film transistors**

by

Seungha Oh

February 2015

**Department of Materials Science and Engineering
College of Engineering
Seoul National University**

Effect of photo-bias stress and crystallinity of channel layer on the instability of In-Zn-O thin film transistors

Advisor : Prof. Hyeong Joon Kim

By
Seungha Oh

A thesis submitted to the Graduate Faculty of Seoul National University in partial fulfillment of the requirements for the Degree of Doctor of Philosophy
Department of Materials Science and Engineering

February 2015

Approved
by

Chairman of Advisory Committee : Cheol Seong Hwang

Vice-chairman of Advisory Committee : Hyeong Joon Kim

Advisory Committee : Ho Won Jang

Advisory Committee : Myung Soo Huh

Advisory Committee : Jae Kyeong Jeong

Abstract

In_2O_3 -based oxide thin film transistors (TFTs) have been studied extensively as switching devices in active-matrix (AM) liquid crystal displays (LCDs), organic light emitting diodes (OLEDs) and flexible displays on account of their considerably high field-effect mobility ($> 30 \text{ cm}^2/\text{Vs}$), high electrical uniformity over a large substrate size, and low processing temperature. The fabrication of In_2O_3 -based oxide TFTs with high mobility has often been reported, but little is known about the photo-bias instability of the resulting In-Zn-O (IZO) TFTs. Moreover, the effect of the crystalline structure on the photo-bias instability of metal oxide TFTs has not been studied.

This dissertation discusses the photo-bias instability of IZO TFT with various In contents and the effect of crystallinity of channel layer on the instability.

In this dissertation, the fabrication of high performance TFTs with an IZO channel layer was carried out using a co-sputtering method. The effect of the indium content on the negative bias illumination stress (NBIS) instability as well as the device performance of the IZO TFTs was investigated. The field-effect mobility and sub-threshold swing were much improved with increasing In fraction; $41.0 \text{ cm}^2/\text{Vs}$ and 0.2 V/decade , respectively, at 85 at.%In, compared to $1.1 \text{ cm}^2/\text{Vs}$ and 2.4 V/decade of ZnO TFTs. The improvement of the transfer characteristic was well

consistent with Hall measurement result of the IZO films. Excepting 16 at.%In, electron concentration and Hall mobility was increased with increasing In fraction. Overall, the electron concentration and Hall mobility had dependence on In fraction and oxygen vacancy (V_O) concentration, but in the films with 16 at.%In the electrical and structural properties of In-doped ZnO was significant. In the result of NBIS instability, an anomalous behavior was observed, attributed to an abrupt polycrystalline to amorphous phase transition. The negative threshold voltage (V_{th}) shift was intensified with increasing In fraction when it was lower than 60 at.%, where the polycrystalline structure was maintained. In particular, columnar-type grain boundaries facilitated the electric field induced migration of ionized vacancies (V_O^{2+}), so the expansion of grain boundary area induced by decrease in grain size degraded the NBIS instability. On the other hand, the NBIS instability in the V_{th} shift was minimized near an In fraction of 75 at.%, which is related to a polycrystalline to amorphous phase transition. It suggests that the migration of photo-excited V_O^{2+} defects also plays an important role in determining the overall V_{th} instability, and the absence of grain boundary defects and columnar structure is desirable for securing the photo-bias stability of the IZO TFTs. Further increases in the In fraction deteriorated the reliability due to the increased vacancy concentration.

The relationship between the crystalline structure of a channel layer and V_{th} instability was examined again using stretched exponential formula. Activation

energies (E_r) of temperature dependent V_{th} shift were evaluated for three devices including a poly-crystalline and amorphous IZO channel of which In content was 52 and 77 at.%. The calculated E_r value of the poly-crystalline TFT was 1.40 eV, whereas the amorphous TFT exhibited larger E_r values of 2.04 eV. The result indicated the transition from a poly-crystalline to amorphous structure induced the increase in migration energy barrier. Moreover, the E_r difference of 0.64 eV between the devices was attributed to the different migration paths of the V_O^{2+} defects, suggesting that the presence of grain boundary defects deteriorates the bias temperature stress-induced V_{th} instability of metal oxide TFTs. On the other hand, the energy barrier (~ 0.75 eV) for the recovery process was independent of the crystalline structure. This recovery behavior was attributed to a neutralization process ($V_O^{2+} + 2e^- \rightarrow V_O$).

Keywords : Indium Zinc Oxide (IZO), thin film transistors (TFTs), photo-bias stability, negative bias illumination stress (NBIS), grain boundary, crystalline structure, In content, sputtering

Student ID : 2009-20617

Seungha Oh

Table of Contents

Abstract	i
Table of Contents	iv
List of Tables	vii
List of Figures	viii
Chapter 1. Introduction	1
1.1 Overview.....	1
Chapter 2. Literature Review	7
2.1 Metal oxide semiconductor.....	7
2.1.1 Metal oxide semiconductor materials	7
2.1.1.1 Binary oxide semiconductors	7
2.1.1.2 Multi component oxide semiconductors	14
2.1.2 Electronic structure and carrier transport mechanism in oxide semiconductors	24
2.2 Thin film transistors.....	34
2.2.1 Device structures.....	34
2.2.2 Operation of oxide TFT	38

2.2.3 Characteristic parameters of transistor	42
2.3 Instability of oxide TFTs	48
2.3.1 Instability under stress measurement	48
2.3.2 Origin of instability	57
2.3.3 Stretched exponential equation	64

Chapter 3. Anomalous behavior of negative bias illumination stress instability in an indium zinc oxide transistor: a cation combinatorial approach.....66

3.1 Introduction.....	66
3.2 Experimental.....	69
3.3 Electrical properties of IZO films and TFTs	72
3.3 Electrical properties of IZO films and TFTs	72
3.4 NBIS instability of IZO TFTs	78
3.5 Chemical state of IZO films	81
3.6 Crystal structure of IZO films	89
3.7 Microstructure of IZO films	96
3.8 Quantitative analysis for ΔV_{th}	100
3.9 Summary	105

Chapter 4. Dynamics of negative bias thermal stress-induced threshold voltage shifts in indium zinc oxide transistors: impact of the crystalline structure on the activation energy barrier	106
4.1 Introduction.....	106
4.2 Experimental.....	110
4.3 Electrical properties of IZO TFTs	113
4.4 Activation energy for the negative V_{th} displacement of IZO TFTs...	116
4.5 Activation energy for the recovery process	125
4.6 Summary.....	134
Chapter 5. Conclusions	136
Bibliography	139
List of publications	152
Abstract (in Korean)	159

List of Tables

Table. 1.1.1 Typical properties of various n-type oxide films.

Table. 1.1.2 Comparison of oxide semiconductor, a-Si and poly-Si TFTs.

Table. 2.1.1 Summary of physical properties of In_2O_3 and ZnO.

Table. 2.1.2 Comparison of the characteristics of conventional amorphous semiconductor and AOSs.

Table. 3.3.1 Electrical characteristics of the TFTs based on $\text{In}_x\text{Zn}_{1-x}$ films with different In contents.

Table 3.5.1 Comparison of portions of the O $1s$ peaks de-convoluted from the XP spectra of the InZnO thin films with different In contents.

Table 3.5.2 Comparison of portions of the In $3d_{5/2}$ peaks de-convoluted from the XP spectra of the InZnO thin films with different In contents.

Table 3.8.1 Values of grain size, ΔV_{th} and change ratio of grain boundary area and ΔV_{th} for various In content. (The devices with 5 and 16 at.%In did not show appropriate TFT operation)

Table. 4.3.1 Electrical characteristics of the IZO TFTs with 52, 65 and 77 at. %In.

Table. 4.4.1 Optical bandgap of the IZO films.

List of Figures

Fig. 2.1.1 Dependence of ρ and μ_H on p_O for the IZO films.

Fig. 2.1.2 Dependence of the room temperature film's mobility on the carrier concentration.

Fig. 2.1.3 (a) Structure of $\text{InGaO}_3(\text{ZnO})_5$, (b) Schematic of the crystal structure, and (c) Cross-sectional high resolution TEM images of a $\text{InGaO}_3(\text{ZnO})_5$ thin film.

Fig. 2.1.4 (a) Room temperature Hall mobility and carrier concentration as functions of chemical composition. (b) Relationships between Hall mobility and carrier concentration in a-IGZO and a-IZO films.

Fig. 2.1.5 Schematic electronic structures of silicon and ionic oxide semiconductors. Bandgap formation mechanisms in (a) covalent and (b,c) ionic oxide semiconductor.

Fig. 2.1.6 Schematic orbital drawings for the carrier transport paths : (a) covalent semiconductor, (b) amorphous oxide semiconductor.

Fig. 2.1.7 (a) Hall mobilities of $\text{InGaO}_3(\text{ZnO})_m$ as functions of electron density. (b) Illustration to explain the percolation conduction model.

Fig. 2.1.8 Schematic electronic structure of a-IGZO.

Fig. 2.2.1 Typical device structures used for AOS TFTs.

Fig. 2.2.2 Energy band diagrams as viewed through the gate for several biasing

conditions: (a) equilibrium, (b) depletion ($V_{GS} < 0$ V), and (c) accumulation ($V_{GS} > 0$ V).

Fig. 2.2.3 Representative (a) transfer and (b) output characteristics n-type oxide-TFTs.

Fig. 2.3.1 PBS-induced V_{th} shift of *a*-IGZO TFTs. The inset shows the bias-stress-induced shift of $\log I_{DS}$ - V_{GS} curve.

Fig. 2.3.2 NBS-induced V_{th} shift of *a*-IGZO TFTs.

Fig. 2.3.3 Changes in the I_{DS} - V_{GS} characteristics of ZnO TFTs under (a) PBS, (b) PBIS, (c) NBS, and (d) NBIS conditions.

Fig. 2.3.4 (a) Schematic showing the electric-field-induced adsorption of oxygen molecules from the ambient atmosphere under NBS. (b) Schematic showing the electric-field-induced desorption of water molecules into the ambient atmosphere under PBS.

Fig. 2.3.5 Photo-generated hole trapping in an NBIS condition.

Fig. 2.3.6 V_{th} degradation process under an NBIS condition by oxygen vacancy transition model.

Fig. 2.3.7 Examples of stretched exponential fit: (a) $t - \Delta V_{th}$ fit, (b) $\tau - 1000/T$ fit for obtaining an activation energy value.

Fig. 3.2.1 Fabrication process flow of the IZO TFTs.

Fig. 3.3.1 Representative transfer characteristics of $In_xZn_{1-x}O$ TFTs with different In

fractions.

Fig. 3.3.2 (a) Electron concentration and (b) Hall mobility of $\text{In}_x\text{Zn}_{1-x}\text{O}$ films.

Fig. 3.4.1 Evolution of transfer characteristic of the IZO TFT (81 at.% In) under the NBIS condition, which shows a parallel shift of the curve.

Fig. 3.4.2 Variation of the NBIS induced V_{th} shift as a function of the In content in IZO thin films.

Fig. 3.5.1 O $1s$ XP spectra (surface) for the (a) $\text{In}_{0.16}\text{Zn}_{0.84}\text{O}$, (b) $\text{In}_{0.52}\text{Zn}_{0.48}\text{O}$, (c) $\text{In}_{0.77}\text{Zn}_{0.23}\text{O}$ and (d) $\text{In}_{0.85}\text{Zn}_{0.19}\text{O}$ thin films.

Fig. 3.5.2 XP spectra (surface) of metal cations: (a) In $3d$, and (b) Zn $2p$.

Fig. 3.5.3 In $3d$ XP spectra (bulk) for the (a) $\text{In}_{0.16}\text{Zn}_{0.84}\text{O}$, (b) $\text{In}_{0.52}\text{Zn}_{0.48}\text{O}$, (c) $\text{In}_{0.77}\text{Zn}_{0.23}\text{O}$ and (d) $\text{In}_{0.85}\text{Zn}_{0.19}\text{O}$ thin films.

Fig. 3.6.1 2D GIXD patterns of the (a) ZnO, (b) $\text{In}_{0.52}\text{Zn}_{0.48}\text{O}$, (c) $\text{In}_{0.65}\text{Zn}_{0.35}\text{O}$, and (d) $\text{In}_{0.73}\text{Zn}_{0.27}\text{O}$ film.

Fig. 3.6.2 Glancing-angle X-ray diffraction patterns of $\text{In}_x\text{Zn}_{1-x}\text{O}$ thin films with different In fractions on the SiO_2/Si substrate.

Fig. 3.6.3 Boron concentration as a function of depth in amorphous and polycrystalline Si after ion implantation.

Fig. 3.7.1 Cross-section TEM images of IZO films of (a) 52, (b) 65, and (c) 77 at.%In, respectively. Inset shows diffraction pattern of the selected area, and (d), (e), (f) are magnified images of the selected area.

Fig. 3.7.2 SEM images of $\text{In}_x\text{Zn}_{1-x}\text{O}$ films: (a) top view of 16 nm-thick films and (b) cross-section view of 130 nm-thick films. White numbers represent In content (at.%) of the films.

Fig. 3.8.1 (a) Average grain size by Scherrer's equation, (b) Change ratio of grain boundary area and ΔV_{th} under NBIS with increasing In content.

Fig. 3.8.2 Percent of (a) oxygen vacancy peak and (b) 1+ charged In peak area with increasing In content.

Fig. 4.2.1 Schematic of structure of the passivated IZO TFT.

Fig. 4.3.1. Representative transfer characteristics for the three devices.

Fig. 4.4.1 Time dependence of $|\Delta V_{\text{th}}|$ under NBTS conditions for the (a) $\text{In}_{0.52}\text{Zn}_{0.48}\text{O}$, (b) $\text{In}_{0.65}\text{Zn}_{0.35}\text{O}$ and (c) $\text{In}_{0.77}\text{Zn}_{0.23}\text{O}$ TFTs at different temperatures. The solid lines are fits with a stretched exponential equation.

Fig. 4.4.2. Relaxation time τ as a function of the reciprocal temperature for the (a) $\text{In}_{0.52}\text{Zn}_{0.48}\text{O}$ (b) $\text{In}_{0.65}\text{Zn}_{0.35}\text{O}$ and (c) $\text{In}_{0.77}\text{Zn}_{0.23}\text{O}$ TFTs. The activation energies were obtained from the slope of the straight lines. The inset shows the corresponding dispersion parameter β as a function of the reciprocal temperature.

Fig. 4.4.3 Schematic diagram showing the migration of V_{O}^{2+} defects for (a) polycrystalline and (b) amorphous IZO materials under the NBTS.

Fig. 4.4.4 (a) Transmittance of IZO films with different In contents. (b) Tau plot

from the transmittance data for obtaining the optical bandgap.

Fig. 4.5.1 Recovery time dependence of ΔV_{th} for the (a) $In_{0.52}Zn_{0.48}O$, (b) $In_{0.65}Zn_{0.35}O$ and (c) $In_{0.77}Zn_{0.23}O$ TFTs at different temperatures. The corresponding relaxation time variations as a function of the reciprocal temperature for the (d) $In_{0.52}Zn_{0.48}O$, (e) $In_{0.65}Zn_{0.35}O$ and (f) $In_{0.77}Zn_{0.23}O$ TFTs.

Fig. 4.5.2 Proposed energy diagram model showing the activation energy of the NBTS-induced V_{th} shift and their recovery process.

Fig. 4.5.3 Comparison of V_{th} displacement when NBTS and recovery was repeated.

The NBTS condition was $V_g = -30$ V, $170^\circ C$ and ~ 2 h.

Fig. 4.6.1 Activation energy values of the three IZO TFTs for NBTS and recovery measurement.

Chapter 1. Introduction

1.1. Overview

Metal oxide thin film transistors (TFTs) have been studied extensively as switching devices in active-matrix (AM) liquid crystal displays (LCDs), organic light emitting diodes (OLEDs) and flexible displays on account of their high field-effect mobility ($> 10 \text{ cm}^2/\text{Vs}$), high electrical uniformity over a large substrate size, and low processing temperature. The typical properties of various oxide films are listed in Table 1.1.1.¹

Existing switching TFTs being used in LCD panels are hydrogenated amorphous silicon (a-Si:H) TFTs introduced by Spear and LeComber.² Although a-Si:H thin films exhibit good uniformity over large areas, acceptable carrier mobility ($< \sim 0.5 \text{ cm}^2/\text{Vs}$) for active matrix addressing, low production cost, and good compatibility with the existing manufacturing technology, a-Si:H TFTs are facing technical limitation as the demand for higher display image quality and larger panel size arises. Because of its low carrier mobility, a-Si:H TFTs cannot satisfy the requirement for the next generation LCD ($\mu > 5 \text{ cm}^2/\text{Vs}$), so other material having higher carrier mobility is needed to replace the a-Si:H.

In OLEDs, poly Si TFTs have been used. The poly Si TFTs show much

excellent device performance, that is, very high mobility up to $\sim 100 \text{ cm}^2/\text{Vs}$ and good stability against bias and light stress. However, poly Si TFTs have a critical problem owing to its poly-crystalline nature, causing the spatial distribution of electrical performances originating from non-uniformity of grain size and grain boundary in the poly Si film.

In this regard, the oxide semiconductor can be alternative for the a-Si:H and poly Si TFTs, because oxide semiconductor has quite high mobility ($5\sim 50 \text{ cm}^2/\text{Vs}$) and large area uniformity by sputtering process and amorphous nature. Owing to a large inter-atomic overlap of isotropic s-orbitals, oxide semiconductors can possess high mobility even in amorphous state. Additionally, oxide semiconductors are usually transparent in the visible region of the electromagnetic spectrum as a result of wide bandgap ($>3 \text{ eV}$), which enables application for transparent electronic devices. (Table 1.1.2 summarized properties of the three devices.^{3 4}) However, because oxide semiconductors have intrinsic defects, resulting in n-type property, so that oxide TFTs tend to suffer from instability under electrical bias, temperature, light. In particular, negative bias illumination stress (NBIS)-induced instability is a crucial problem, which reflects the real operation environment of display inside and causes a negative V_{th} shift.

In this dissertation, the NBIS instability of oxide semiconductor TFTs was investigated. For the study, Indium Zinc Oxide (IZO) TFTs were fabricated by

shadow masking and sputtering process. The IZO is a one of the promising oxide semiconductors on account of its high mobility exceeding ($>30 \text{ cm}^2/\text{Vs}$), but little is known about the NBIS instability of the resulting IZO TFTs. For the first experiment, IZO TFTs with various In contents (0~85 at.%) were fabricated and NBIS measurement was carried out. The field-effect mobility and sub-threshold swing were much improved with increasing In fraction; $41.0 \text{ cm}^2/\text{Vs}$ and 0.2 V/decade , respectively, at 85 at.%In, compared to $1.1 \text{ cm}^2/\text{Vs}$ and 2.4 V/decade of ZnO TFTs. In contrast, the NBIS instability in the V_{th} shift was not proportional shape. A local minimum negative bias illumination stress instability was observed near 73–77 at.%In, where the structure of IZO channel layer changed from polycrystalline to amorphous. It was confirmed that the crystallinity of channel layer is important to the device instability as well as oxygen vacancy concentration, and it was suggested the migration of photo-excited V_{O}^{2+} defects also plays an important role in determining the overall V_{th} instability.

In addition, the kinetics of the negative bias thermal stress (NBTS)-induced V_{th} variations of IZO transistors with different crystallographic qualities were examined based on the stretched-exponential formalism. A polycrystalline IZO device had a 0.64 eV lower activation barrier energy than an amorphous IZO device under NBTS conditions. This was attributed to the difference in the migration energy barrier between polycrystalline and amorphous IZO films. For the recovery

process, however, the activation energy barriers (~ 0.75 eV) were independent of the crystalline structure. A plausible microscopic mechanism to account for the experimental results was proposed by comparing the activation energy barrier values.

The organization of this dissertation is as follows. Chapter 2 reviews literature about oxide semiconductors, which describes properties of oxide semiconductor materials, thin film transistor and device instability, *etc.*. Chapter 3 explains the result of NBIS instability of IZO TFTs experimented by a cation combinatorial method. Chapter 4 explains the kinetics of the NBTS-induced V_{th} variations investigated by stretched exponential formula.

Table. 1.1.1 Typical properties of various n -type oxide films. ¹

Mat.	E_g^{opt} (eV)	T (%)	μ_{Hall} (cm ² /Vs)	N_d (cm ⁻³)	ρ (Ω cm)
CdO	2.2-2.6	75	220	10^{19} - 10^{21}	2×10^{-3}
Cd ₂ SnO ₄	2.9-3.1	90	35-60	$\sim 7 \times 10^{21}$	$\sim 2 \times 10^{-4}$
In ₂ O ₃	3.7	80-90	10-40	$\leq 10^{21}$	$\geq 10^{-4}$
InGaO ₃	3.3	90	10	10^{20}	2.5×10^{-3}
InGaZnO ₄	3.5	80-90	24	$\sim 10^{20}$	2×10^{-3}
SnO ₂	3.6	80-90	5-30	$\leq 10^{20}$	$\geq 10^{-3}$
ZnO	3.2-3.3	80-90	5-50	$\leq 10^{21}$	$\geq 10^{-4}$
Zn ₂ In ₂ O ₅	2.9	80	12-20	$\sim 5 \times 10^{20}$	4×10^{-3}
ZnSnO ₃	3.5	80	7-12	10^{20}	5×10^{-3}
Zn ₂ SnO ₄	3.3-3.9	90	12-26	6×10^{18}	$\sim 5 \times 10^{-2}$

※ E_g^{opt} : optical band-gap, χ : electron affinity, μ_{Hall} : Hall mobility, N_d : carrier concentration, ρ : resistivity

Table. 1.1.2 Comparison of oxide semiconductor, a-Si and poly-Si TFTs.

Properties	oxide	a-Si:H	poly-Si
μ_{SAT} (cm ² /V·s)	5~ 30	< 1	30 ~ 100
ΔV_{TH}	- 0.5 V	< 3 V	< 1×10 ⁻² V
S (V/decade)	0.5	1.49	0.5
Process Temp. [°C]	RT ~ 400	150 ~ 350	250 ~ 550
TFT uniformity	Good	Good	Poor
TFT type	n-type	n-type	CMOS
Application	AMLCD, AMOLED	AMLCD	AMOLED

Chapter 2. Literature review

2.1. Metal oxide semiconductor

2.1.1. Metal oxide semiconductor materials

2.1.1.1. Binary oxide semiconductors

The key binary oxide semiconductors (ZnO, In₂O₃, SnO₂, etc.) have wide bandgap (> 3.0 eV) that allow the transmission of visible light.⁵ Often even when undoped, they exhibit much higher electrical conductivities (10^{-2} /Ω cm to 10^2 /Ω cm) than other wide gap metal oxide materials due to inherent high levels of n-type conductivity. This indicates that native shallow defects must exist including either oxygen vacancies, cation interstitials, or interstitial hydrogen.⁶ Because of such donor defects, these binary oxides exhibit relatively high carrier concentrations (> 10^{18} cm⁻³) and electron mobilities (> 10 cm²/V · s) even when deposited at room temperature. As a consequence, they have undergone intensive research as transparent conducting materials and semiconductors for various electronic devices (e.g., LCDs, OLEDs, and solar cells).

1) ZnO

Zinc oxide crystallizes in the hexagonal wurtzite lattice. The zinc atoms are nearly in the position of hexagonal close packing. Each oxygen atom lies within a tetrahedral group of four zinc atoms, which are in the same direction along the hexagonal axis. ZnO lattice has space group $P6_3mc$, with the lattice constants of $a=b= 3.24 \text{ \AA}$, $c= 5.19 \text{ \AA}$. Three of the oxygen atoms in the distorted ZnO_4 tetrahedron are placed in one close-packed ab plane, whereas the fourth oxygen atom is located in the adjacent plane. As a result, the structure contains an array of vertical Zn-O vectors along the c axis, resulting in a classical polar structure. The physical properties of ZnO and In_2O_3 are summarized in Table. 2.1.1.

The electronic structure of ZnO has been calculated by many researchers. The lowest two valence bands correspond to the $O_{2-} 2s$ core-like states. The next six valence bands correlate to the $O_{2-} 2p$ bonding states. The first two conduction band states are strongly localized on zinc and correspond to the unoccupied $Zn^{2+} 4s$ levels. The higher conduction bands are free-electron-like. The fundamental bandgap, calculated by using band structure models, is $\sim 3.4 \text{ eV}$ at room temperature.⁷ The undoped ZnO is slightly an n-type wide and a direct bandgap semiconductor. The n-type conduction is attributed to the deviation from the stoichiometry. The free carriers are created from the self-donors, associated with the oxygen vacancies and/or interstitial zinc. The donor levels are also produced by

the incorporation of foreign atoms such as hydrogen, indium, aluminum, and gallium. It is necessary to fabricate both p-type and n-type ZnO in order to realize bipolar devices from ZnO. However, wide bandgap semiconductors generally have an asymmetric doping problem; that is they can be easily doped to either an n-type or a p type, but not both. For example, ZnO is easily doped to an n-type with a very high carrier density and low resistance by group III elements. However, p-type doped ZnO is very difficult to achieve. Group V elements such as nitrogen have been considered as acceptor dopants.

ZnO TFTs in former studies exhibited field effect mobility values ranging from 0.2 to 40 cm^2/Vs by the optimization of the semiconductor microstructure, post annealing, and selection of gate insulator.⁸ However, it is recognized that the formation of amorphous or single crystalline ZnO thin films is very difficult, and in general a polycrystalline structure is obtained, which leads to the formation of grain boundary defects. The existence of grain boundaries induces non-uniform TFT performance at different locations across a single flat panel display. Another problem is the difficulty of fabrication, which originates from the low chemical durability of pure ZnO against acidic etchants. Because of such problems, intensive research has been carried out on the development of amorphous metal oxide semiconductors with comparable or better device properties than those of ZnO TFTs.

2) In_2O_3

In_2O_3 has a bixbyite crystal structure that is inherently a cubic-type rare earth, vacancy-defect oxide. Bixbyite has an 80 atom unit cell with the $Ia\bar{3}$ space group and a 1 nm lattice constant in an arrangement, based on the stacking of the MO_6 coordination groups.⁷ The bixbyite structure is similar to that of fluorite and has a face-centered cubic array of indium atoms with all the tetrahedral interstitial positions filled with oxygen atoms. The primary difference between fluorite and bixbyite is the MO_8 coordination units in the bixbyite structure (the oxygen position is on the corners of a cube and the indium atom is located at the center of the cube) are replaced by units with oxygen atoms missing from either the body or the face diagonally. The removal of two oxygen atoms from the MO_8 to form the MO_6 coordination units forces the displacement of the indium from the center of the cube. Thus, indium is distributed in two nonequivalent sites with one-quarter of the indium atoms positioned at the center of a trigonally distorted oxygen octahedron (diagonally missing O), and the remaining three-quarters positioned at the center of a more distorted and less symmetric octahedron that results from the removal of two oxygen atoms from the same face of the octahedron. The resulting MO_6 coordination 5 units are then stacked such that one-quarter of the oxygen atoms are missing from each $\{100\}$ plane in the fluorite structure.

In_2O_3 has a cubic bixbyite structure in which O^{2-} ions occupy, in an ordered

manner, three-quarters of the tetrahedral interstices of a faced-centered-cubic In^{3+} ion array. Consequently, In_2O_3 should consist of a filled O^{2-} 2p valence band that is primarily oxygen 2p in character.⁹ The In 3d core lies below the valence band edge (E_v). The conduction band is the In 5s band with band edge (E_c) approximately 3.75 eV above E_v . In_2O_3 is usually oxygen-deficient. At high oxygen vacancy concentration, an oxygen vacancy band forms and overlaps E_c at the bottom of the conduction band such that In_2O_3 becomes a degenerated semiconductor. Hereby, the oxygen vacancies act as doubly ionized donors and contribute a maximum of two electrons to the conduction band. Electrons can also be generated by doping tin into indium oxide to form tin-doped In_2O_3 . Since indium has a valence of three, the tin substitution results in an n-type doping by providing an extra electron to the conduction band to preserve the overall charge neutrality.

The development of In_2O_3 TFTs was launched late because indium oxide (In_2O_3), while a well-known transparent conductive oxide (TCO) with high carrier concentration ($>10^{19} \text{ cm}^{-3}$), shows some difficulty in having its carrier concentrations reduced to semiconducting levels ($< 10^{18} \text{ cm}^{-3}$). Lavareda et al. reported InO_x TFTs with bottom gate structure. They optimized the rf power and oxygen pressure during InO_x deposition by 'radio-frequency plasma enhanced reactive thermal evaporation', resulting in broad ranges of electrical resistivity from 13.7 to $1.7 \times 10^7 \Omega \text{ cm}$. The InO_x TFTs showed reasonable electrical performance,

including μ_{fe} of $0.02 \text{ cm}^2/\text{Vs}$ and drain current on/off ratio of 10^4 .¹⁰ Following that, Vygranenko et al. improved the electrical performance of In_2O_3 TFTs by using In_2O_3 channel layers deposited by ion-beam-assisted evaporation.¹¹ They fabricated a reliable In_2O_3 TFT at room temperature, showing μ_{fe} of $3.3 \text{ cm}^2/\text{Vs}$, subthreshold swing (SS) of 0.5 V/decade , and drain current on/off ratio of 10^6 . They also suggested that achieving a high performance In_2O_3 device is dependent on precise control of the oxygen ion beam flux and interface defects ($\text{In}_2\text{O}_3/\text{SiO}_x$). Moreover, Dhanajay et al. investigated In_2O_3 TFTs fabricated at a substrate temperature of $100 \text{ }^\circ\text{C}$ as a function of active channel thickness ($5\sim 20 \text{ nm}$).¹² They found that there is a reduction in grain boundary density in thicker films leading to a higher mobility ($\sim 34 \text{ cm}^2/\text{Vs}$). This suggests that grain size control of the active layer is a key factor in obtaining better electrical performance with regard to mobility.

Table. 2.1.1 Summary of physical properties of In₂O₃ and ZnO.

Property	In ₂ O ₃	ZnO
Mineral name	-	Zincite
Abundance of the metal in the earth's crust (ppm)	0.1	132
Crystal structure	Cubic, bixbyite	Hexagonal, wurtzite
Lattice constants [nm]	$a = 1.012$	$a = 0.325$ $b = 0.521$
Density [g cm ⁻³]	7.12	5.67
Thermal expansion coefficient (300K) [10 ⁻⁶ K ⁻¹]	6.7	c: 2.92 ⊥ c: 4.75
Melting point [°C]	2190	2240
Static dielectric constant	~9	c: 8.75 ⊥ c: 7.8
Refractive index		2.008
E_g^{opt} [eV]	3.75	3.4
Intrinsic N_d	$> 10^{19} \text{ cm}^{-3}$	$< 10^{16} \text{ cm}^{-3}$
Exciton binding energy		60 meV
Electron Hall mobility	$200 \text{ cm}^2 \text{ V}^{-1} \text{ s}^{-1}$	$200 \text{ cm}^2 \text{ V}^{-1} \text{ s}^{-1}$
Hole Hall mobility	$5-50 \text{ cm}^2 \text{ V}^{-1} \text{ s}^{-1}$	$5-50 \text{ cm}^2 \text{ V}^{-1} \text{ s}^{-1}$

2.1.1.2. Multicomponent oxide semiconductors

Multicomponent amorphous oxides, in general, exhibit considerably better TFT performance than binary compounds. Rather than having carrier transport limited by grain boundaries, in amorphous oxides carrier transport is mostly dictated by the potential barriers located around the CBM, associated with the structural randomness, which can easily be surpassed in properly processed films by increasing V_{GS} . Furthermore, the relative proportion of the cations controls the electron carrier concentration and mobility within a broad range, which has direct implications on transistor performance.

1) IZO

IZO is a promising oxide semiconductor because of its high device mobility. Generally, one of the principles of forming amorphous materials is mixing multi-components with different crystal structures. In_2O_3 and ZnO have bixbyite and wurtzite structures, respectively, and also exhibit different coordination numbers to the oxygen as InO_6 and ZnO_4 . These aspects allow In-Zn-O (IZO) to have an amorphous phase. Consequently, the IZO has become an essential component for both the transparent electrodes for flat-panel displays and the active layer for TFTs. By varying the composition and the deposition conditions, the IZO has exhibited a

wide range of the resistivity, $10^{-4} \Omega \text{ cm}$ to $10^8 \Omega \text{ cm}$. For instance, IZO films with 10 wt.% ZnO is mostly used in electrode applications, while the films with a comparable composition of In/Zn (typically In 60:40 Zn) exhibit semiconducting behavior in the resistivity range of $10 - 10^3 \Omega \text{ cm}$.¹³ In addition, amorphous IZO has shown extremely high thermal stability even up to 600°C .¹⁴ Due to these advantages, amorphous IZO (a- IZO) has been one of the most extensively investigated TCOs and semiconducting oxides for display applications.

Martin *et al.* investigated electrical property of amorphous IZO films as a function of the oxygen partial pressure in sputtering process and discussed the conduction behavior of the IZO films.^{15 16} Figure 2.1.1 and fig. 2.1.2 show the dependence of ρ and μ_{H} on p_{O} for the IZO films and Hall mobility-carrier concentration relationship, respectively.

The carrier transport is due to preferential channel path formed by the direct overlap among the neighboring n-like metal orbitals, function of the state of oxidation of cations and oxygen vacancies, reinforced by the presence of Zn atoms in the indium oxide matrix. This makes the films insensitive to distorted metal–oxygen–metal chemical bonds, explaining so the high μ_{H} achieved, independent of the bulk defect states, as p_{O} varies from 1.5×10^{-3} to $1.5 \times 10^{-1} \text{ Pa}$. On the other hand, ρ varies from about $2 \times 10^{-4} \Omega \text{ cm}$ to $10 \Omega \text{ cm}$, for the same p_{O} range).

This proves the effectiveness of oxygen in controlling the electronic performances of IZO films from almost degenerated passive semiconductors to active semiconductors.

In typical semiconductors where the only scattering mechanism is the ionized impurity, the mobility increases as the net carrier concentration decreases. This is the behavior observed for example on the ZnO films. Nevertheless, the IZO films exhibit a reverse behavior that cannot be only explained by the fact that the Hall mobility is limited by carrier trapping at localized states and that oxygen vacancies contribute to the enhancement of conduction electrons. In IZO, the degenerated band conduction is not band tail limited, but dependent on channel conduction governed by metal cations electronic configurations of the type $(n-1)d^{10} ns^0$ (with $n \geq 4$). This electric behavior is a consequence of a conduction band primarily derived from spherically symmetric heavy-metal cation ns orbitals with large radii and so the adjacent ones overlap leading to formation of well-defined conduction paths, irrespective to the bulk film structure. The proportionality of μ -n can be explained by the role of defects and voids, originated by the presence in the same structure of metal ions with different cross sections, which will trap electrons and by the fact that oxygen vacancies will contribute to the enhancement of conduction electrons. Thus, as these defects centers become negatively charged, they will scatter electrons, reducing so the mobility as the carrier concentration decreases.

Even though a-IZO films have exhibited adequate properties as a component of TFTs, such as excellent uniformity and large mobility ($>30 \text{ cm}^2/\text{Vs}$), one of the critical issues with this material is the controllability of the carrier concentration. Because IZO typically exhibits a high carrier concentration of $>10^{18} \text{ cm}^{-3}$, this can lead to large off-current and small on-off ratios. Therefore, to reduce the carrier concentration below that, doping has been conducted into the a-IZO.

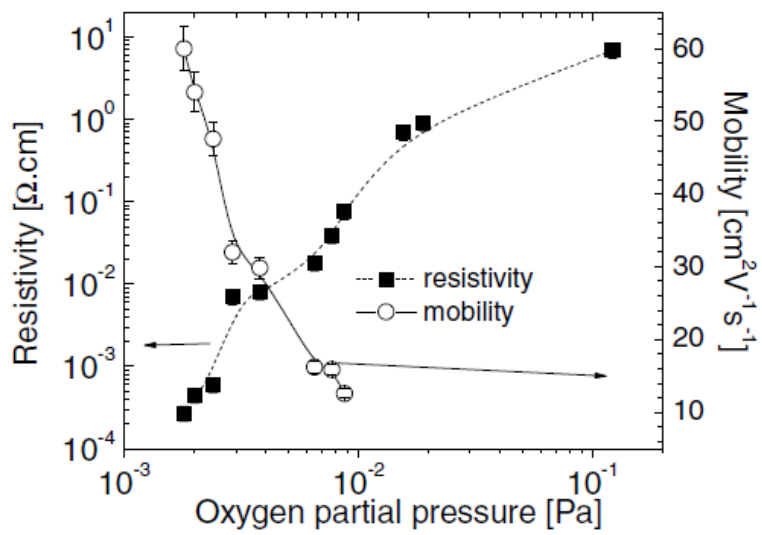


Fig. 2.1.1 Dependence of ρ and μ_{H} on p_{O} for the IZO films.¹⁶

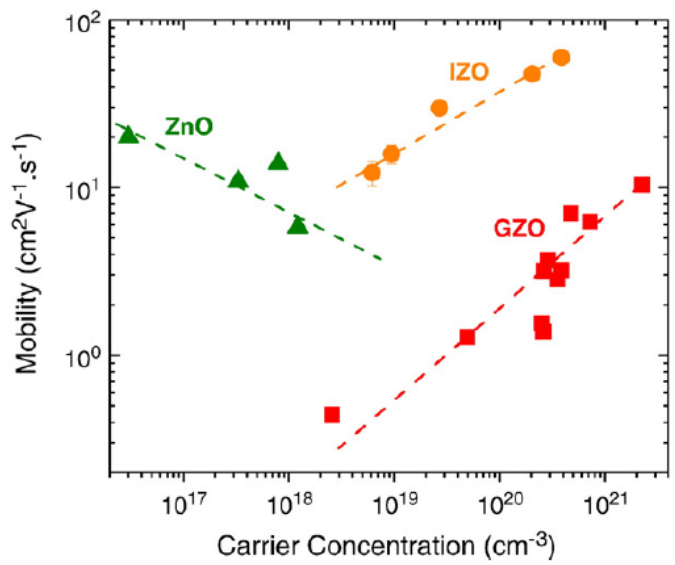


Fig. 2.1.2 Dependence of the room temperature film's mobility on the carrier concentration.¹⁵

2) IGZO

Currently, IGZO is most widely used semiconducting oxide. Since Nomura et al. inserted Ga into IZO,¹⁷ the IGZO has been extensively studied for the display industry application. Their approach demonstrated that the carrier concentration of amorphous IGZO can be lowered below $< 10^{17} \text{ cm}^{-3}$ while its electron mobility ($\sim 10 \text{ cm}^2/\text{Vs}$) remains high. The decrease of the carrier concentration has been attributed to the high ionic potential of Ga^{3+} ions, which allows them to tightly bind oxygen ions and thereby suppress the formation of oxygen vacancies.

In the structure of IGZO ($\text{InGaO}_3(\text{ZnO})_5$) structure, its layered super lattice structures in which InO_2 layers and $\text{GaO}(\text{ZnO})_5$ blocks were alternately stacked along the (0001) axis, as shown in Figure 2.1.3.¹⁸ The layers are similar to those of indium tin oxide (ITO) and Ga-doped ZnO, in which carrier doping is controlled by the amount of Ga. However, the Ga^{3+} ion incorporated in the $\text{GaO}(\text{ZnO})_5^+$ block does not generate carriers in $\text{InGaO}_3(\text{ZnO})_5$ because the Ga^{3+} ion does not substitute the Zn^{2+} tetrahedral sites only, but also takes trigonal-bipyramidal coordination sites, which keeps the local electro neutrality.¹⁸ The structure of the $\text{GaO}(\text{ZnO})_5^+$ is very similar to wurtzite ZnO and in-plane lattice mismatch is very small, only $\sim 0.8 \%$ (the a -axis lattice parameter a is 0.328 nm for $\text{InGaO}_3(\text{ZnO})_5$ and 0.3249 nm for ZnO).¹⁹ Moreover, the In_2O_3 layer works as a blocking barrier for oxygen out diffusion, and thereby may suppress the formation of oxygen vacancy. It is

therefore easier to maintain the material in stoichiometry and control the carrier concentration down to the intrinsic level in a single crystal.

Figure 2.1.4 summarizes electrical properties (Hall mobility and carrier concentration) for the films in the In_2O_3 - Ga_2O_3 - ZnO system. Although pure In_2O_3 and ZnO films exhibited high Hall mobilities of 34 and 19 cm^2/Vs , respectively, they were crystalline even if the films were deposited at RT. Moreover, it is not easy to reduce carrier concentration to $< 10^{17} \text{ cm}^{-3}$ in these films without compensation doping. Pure Ga_2O_3 formed amorphous films but carrier doping, i.e., the formation of oxygen vacancies, was very difficult irrespective of deposition conditions. Thus, these endmember materials in this ternary system are not suitable for TFTs because they have local non-uniformity due to grain boundaries, no stable amorphous phase and/or difficulty in generating carriers. As known in glass science, the incorporation of aliovalent different-sized cations is effective in enhancing amorphization, and it is very favorable to introduce network-forming cations. Indeed, stable amorphous phases were formed in the binary systems of In_2O_3 - Ga_2O_3 (a-IGO) and ZnO - Ga_2O_3 (a-GZO), and in the ternary system of In_2O_3 - Ga_2O_3 - ZnO (a-IGZO).

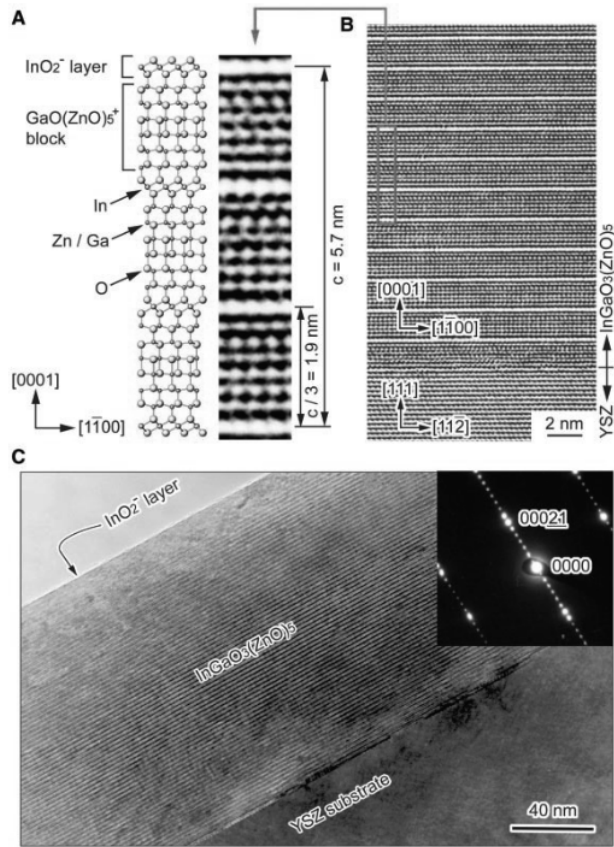


Fig. 2.1.3 (a) Structure of $\text{InGaO}_3(\text{ZnO})_5$, (b) Schematic of the crystal structure, and (c) Cross-sectional high resolution TEM images of a $\text{InGaO}_3(\text{ZnO})_5$ thin film.¹⁸

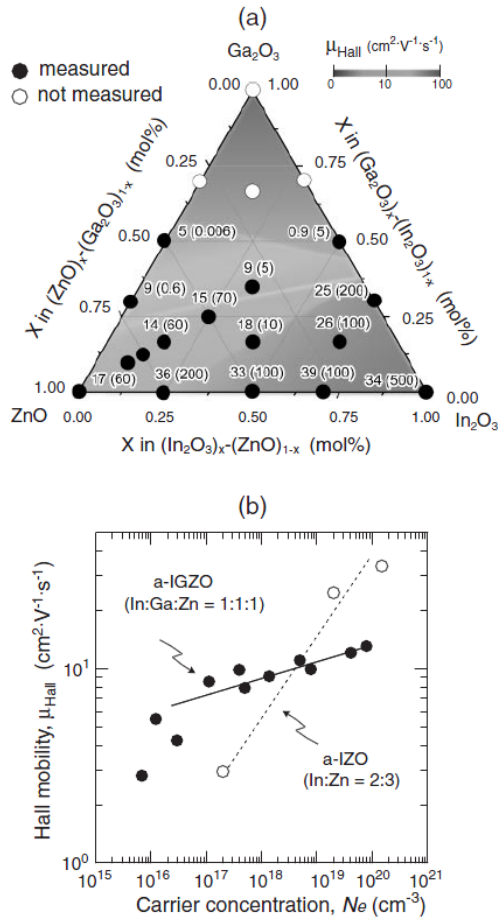


Fig. 2.1.4 (a) Room temperature Hall mobility and carrier concentration as functions of chemical composition. (b) Relationships between Hall mobility and carrier concentration in a-IGZO and a-IZO films.²⁰

2.1.2. Electronic structure and carrier transport mechanism in oxide semiconductors

Generally, it is believed that the properties of amorphous semiconductors are considerably degraded compared with their corresponding crystalline phases, which is actually the case for silicon because intrinsic crystalline silicon (c-Si) exhibits an electron mobility of $1,500 \text{ cm}^2/\text{Vs}$, which deteriorates to less than $2 \text{ cm}^2/\text{Vs}$ in a-Si:H. On the other hand, AOSs exhibit large electron mobilities of greater than $10 \text{ cm}^2/\text{Vs}$ even in amorphous structures. Hosono *et al.* propose a theory to explain the dramatic differences seen in the electronic and optical properties of traditional amorphous semiconductors and AOS.¹⁷ In contrast to covalent semiconductors, oxide semiconductors are ionic in nature and the conduction band minimum (CBM) and the valence band maximum (VBM) are formed by different ionic species. When metal atoms and oxygen atoms come close, due to the large differences in the electron affinity and ionization potential, charge transfer takes place ionizing the atoms and leading to electrostatic separation of the anionic and cationic sites. This leads to the CBMs being primarily composed of metal cations and the VBMs composed of oxygen $2p$ orbitals in most oxides although this does not hold for lanthanide and actinides and transition metal oxides. A large bandgap in oxides is attained by the low energy of the oxygen $2p$ orbitals leading to transparency. It has

been proposed that metal oxides composed of heavy metal cations (HMC) with an electronic configuration $(n-1)d^{l_0}ns^0$ where $4 \leq n \leq 6$ would lead to realizing high mobility in amorphous oxides. To achieve high mobility a continuous conduction path is required and hence a large overlap between relevant orbitals is essential. Moreover the magnitude of the overlap needs to be insensitive to the structural randomness, which is intrinsic to the amorphous state, and HMCs satisfy both these requirements. The bottom part of the conduction band in these oxides is primarily composed of ns orbitals of the HMCs. Given the spatial spread of the s orbital is larger than the inter-cationic distance (by selecting a suitable value of n), and owing to the spherical symmetry of the s -orbital, large overlap and insensitivity to the amorphous state is achieved. The electronic structure is depicted in fig. 2.1.5 and fig 2.1.6 In silicon, the conduction band minimum (CBM) and valence band maximum (VBM) are made of anti-bonding ($sp^3 \sigma^*$) and bonding ($sp^3 \sigma$) states of Si sp^3 hybridized orbitals, and its bandgap is formed by the energy splitting of the $\sigma^*-\sigma$ levels (fig 2.1.5 (a)). By contrast, oxides have strong ionicity and charge transfer occurs from metal to oxygen atoms (fig 2.1.5 (b)), and the electronic structure is stabilized by the Madelung potential formed by these ions, raising the electronic levels in cations and lowering the levels in anions. Consequently, the CBM is primarily formed by the unoccupied s orbitals and the VBM of anion by

fully occupied O $2p$ orbitals, as illustrated in fig 2.1.5 (c). As schematically shown in figure 2.1.6 (a), the spatial spreading of the s -orbital is considerable and the overlap between these ns orbitals with spherical symmetry is large and insensitive to any angular variation in the bonding angles compared with the cases of p - p or d - p orbitals having high spatial anisotropy. Figure 2.1.6 (b) shows the spatial directivity of a typical covalent semiconductor having sp^3 orbitals. Owing to this arrangement, the amorphous state leads to highly strained chemical bonds, which leads to rather deep and high-density localized states below the CBM and above VBM, causing carrier trapping. This would also explain why amorphous semiconductors typically exhibit much deteriorated carrier transport properties compared to their crystalline counterparts as shown in a-Si:H and chalcogenides whereas the electron mobility of AOS is comparable to their corresponding crystalline counterparts. The above electronic structure of AOS explains their peculiar properties not observed in conventional amorphous semiconductors. First, the electron mobilities ($10 - 40 \text{ cm}^2/\text{Vs}$) in AOS devices are relatively high, greater than a-Si:H by a factor > 10 and most organic semiconductors by a factor $> 10^2$. Second, a Hall sign anomaly is seen in conventional amorphous semiconductors in which the sign of the Hall coefficient is different from that of the Seebeck coefficient.²¹ This is presumably due to the short carrier mean free paths, which invalidates assumptions made in the Boltzmann transport equations.²² In AOS, the

Hall coefficient matches that of the Seebeck coefficient, which indicates that the length of the electron mean free path is longer translating to larger mobilities. Third, it is possible to dope AOS degenerately whereas this is not possible in conventional amorphous semiconductors. Carrier conduction in conventional amorphous semiconductors takes place by hopping between tail states within the band gap of the semiconductor where the Fermi level is pinned leading to lower mobilities.²¹ In contrast, with appropriate doping or via application of a gate bias in a thin film transistor structure, the Fermi level of AOS can be moved into the conduction band, resulting in degenerate or band conduction. Table. 2.1.2 lists some of the properties that differentiate the two classes of amorphous semiconductors. Primarily TCO are based on heavy metal cations similar to AOS but are degenerately doped to achieve high conductivity. By achieving well-controlled and low carrier concentration active transparent devices, namely transistors, can be made using oxide semiconductors.

Figure 2.1.7 (a), (b) shows μ -n relationship and conduction mechanism model of IGZO, respectively, which can be considered as a representative in oxide semiconductors. As shown in figure 2.1.7 (a), electron mobility of IGZO increases with increasing free-electron density (behavior (i)), and the maximum Hall mobility is similar for crystalline $\text{InGaO}_3(\text{ZnO})_m$ and a-IGZO (behavior (ii)). The reason for (ii) is that the band dispersions, i.e. the effective masses, are similar for c-IGZO and

a-IGZO because their CBM bands are formed by the s orbitals. Behavior (i) is opposite that of single-crystalline semiconductors, in which the carrier mobility usually decreases with increasing carrier density because of scattering on the ionized donors or acceptors. Behavior (i) is explained by a percolation conduction model.^{23 24} As illustrated in figure 2.1.7 (b), a distribution of potential barriers is formed above CBM owing to the disordered structure. Electrons take shorter transport paths at high temperatures even if these paths have high potential barriers (path (i) in figure 2.1.7 (b)). They take a longer path (ii) with lower barriers at lower temperatures because they do not have sufficient thermal energy to pass the high potential barriers. In this model, a distribution of potential barriers exists in the conduction band and limits the electron mobility, and electrons take a shorter and higher conduction path at higher temperatures. This means that the mobility increases and the activation energy decreases with increasing temperature. An analysis by the percolation model revealed that the potential distribution is approximately 0.1 eV in height and a few tens of millielectronvolts in width (fig. 2.1.8).

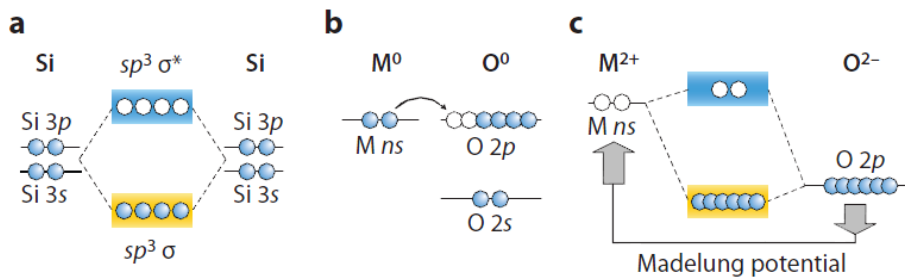


Fig. 2.1.5 Schematic electronic structures of silicon and ionic oxide semiconductors. Bandgap formation mechanisms in (a) covalent and (b,c) ionic oxide semiconductor.²⁵

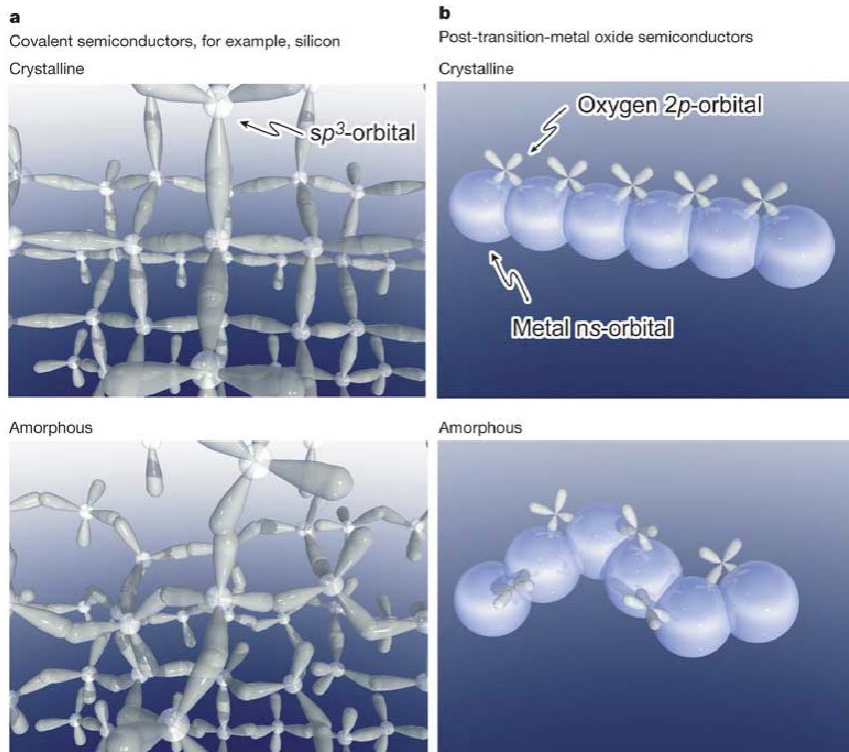


Fig. 2.1.6 Schematic orbital drawings for the carrier transport paths : (a) covalent semiconductor, (b) amorphous oxide semiconductor.¹⁷

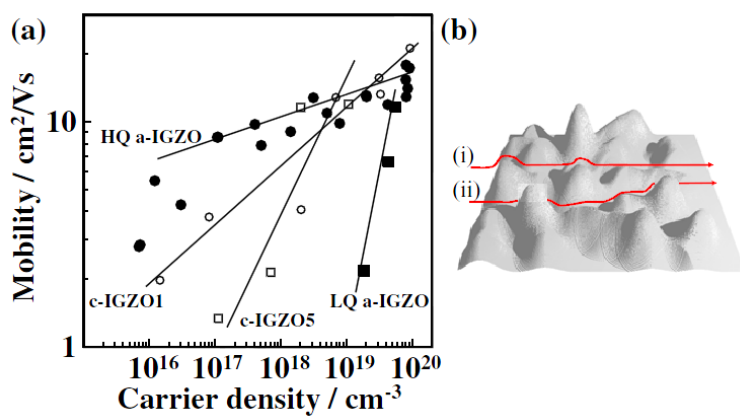


Fig. 2.1.7 (a) Hall mobilities of $\text{InGaO}_3(\text{ZnO})_m$ as functions of electron density.

(b) Illustration to explain the percolation conduction model.²⁶

Table. 2.1.2 Comparison of the characteristics of conventional amorphous semiconductor and AOSs.

	Conventional Amorphous Semiconductors (a:Si-H)	Amorphous Oxide Semiconductors
Mobility	1-2 cm ² V ⁻¹ sec ⁻¹	10-60 cm ² V ⁻¹ sec ⁻¹
Chemical Bonding	Covalent	Ionic
Conduction Mechanism	Hopping	Band Conduction
Doping degenerately	Not possible	Possible

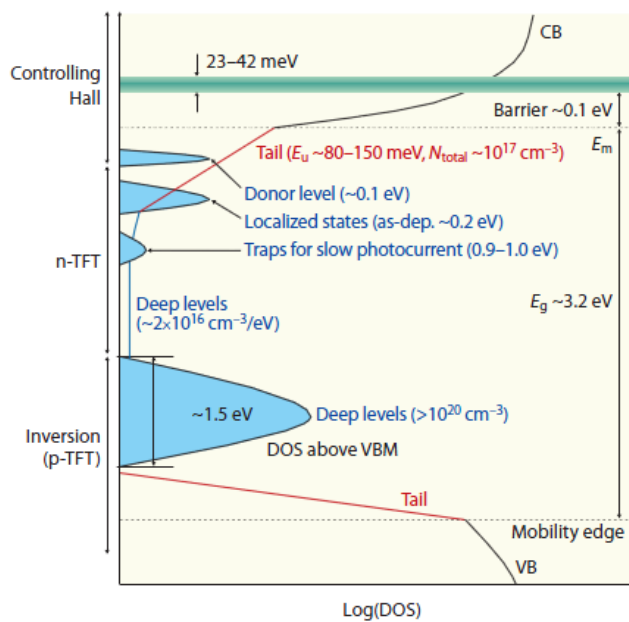


Fig. 2.1.8 Schematic electronic structure of a-IGZO.²⁵

2.2. Thin film transistors

2.2.1. Device structures

Fig. 2.2.1 illustrates typical device structures used for AOS TFTs. It is convenient to specify the TFT structure by the stacking order of the gate electrode, channel layer and source/drain electrodes (contacts) and to classify them into combinations of top/bottom gate and top/bottom contact. There is another structure called a co-planar structure in which source/drain contacts are formed in the same plane of the channel layer. This structure is employed for poly-Si TFTs and c-Si field-effect transistors (FETs), and its use has also recently been proposed for a-IGZO TFTs. The top-gate structure was employed for TFTs using epitaxial layers in which it is difficult to form a bottom electrode (e.g. c-InGaZnO₄ FET). This structure has other advantages. For example, it requires only two patterning mask steps at minimum, and the upper gate insulator and electrode act as passivation layers that protect the channel layer from degradation due to atmospheric exposure. Bottom-gate structures are common in laboratory research because commercially available SiO₂/Si wafers can be used for the gate insulator and electrode, respectively, and TFT structures are easily formed by the deposition of a channel layer with a single mask step to form the source and drain electrodes. This structure

is, of course, not applicable to practical displays, and it has various disadvantages. For example, (i) the back-channel surface is exposed to the atmosphere, and therefore the TFT characteristics can be affected by the adsorption, desorption and diffusion of atmospheric gases, causing instability and (ii) the gate—source/drain overlaps are very large and result in a large parasitic capacitance, which slows the response of devices and circuits. Both gate structures can employ either top-contact or bottom-contact structures. An advantage of the top-contact structure for oxide TFTs is that it can minimize the oxidation of the source/drain electrodes at the semiconductor channel interface, and geometrically accurate contacts can easily be formed. On the other hand, using a bottom-contact structure, more care is required to make good contacts with the upper channel layer, such as by forming taper-edge structures in the electrodes.²⁷ Inverted staggered structures have been employed in most prototype displays. One reason for this is that the same structures are used for a-Si:H TFTs. These structures employ bottom-gate and top-contact configurations, which are further classified by the structure above the channel layer. One is an etch-stopper structure, where an etching protection layer is formed before forming the source and drain; the latter are patterned by etching. The other is a channel-etch structure where a part of the channel layer is removed when the source and drain are formed by etching. The channel-etching procedure damages the back-channel surface and can cause the degradation of TFT characteristics; it also requires a thick

channel to stop etching in the channel layer. The etch-stopper structure is free from these problems but requires an extra patterning mask. Both structures have been employed for the mass production of a-Si:H TFTs and are also used for AOS TFTs.

In this dissertation, TFTs was fabricated as the bottom gate, top contact type, but the channel layer was also defined by shadow mask. Schematic picture of the resulting TFT are shown in section 3.2.

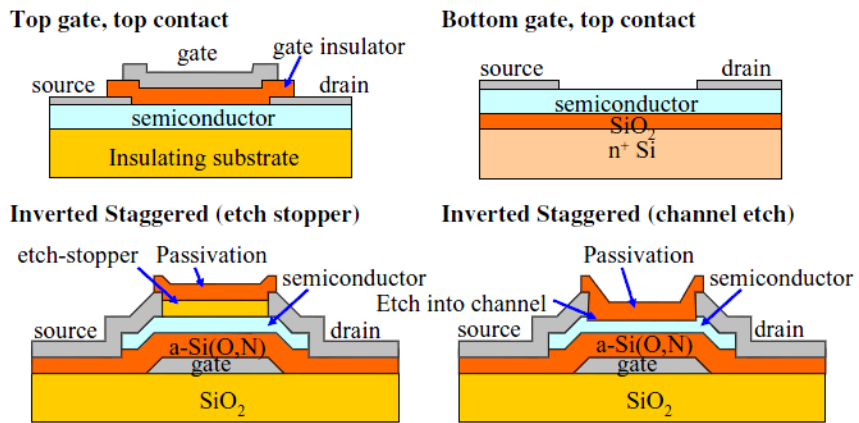


Fig. 2.2.1 Typical device structures used for AOS TFTs.²⁶

2.2.2. Operation of oxide TFT

The oxide TFTs, such as ZnO, IGZO, ZTO, IZO, etc., are ideal n-type mode transistors, which means an electron accumulation layer is formed by appropriate bias. Figure 2.2.2 shows energy band diagrams of accumulation-mode TFT.²⁷ The energy band diagrams are represented as a change of field of gate voltage and charge carriers at the interface between the channel and insulator layer.

1) Equilibrium Mode

Figure 2.2.2 (a) shows the device at equilibrium. In equilibrium mode, the gate and S/D is applied to 0 V. When gate voltage of 0 V is applied, the conductance of the semiconductor is significantly low. There is no flow of charges through the channel layer because of no difference of the Fermi level (E_F) between the semiconductor and metal. However, if the intrinsic Fermi levels of metal and semiconductor are quite different, the internal field between metal and semiconductor exists in equilibrium state, which can induce electron accumulation or depletion of semiconductor/insulator interface.

2) Depletion Mode

When a negative bias ($V_{GS} < 0$) is applied to the gate (Figure 2.2.2 (b)), E_F in the metal is raised compared to E_F in semiconductor leading the band to band upwards. The concentration of electron is decreased and a depletion region is created in the vicinity of semiconductor/insulator interface. This is called the depletion mode. As the negative gate bias increases, the semiconductor surface can bend up more causing the increase of hole concentration at the surface. However, the transport of holes is negligible due to a huge sub-gap density of states ($10^{20}/\text{cm}^3$) near the valence band of Zinc based oxide film.²⁸

3) Accumulation Mode

When a positive bias ($V_{GS} > 0$) is applied to the gate (Figure 2.2.2 (c)), E_F in the metal is lowered compared to E_F in semiconductor and cause the downward band bending. The electrons are drawn towards the semiconductor/insulator interface and accumulated at the semiconductor/insulator interface, resulting in the increase in electron concentration and formation of the active channel layer near the semiconductor/insulator interface. This is the accumulation mode of the n-type TFT.

If the drain to source voltage (V_{DS}) is increased from 0 V, electrons are injected from the source electrode into the channel and drift toward drain electrode. Here, the current (I_{DS}) increases linearly with V_{DS} and comes to saturation current after pinch-off.

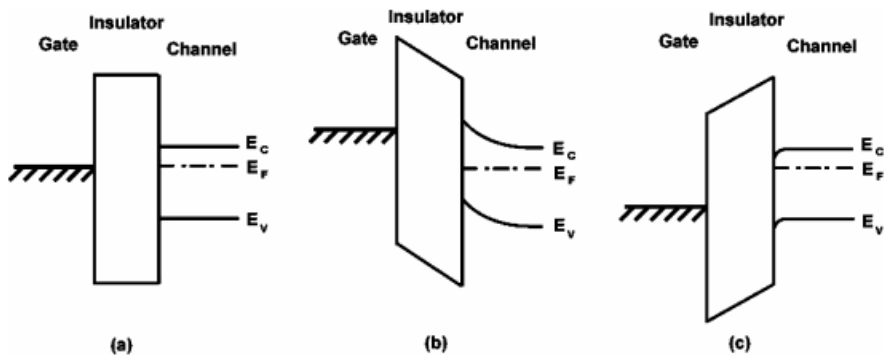


Fig. 2.2.2 Energy band diagrams as viewed through the gate for several biasing conditions: (a) equilibrium, (b) depletion ($V_{GS} < 0 \text{ V}$), and (c) accumulation ($V_{GS} > 0 \text{ V}$).²⁷

2.2.3. Characteristic parameters of transistor

The TFT characteristic parameters are usually extracted from the transfer characteristics, where the drain current (I_{DS}) is plotted against the gate voltage (V_{GS}) for various drain voltages (V_{DS}), as shown in fig. 2.2.3. Based on MOSFET drain current equations, drain current on/off ratio ($I_{on/off}$), channel mobility (μ), threshold voltage (V_{th}), subthreshold swing (S) can be extracted. These parameters represent the device performance.

1) Channel mobility (or device mobility)

This is most often used for device characterization channel mobility is related with the carrier transport in a channel layer, affected by several scattering mechanisms, such as lattice vibrations, ionized impurities, grain boundaries and other structural defects.²⁹ Because of the movement of carriers is constrained to a narrow channel region close to the interface, additional sources of scattering should be considered, such as Coulomb scattering from dielectric charges and surface roughness scattering.

There are various methods of defining the device mobility. In this study, field effect mobility (μ_{FE}) and saturation mobility (μ_{sat}) are used. μ_{FE} is extracted from

linear region ($V_D < V_G - V_T$) and small drain voltage (~ 0.1 V), and μ_{sat} is extracted from saturation region ($V_D > V_G - V_T$) and large drain voltage (5~15 V). The MOSFET equations for thin film transistor are shown following,

in linear region, $V_D < V_G - V_T$

$$I_{D,\text{linear}} = \frac{W}{L} \mu_{\text{eff}} C_{\text{ox}} (V_G - V_T) V_{\text{DS}}$$

$$g_m = \left. \frac{\partial I_{\text{DS}}}{\partial V_{\text{GS}}} \right|_{V_{\text{DS}}=\text{const.}} = \frac{W}{L} \mu_{\text{eff}} C_{\text{ox}} V_{\text{DS}}$$

Field effect mobility (μ_{FE} or μ_{eff}) is extracted using,

$$\mu_{\text{FE}} = \frac{L g_m}{W C_{\text{ox}} V_{\text{DS}}}$$

in saturation region, $V_D > V_G - V_T$

$$I_{D,\text{sat}} = \frac{W \mu_{\text{sat}} C_{\text{ox}}}{2L} (V_G - V_T)^2$$

Saturation mobility (μ_{sat}) is extracted using,

$$\mu_{\text{sat}} = \frac{2Lm^2}{WC_{\text{ox}}} \quad m : \text{slope of } \sqrt{I_{\text{D,sat}}} - (V_{\text{G}} - V_{\text{T}})$$

where L is the channel length, W is the width, and C_{ox} is the gate capacitance per unit area. By the device mobility, the current transfer performance of the transistor can be evaluated.

2) Subthreshold swing (SS)

The subthreshold swing (SS) are estimated using a log plot of the transfer curve. SS can be an useful parameter of how effectively the TFTs turn on by the gate bias, and reflects the value of V_{GS} required to obtain a 10 times larger I_{DS} in the subthreshold region (i.e. $V_{\text{GS}} < V_{\text{th}}$). The SS value is also dependent on V_{GS} as shown, and usually the smallest value of SS is taken. Following equations are the definition of the SS value.

$$\begin{aligned} \text{SS} &= \frac{1}{\text{slope}} = \frac{V_2 - V_1}{\log(I_{\text{DS2}} - I_{\text{DS1}})} \\ &= \ln 10 \cdot \frac{K_{\text{B}}T}{e} \left(1 + \frac{eD_{\text{sg}}}{C_{\text{G}}} \right) \\ &= 59.5 \left(1 + \frac{eD_{\text{sg}}}{C_{\text{G}}} \right) \quad (\text{meV decade}^{-1} \text{ at } 300\text{K}) \end{aligned}$$

The SS value also provides important information about the quality of a TFT. It is related to the trap density (D_{sg}) in the band gap (subgap traps) at the Fermi level. From above equation, the SS value of a metal-insulator-semiconductor (MIS)-type FET should be larger than $59.5 \text{ mVdecade}^{-1}$ at 300K and a steeper transfer curve should correspond to a higher-quality channel with fewer defects. D_{sg} value includes contributions from the bulk channel region N_{ss} and the interface D_{it} , and it is important to separate them to clarify the origin of the defects.

3) Drain current on/off ratio ($I_{on/off}$)

This is a parameter for switching device and defined as the ratio of the on current to off current. Figure 2.2.3 (a) shows the transfer characteristics of n-type oxide TFTs. In the case of high performance TFT, the TFT shows about $10^7 \sim 10^8$ of $I_{on/off}$.

3) Threshold voltage (V_{th})

There are several methods of V_{th} extraction. In this study, constant current method was used for V_{th} extraction. The V_{th} was defined as the gate voltage which induces a drain current of $L/W \times 10 \text{ nA}$ at $V_{DS} = 10.1 \text{ V}$ from transfer curve (the

L/W is a correction term that eliminates the effect of channel length and width on the drain current). This method is frequently used in display industry because the analog driver in the actual unit pixel of AMOLED panel is loaded between $1\mu\text{A}$ and 1nA . Here, the roughly $1\mu\text{A}$ and 1nA are needed to embody the full-on and black gray scale for AMOLED devices, respectively. Although this type of V_{th} definition does not have a unique physical meaning, the gate voltage to induce a drain current of 10nA can be a very useful guideline for the panel design as well as the process control.

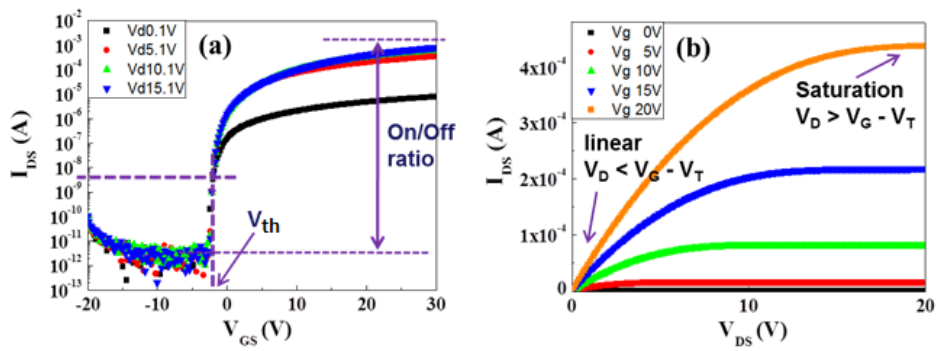


Fig. 2.2.3 Representative (a) transfer and (b) output characteristics n-type oxide-TFTs

2.3. Instability of oxide TFTs

2.3.1. Instability under stress measurement

Achieving the stability of oxide TFT is the most important issue in this field. In real operation environment (inside of display or electronic product), the device undergoes various external stress, such as electrical bias, light illumination, high or low temperature and mechanical stress, *etc.*, for a long time. These stress factors can induce degradation of device performance. By the stresses, off current can be increased, and SS value or mobility can be deteriorated. Especially, under the stress condition, the V_{th} shift phenomenon of transistor is the crucial problem for product application, which is not resolved clearly until now. Eventually, the degradation of device performance causes malfunction or defect of product. For evaluating the device instability, several stress measurement methods are being used.

1) Positive bias stress

Applying positive gate bias to TFT is called positive bias stress (PBS) measurement. In fig. 2.3.1, J.-M *et al.*³⁰ applied a gate bias of up to 15 V and measured the change of the device parameters, such as device mobility, threshold

voltage, and subthreshold swing. The bias stress produced a parallel shift of V_{th} to the positive direction and no or little change in μ and S.S. values. Generally, as shown in fig. 2.3.1, oxide TFT shows positive V_{th} shift under positive gate bias stress, and shows negative V_{th} shift under negative gate bias stress. For the case of stress under gate and drain biases at the same time, Fujii et al. reported an increase of V_{th} shift with an increasing gate bias.³¹ However, the shift was not strongly dependent on the drain bias. Positive bias stressing has usually been tested for the AMOLED applications, because the TFT must supply a stable current for the entire operating time of the OLED. In such a case, instability measurement is generally carried out under a $V_g=V_d>0$ condition in order to supply a constant current. A similar phenomenon was observed for constant current stress experiments, which means the observation of only a parallel V_{th} shift.^{32 33} An instability mechanism of the conventional a-Si TFT under bias stress was interpreted by two models.^{34 35} One was the defect creation in a channel and the other was trapping in a gate insulator or at the interface between the channel and the insulator. The former resulted in the degradation of mobility and S.S., while the latter showed only a parallel shift of V_{th} . Based on these observations, the instability of oxide TFTs under positive bias stress was also explained based on the charge trapping model.

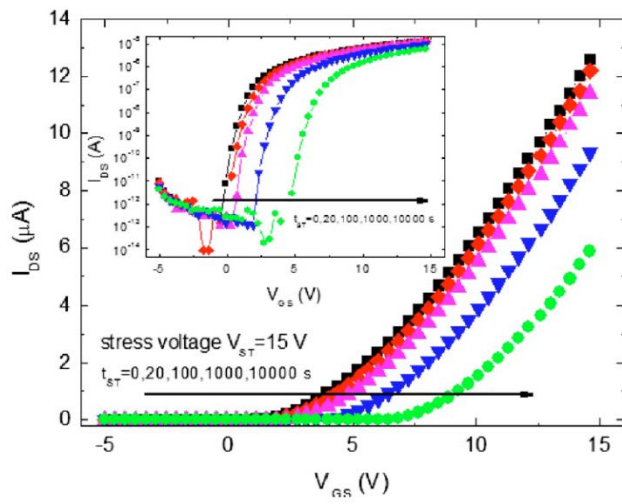


Fig. 2.3.1 PBS-induced V_{th} shift of *a*-IGZO TFTs. The inset shows the bias-stress-induced shift of $\log_{10} I_{DS}$ - V_{GS} curve.³⁰

2) Negative bias stress

In general, oxide semiconductors have n-type characteristics, so applying negative voltage at the gate is required for turning-off the device. In particular, the total duration of the negative gate bias applied on the switching transistor is larger than that of the positive gate bias by more than 500 times in the case of AMLCD products. For an AMOLED, the driving TFT must supply current for emission of light and requires high stability under positive bias stressing. However, switching the TFT is also required for the AMOLED as is exactly in the same bias situation as that of the AMLCD. Therefore, a high reliability with a negative bias stress is an indispensable requirement for operating an active matrix display. Figure 2.3.2 shows a negative V_{th} shift in transfer curve of an a-IGZO TFT.³⁶ Only the negative V_{th} shift occurred and degradation of SS or mobility was not induced. This result is often seen in NBS test and opposite to PBS test. Similar to the positive shift, the negative shift of V_{th} could be explained by hole trapping or positively charged defect trapping near the gate dielectrics. However, most oxide semiconductors are intrinsic n-type and contain little hole charge (in the valence band) to induce V_{th} shift by hole trapping process, so that the mechanism of positively charged defect (*e.g.*, oxygen vacancy) has been frequently proposed. Meanwhile, in the commercial AMLCD device, TFT experiencing a continuous pulsed gate voltage is

also exposed to the light, which is inevitable due to the presence of the back light unit underneath. Thus, the device degradation under a negative bias and illumination stress at the same time is a critical issue to be resolved. It will be discussed in next section.

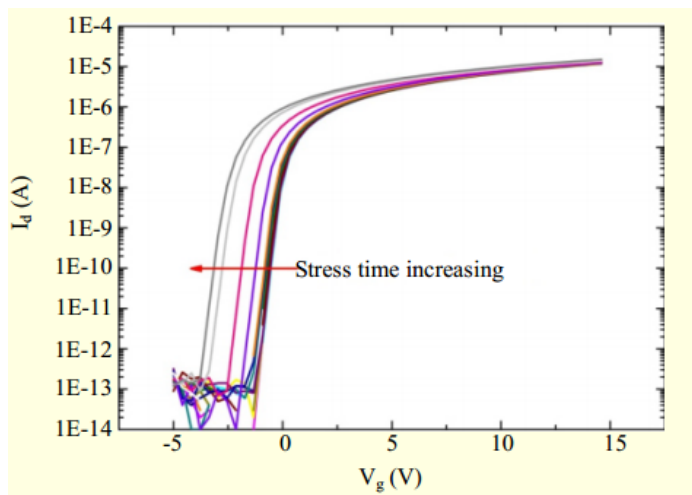


Fig. 2.3.2 NBS-induced V_{th} shift of a -IGZO TFTs.³⁶

3) Bias and illumination stress

Stressing of bias and light at the same time (bias illumination temperature stress, BITS) is a more realistic test scheme for display applications than stressing of only bias (bias temperature stress, BTS). In the case of a conventional a-Si TFT, the shift of transfer curve by bias stressing and the increase of off-current by illumination stress could be observed. However, no drastic degradation under simultaneous bias and light stresses was found compared to under individual stress. In contrast for the oxide semiconductor TFTs, the shift of V_{th} was accelerated under BITS. Figure 2.3.3 shows the evolution of the transfer curve under BTS and BITS, respectively.³⁷ For the positive bias stress, there was little difference between under PBS and PBIS. However, the transfer curve moved to the negative direction fast under NBIS, while no remarkable change was observable under NBS for negative bias stress. Since n-type oxide semiconductors have negligible holes in the valence band, hole trapping in a gate insulator or at the interface between the semiconductor and the gate dielectric is extremely difficult even under the negative gate bias. However, abundant holes could be generated by light exposure. Drift of those toward the gate insulator and subsequent trapping by the negative electric field would result in remarkable shift of V_{th} . In many case, severe V_{th} shift occurs under NBIS as seen in fig. 2.3.3, and NBTS (negative bias temperature stress) also cause large V_{th} shift.

On the other hand, PBS or PBIS-induced V_{th} instability can be considerably reduced by appropriate back channel passivation. In this regard, NBIS or NBTS instability is the more critical problem, so in this dissertation, NBIS and NBTS-induced V_{th} instabilities of IZO TFTs are mainly investigated.

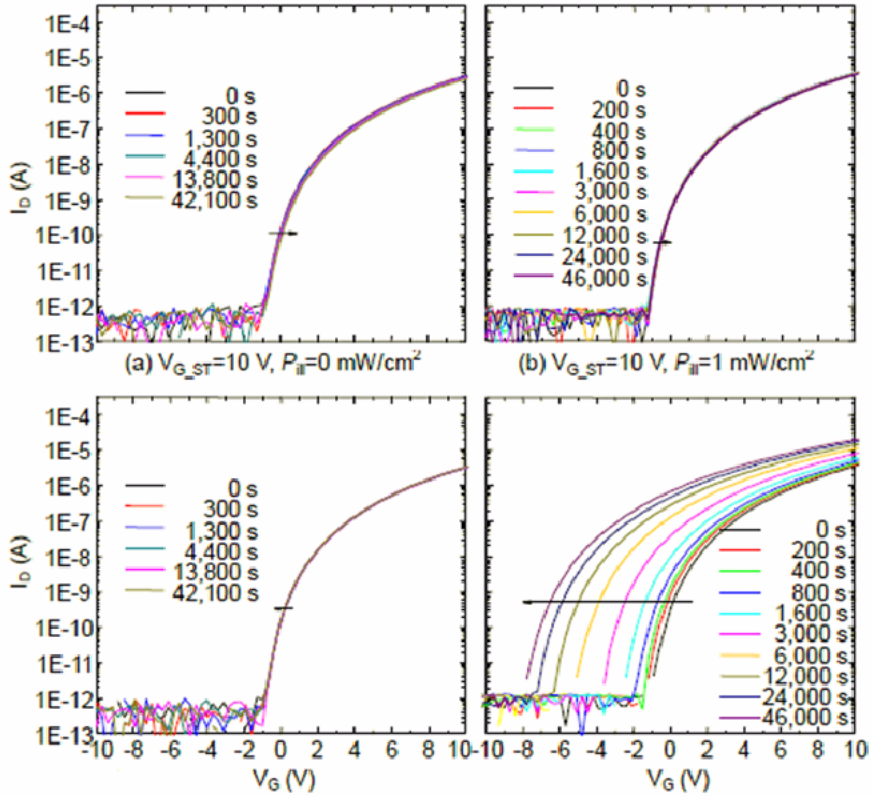


Fig. 2.3.3 Changes in the I_{DS} - V_{GS} characteristics of ZnO TFTs under (a) PBS, (b) PBIS, (c) NBS, and (d) NBIS conditions.³⁷

2.3.2. Origin of instability

There are many factors affecting the V_{th} instability in oxide TFTs under stress conditions. Gate insulator quality, channel/insulator interface property, defect density in channel or insulator layer, passivation, etc., these factors determine the device stability, so control of the material and structural property of the device and an investigation of the V_{th} degradation mechanism are very important. The NBIS (or NBTS) instability is the crucial problem which is not resolved until now, so here, only the origins of NBIS-induced instability will be discussed. By many research for instability of the device, largely, three mechanisms for V_{th} instability under NBIS condition have been proposed, which are ambient effect, hole trapping, and oxygen vacancy related instability.

1) Ambient interaction in back-channel surface

It is well known that metal oxides are surface sensitive to molecules in an ambient atmosphere.^{38 39} The adsorption of oxygen onto the surface of the metal oxides introduces an acceptor-like surface state. When oxygen chemisorbs on the surface, it is negatively charged by capturing an electron from the conduction band, and consequently, surface of oxide semiconductor is depleted. On the other hand,

H₂O acts as a donor-like surface state based on a similar explanation. For instance, Jeong et al. discussed how bias stressing is able to lead to field induced adsorption and desorption of O₂ or H₂O and how it affects device instability by varying the carrier concentration of the oxide semiconductors (fig. 2.3.4).⁴⁰ Other experimental results for the effects of ambience was reported by Lee *et al.*⁴¹ They carried out a BITS test in a humid environment. As the humidity of environment increased, V_{th} moved to the negative direction faster. In that report, it was suggested that water molecules supplied by the ambient condition generated metastable gap states which brought about a large number of trapped electrons and eventually an increase of hole carriers in the oxide semiconductors, and finally the devices exhibited a negative shift of the threshold voltage. To improve stability by protecting the device from the environment, a passivation layer becomes one of the key parameters. SiO₂ film and Al₂O₃ were suggested as a superior passivation layer. However, not only stability of the device but of the interconnection should be considered in selecting the passivation layer.

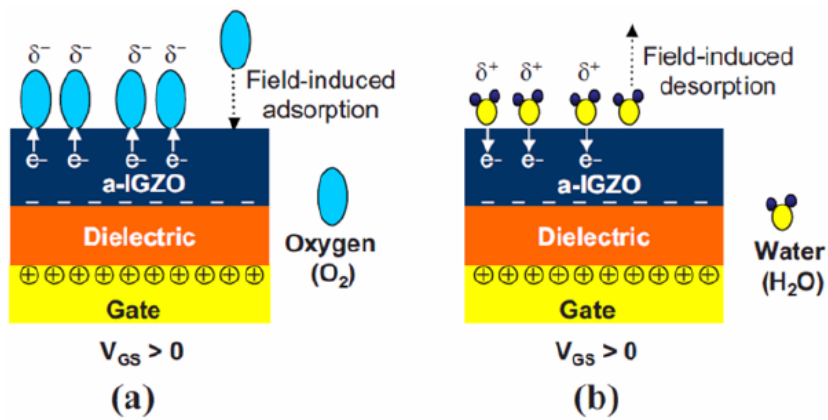


Fig. 2.3.4 (a) Schematic showing the electric-field-induced adsorption of oxygen molecules from the ambient atmosphere under NBS. (b) Schematic showing the electric-field-induced desorption of water molecules into the ambient atmosphere under PBS.⁴⁰

2) Hole trapping (or charge trapping)

Hole trapping (or charge trapping) model can be easily expected under NBS and NBIS condition, which induces negative V_{th} shift in transfer characteristic of oxide TFTs. In the NBS condition, of course, the positive charge (hole) is attracted toward gate electrode direction, but the oxide semiconductors are intrinsic n-type property and have few valence band hole carriers, so NBS cannot induce a large V_{th} shift. However, in the NBIS condition, a large amount of hole carriers can be generated by band-to-band excitation or trap assisted excitation because of light illumination. If a sufficient photon energy ($>3.1\sim 3.4$ eV) is irradiated, band-to-band excitation would occur, while a smaller energy could induce trap-assisted excitation by subgap electron traps. Electrons are localized at the subgap traps and holes are transported to traps in a channel-gate insulator interface or a gate insulator by positive gate bias. Schematic of the process is shown in fig. 2.3.5.⁴² The attracted holes near gate insulator can be trapped in two regions, that is, channel/insulator interface or insulator inside. The trapped holes in insulator inside, at first, can be trapped in shallow level traps, and then can be migrated to deep level traps.

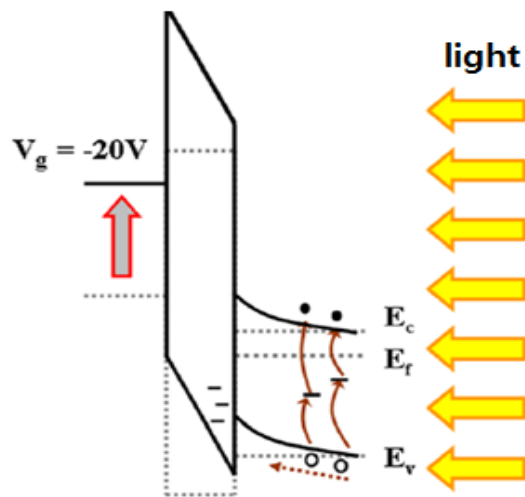


Fig. 2.3.5 Photo-generated hole trapping in an NBIS condition.⁴²

3) Oxygen vacancy transition model

Exist of the oxygen vacancy is inevitable in n-type oxide semiconductor. Most of the n-type oxide semiconductors have an oxygen deficient composition from deposition step, which is the origin of intrinsic n-type conductivity of the oxide semiconductors. In this regard, the common device instability (NBIS induced V_{th} shift) would be attributed to the oxygen vacancy. In many experimental and simulation research, it was known that the oxygen vacancy defect plays a critical role in determining the V_{th} instability under the application of NBIS conditions.^{43 44} The photon irradiation onto the oxide bulk film would excite the pre-existing neutral oxygen vacancies, V_O , to the V_O^{2+} charged state. A negative shift in V_{th} can be expected because such a photo-transition contributes to two delocalized electrons into the conduction band. On the other hand, the ionized V_O^{2+} defect itself can migrate toward the channel/gate insulator interface by the attractive coulombic force, which is due to the negative bias stress applied to the gate electrode. Both processes can result in a negative V_{th} shift under NBIS conditions. And there is an energy barrier (0.2-0.3 eV) between V_O^{2+} and V_O , the V_O^{2+} is hindered to return to V_O state, which can result in the persistent photo-conductivity (PPC). The explanation of the oxygen vacancy model is depicted in fig. 2.3.6.⁴⁵

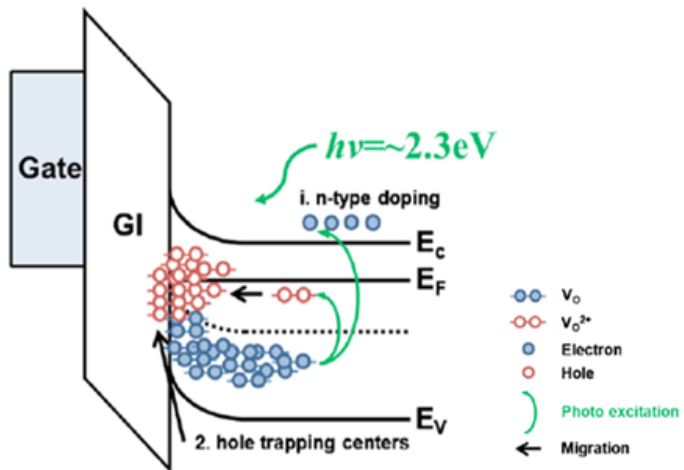


Fig. 2.3.6 V_{th} degradation process under an NBIS condition by oxygen vacancy transition model.⁴⁵

2.3.3. Stretched exponential equation

Stretched exponential equation is the formula that can describe the V_{th} shift behaviors of transistors, that is, the V_{th} instability of the devices can be evaluated numerically by activation energy values. The equation was originated to describe V_{th} degradation in a-Si:H TFTs. Now, the equation is being applied to oxide TFTs as well as the former devices. Following is the equation (eq.1):

$$|\Delta V_{th}(t)| = V_0 \left\{ 1 - \exp \left[- \left(\frac{t}{\tau} \right)^\beta \right] \right\}$$

where τ is the relaxation time, β is the dispersion parameter of the barrier energy height, and V_0 is $V_{GS} - V_{th0}$ (V_{GS} is the applied gate bias stress). The relaxation time (τ) is activated thermally according to the following equation (eq.2):

$$\tau = v^{-1} \exp \left(\frac{E_\tau}{k_B T} \right)$$

where E_τ is the activation energy for the process, v is the frequency pre-factor for emission over the barrier, T is the absolute temperature, and k_B is the Boltzmann constant. Using eq.1, $t - \Delta V_{th}$ result of BTS tests can be fitted and the parameters of τ , β can be obtained. Furthermore, by the BTS tests for various temperatures the activation energy barrier related to V_{th} degradation processes can be estimated. The activation energy values can provide more specific information on the V_{th} shift mechanism than simple stress measurements. Figure 2.3.7 shows an example of the fitting process for an IZO TFT using the stretched exponential equation.

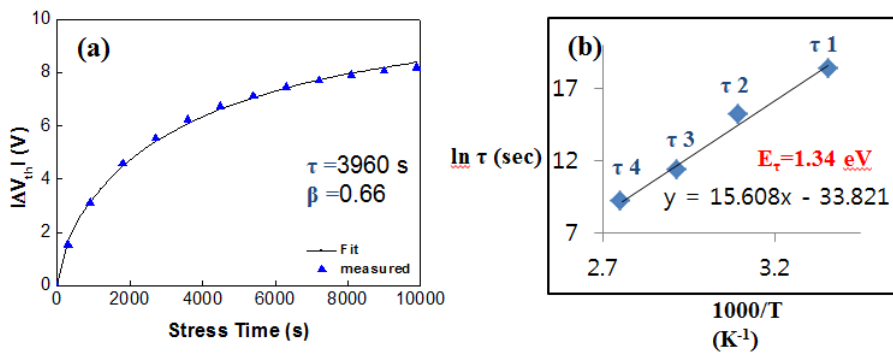


Fig. 2.3.7 Examples of stretched exponential fit: (a) $t - \Delta V_{th}$ fit, (b) $\tau - 1000/T$ fit for obtaining an activation energy value.

Chapter 3. Anomalous behavior of negative bias illumination stress instability in an indium zinc oxide transistor: a cation combinatorial approach

3.1. Introduction

Metal oxide thin film transistors (TFTs) have been studied extensively as switching devices in active-matrix (AM) liquid crystal displays (LCDs), organic light emitting diodes (OLEDs) and flexible displays on account of their high field-effect mobility ($>10 \text{ cm}^2/\text{Vs}$), high electrical uniformity over a large substrate size, and low processing temperature. InGaZnO (IGZO) is one of the most promising channel materials in TFTs, which typically have a mobility ranging from 10 to 25 cm^2/Vs ,^{17 46 47 48} even with an amorphous structure. Although several IGZO TFT-driven prototype devices, such as 19" QFHD AMOLEDs⁴⁹, 37" FHD AMLCD⁵⁰, and 6.5" flexible AMOLEDs⁵¹, have been demonstrated, there is still a stringent requirement for a high mobility exceeding 30 cm^2/Vs , which will enable a rapid switching speed ($\geq 240 \text{ Hz}$), high-resolution ($>200 \text{ pixel per inch}$), and large active-matrix panel size ($>50 \text{ inch}$). For this reason, some attention should be paid to In_2O_3 -based oxide TFTs because indium-rich oxide can have a higher mobility (>30

cm²/Vs).⁵²

Although the fabrication of In₂O₃-based oxide TFTs with high mobility at low temperatures has been reported^{53 54}, little is known about the photo-bias instability of the resulting IZO TFTs. In the case of silicon-based TFTs, the photo-bias instability depends strongly on the crystalline structure of channel Si. Amorphous Si TFTs suffer from light-induced meta-stability due to the Staebler-Wronski effect.⁵⁵ In contrast, poly-crystalline Si TFTs exhibit stable behavior against light and bias stress. Despite its importance, the effect of the crystalline structure on the photo-bias instability of metal oxide TFTs has not been studied. It is well known that the threshold voltage (V_{th}) degradation by the application of simultaneous bias and light stress is more severe for negative bias illumination stress (NBIS) than for positive bias illumination stress.⁵⁶ For this reason, NBIS instability of metal oxide TFTs have been intensively investigated^{57 58 59 60}. Oxygen vacancy defect in metal oxide semiconductor is suggested to be origin for NBIS instability of oxide TFTs.⁵⁹

60

In this study, the fabrication of high performance TFTs with an InZnO (IZO) channel layer was carried out using a co-sputtering method. The effect of the indium content on the negative bias illumination stress (NBIS) instability as well as the device performance of the IZO TFTs is described in detail. Although the NBIS instability of the IZO TFTs is expected to deteriorate with increasing In content, a

local minimal value was observed for transistors with an indium fraction of approximately 77 at. % in terms of the negative V_{th} shift during the application of NBIS. This anomalous behavior was attributed to an abrupt poly-crystalline to amorphous phase transition.

3.2. Experimental

The fabricated IZO TFTs have a bottom gate and top contact configuration. A highly-doped p-type silicon wafer was used as the gate electrode. As a gate insulator, a 100-nm-thick SiO₂ layer was grown by wet thermal oxidation. Subsequently, 16-nm-thick IZO channel layers with different In fractions of $[\text{In}]/[\text{In}+\text{Zn}]$ were prepared by radio-frequency (rf) magnetron co-sputtering using a ZnO target and In₂O₃-ZnO (90:10 wt%) target. The targets were placed approximately 15 cm from the substrate. The input rf power to the ZnO target was fixed to 100 W, whereas that to the IZO was varied from 0 to 240 W. The working pressure was 5 mTorr and the relative oxygen flow rate $[\text{O}_2]/[\text{Ar}+\text{O}_2]$ was maintained at 0.3. X-ray fluorescence (XRF) spectroscopy confirmed that the In fraction (referred to as $[\text{In}]/[\text{In}+\text{Zn}]$) was varied from 0 to 0.85 by controlling the IZO target power. The channel area was defined using a shadow mask during IZO film deposition, and 100-nm-thick ITO source/drain (S/D) electrodes were deposited at room temperature using the same sputtering system. The channel width (W) and length (L) of the fabricated TFTs were 1000 μm and 300 μm , respectively. Post-deposition-annealing (PDA) of the IZO TFTs was performed in air ambient at 350°C for 1 hour in a vertical-type tube furnace. The device structure and its fabrication flow are shown in fig.3.1.1. The electrical characteristics of the TFTs

were measured at room temperature using an HP 4155A semiconductor parameter analyzer. Synchrotron-based two-dimensional (2D) grazing-incidence X-ray diffraction (GIXD) of the IZO films with various In fractions were performed at the X9 beamline of the National Synchrotron Light Source (NSLS) at Brookhaven National Laboratory. Each sample was mounted on a two-axis goniometer on top of an x-z stage, and the scattering intensity was recorded using a 2D Mar CCD detector. The structural properties of the IZO films were double-checked by glancing angle X-ray diffraction (XRD, X'Pert PRO, PANalytical) using Cu K α radiation. The chemical state of the IZO films was examined by X-ray photoelectron spectroscopy (XPS, SIGMA PROBE, ThermoVG, U.K). The microstructures of IZO films were analyzed by scanning electron microscopy (SEM) and transmission electron microscopy (TEM).

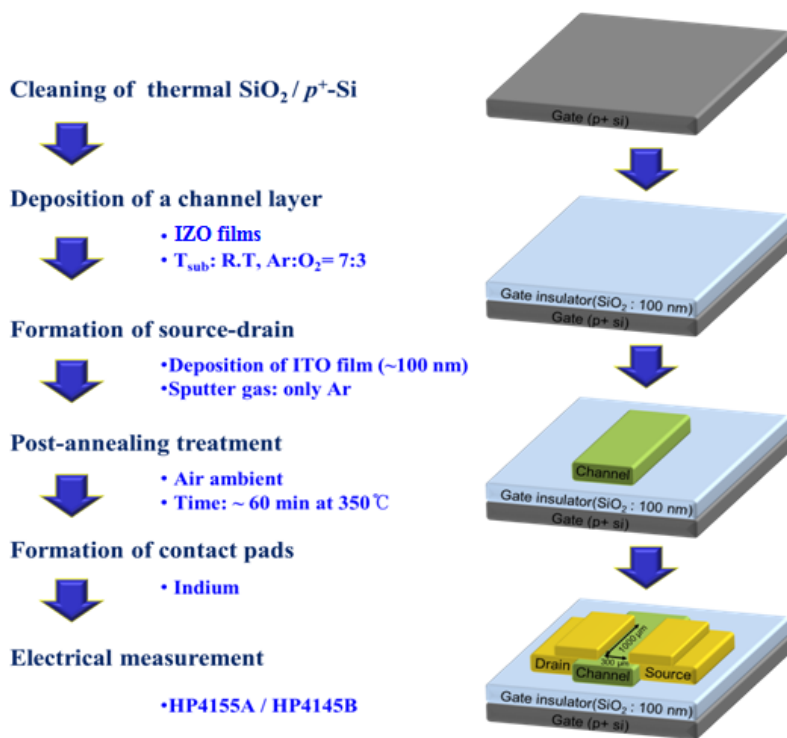


Fig. 3.2.1 Fabrication process flow of the IZO TFTs

3.3. Electrical properties of IZO films and TFTs

Figure 3.3.1 shows the representative transfer characteristics of various IZO TFTs. The field-effect mobility (μ_{FE}) was determined by the maximum transconductance at a drain voltage (V_{DS}) of 0.1V.⁶¹ The threshold voltage (V_{th}) was defined as the gate voltage (V_{GS}) that induces a drain current of $L/W \times 10$ nA at $V_{DS} = 10$ V. The sub-threshold gate swing ($SS = dV_{GS}/d\log I_{DS}$ [V/decade]) was extracted from the linear part of the $\log(I_{DS})$ vs. V_{GS} plot. The pure ZnO TFTs exhibited a μ_{FE} , SS value and V_{th} of 1.1 cm²/Vs, 2.4 V/decade and 2.3 V, respectively. The μ_{FE} value increased monotonically with increasing the In₂O₃ content in the IZO channel layer. Therefore, the device with the In_{0.77}Zn_{0.23}O channel prepared at an IZO target power of 160 W exhibited a high μ_{FE} and V_{th} of 31.0 cm²/Vs and -1.2 V, respectively. The highest mobility (41.0 cm²/Vs) was observed for the device with an In_{0.85}Zn_{0.15}O channel prepared at an IZO target power of 240 W. The SS factor, which is often used as an indicator for the tailing trap density, was improved with increasing In content, as listed in Table 3.3.1. The physical role of the In cation has been identified as the mobility enhancer and carrier generator because of its large 5s orbital radius.²⁶ This observation is consistent with the experimental and theoretical calculations in the literature. In the transfer characteristic of the TFTs, peculiarly, a TFT with 16 at.%In showed a huge negative V_{th} value of -14 V. This unexpected

result was consistent with Hall measurement data of the IZO films in fig. 3.3.2. Most of the IZO films with In content below 52 at.%, the electrical properties could not be measured in Hall measurement, because the films had low conductivity below measurement limit. However, only an IZO film with 16 at.%In could be measured, which showed the highest electron concentration of $1.39 \times 10^{18} / \text{cm}^3$ among the IZO films. Because of its high electron concentration, the TFT with 16 at.%In needed highly negative gate voltage for off state and had slightly increased off current of $\sim 10^{-11}$ A. For IZO films with low In content, it has been often reported that In atom exists as a either interstitial or substitutional defect in ZnO-based crystal structure, which can act as a significant electron donor. The cause of the high electrical property of the IZO film with 16 at.%In will be discussed in section 3.6 through analyzing crystallographic information.

When In content was > 52 at.%, Hall measurement result shows an increase tendency of the n and μ_{Hall} with In content, which is consistent with the transfer characteristic of the TFTs. The n values were $10^{17} \sim 10^{18} / \text{cm}^3$, and the appropriate electron concentration enabled the IZO films to operate as semiconducting channel layers. Generally, the IZO is known as a conducting material, but in this study an addition of O_2 gas in sputtering process and the appropriate setting of annealing temperature (350°C) enabled to make the quite excellent semiconductor device.

When the In composition was > 77 at%, both n and μ_{Hall} are increased rapidly. It

is expected that in In content above 77 at%, large amount of oxygen vacancies were generated, and effect of percolation conduction was amplified by sufficient In content and homogeneous dispersion of In atoms in amorphous network structure.

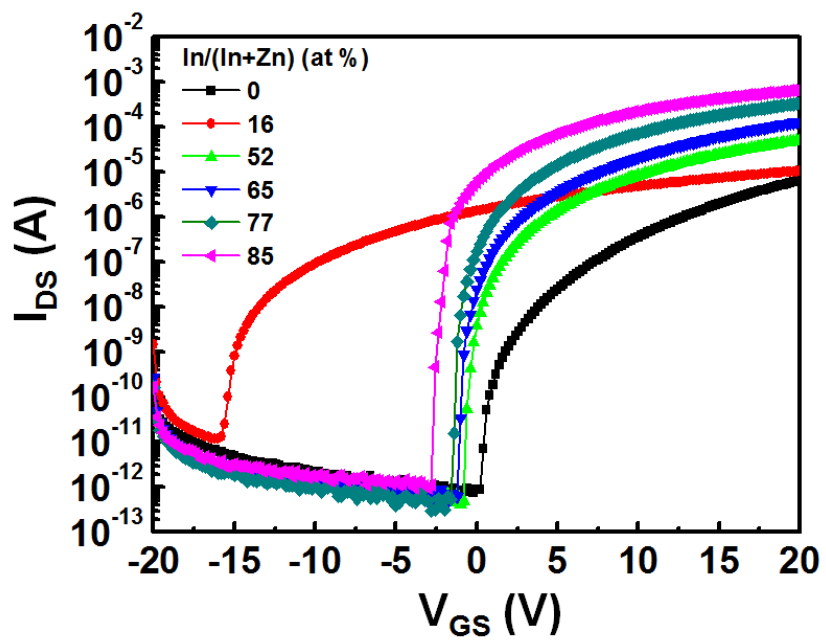


Fig. 3.3.1 Representative transfer characteristics of In_xZn_{1-x}O TFTs with different In fractions

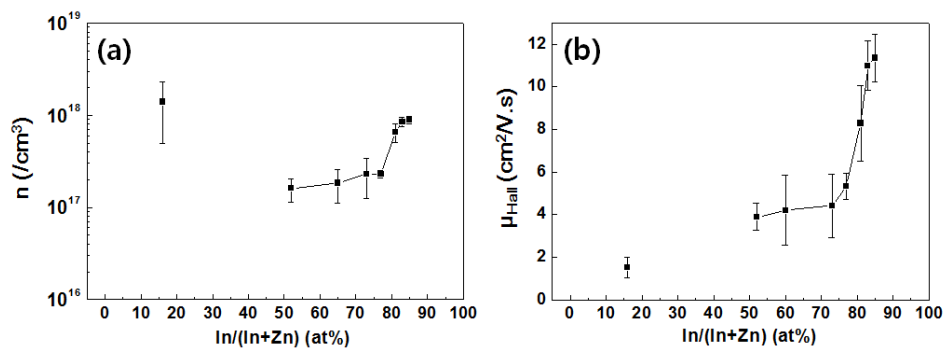


Fig. 3.3.2 (a) Electron concentration and (b) Hall mobility of $\text{In}_x\text{Zn}_{1-x}\text{O}$ films

Table. 3.3.1 Electrical characteristics of the TFTs based on $\text{In}_x\text{Zn}_{1-x}\text{O}$ films with different In contents

Samples	μ_{FE} [$\text{cm}^2\text{V}^{-1}\text{s}^{-1}$]	SS[Vdecade ⁻¹]	V_{th} [V]	$I_{\text{on}}/I_{\text{off}}$
ZnO	1.1	2.4	2.3	2.9×10^6
$\text{In}_{0.16}\text{Zn}_{0.84}\text{O}$	0.8	0.95	-14.0	8.6×10^5
$\text{In}_{0.52}\text{Zn}_{0.48}\text{O}$	7.2	0.42	-0.17	5.0×10^7
$\text{In}_{0.65}\text{Zn}_{0.35}\text{O}$	18.2	0.32	-0.62	1.2×10^8
$\text{In}_{0.77}\text{Zn}_{0.23}\text{O}$	31.0	0.22	-1.17	3.2×10^8
$\text{In}_{0.81}\text{Zn}_{0.19}\text{O}$	37.0	0.19	-1.5	4.9×10^8
$\text{In}_{0.85}\text{Zn}_{0.15}\text{O}$	41.0	0.20	-2.56	6.4×10^8

3.4. NBIS instability of IZO TFTs

The NBIS instability of the various IZO TFTs was examined. The devices were stressed under the following conditions: V_{GS} and V_{DS} were set to $V_{th} - 15$ V and 10 V, respectively, at room temperature, and the maximum stress duration was 2,000 s. The photons with a wavelength of ~ 600 nm, which was selected from a white-light halogen lamp through a band-pass filter, with an intensity of ~ 1.5 mW/cm² calibrated by photometry were used for the NBIS test. All IZO TFTs exhibited a negative parallel shift without a notable change in mobility and SS factor, irrespective of the In fraction (representative data shown in fig. 3.4.1). On the other hand, the amount of negative V_{th} shift was strongly dependent on the In fraction in the IZO channel layer. Figure 3.4.2 shows the variation of the NBIS-induced V_{th} shift as a function of the In content in the IZO thin film, which can be divided into three regions for convenience. In **Region I** (below In content of 55 at.%), the NBIS-induced ΔV_{th} increased with increasing In content: the $In_{0.52}Zn_{0.48}O$ TFT suffered from the largest V_{th} shift of -7.9 V. In contrast, the NBIS-induced V_{th} variations began to decrease at an In fraction of 60 at.% and a strongly suppressed to -3.65 V for the $In_{0.73}Zn_{0.27}O$ TFT (**Region II**). When the In composition was > 77 at.%, the NBIS induced V_{th} shift again increased monotonically and was almost proportional to the In fraction (**Region III**). As indicated in the figure, this trend is closely related to the crystalline state of the IZO films.

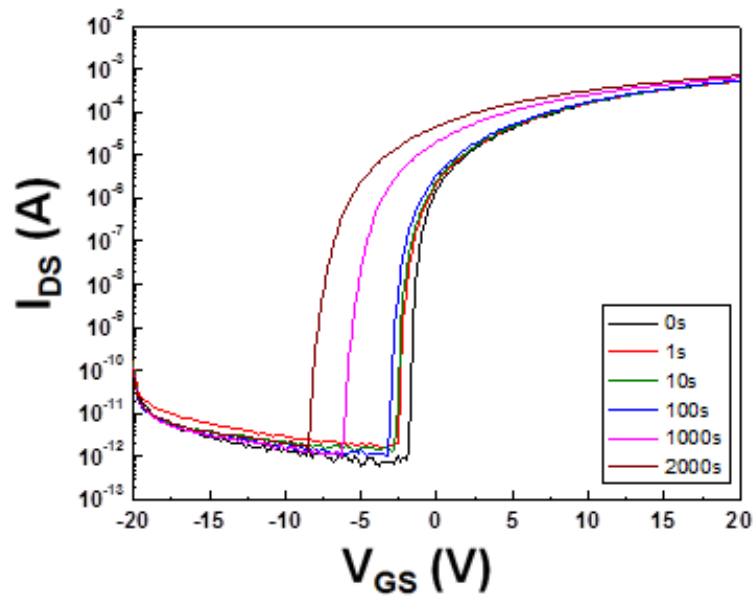


Fig. 3.4.1 Evolution of transfer characteristic of the IZO TFT (81 at.%In) under the NBIS condition, which shows a parallel shift of the curve

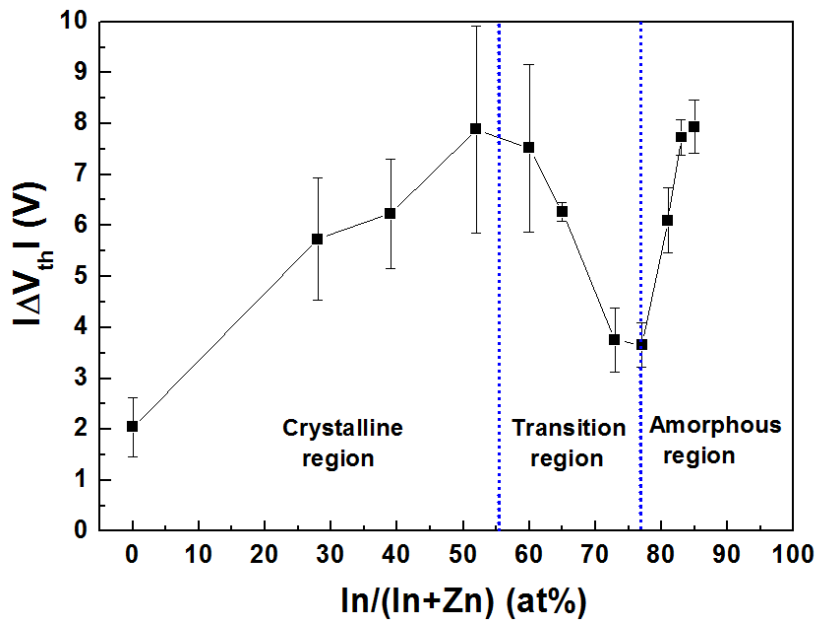


Fig. 3.4.2 Variation of the NBIS induced V_{th} shift as a function of the In content in IZO thin films.

3.5. Chemical state of IZO films

The chemical state of the IZO films was examined by XPS, to gain further insight into the effects of the In fraction on the NBIS instability of IZO TFTs. Figure 3.5.1 shows the O *1s* XP spectra (surface) of the (a) $\text{In}_{0.16}\text{Zn}_{0.84}\text{O}$, (b) $\text{In}_{0.52}\text{Zn}_{0.48}\text{O}$, (c) $\text{In}_{0.77}\text{Zn}_{0.23}\text{O}$, and (d) $\text{In}_{0.85}\text{Zn}_{0.19}\text{O}$ thin films. To calibrate the photoelectron binding energy, the adventitious C *1s* peak for C-C bonds was assigned to 284.5 eV. For accurate analysis, the O *1s* spectra were de-convoluted into three different components consisting of (i) a strong peak at a lower binding energy, which was assigned to the “lattice oxygen peak free from the influence of oxygen vacancies” (529.7~530.0 eV), (ii) a “lattice oxygen peak near the oxygen vacancy” (531.1 eV), and (iii) a “metal hydroxide peak” (531.9 eV).^{62 63 64} The relative area of the oxygen vacancy-related peak increased monotonically with increasing In content, and was 20.1, 23.6, 27.3 and 31.2 % for $\text{In}_{0.16}\text{Zn}_{0.84}\text{O}$, $\text{In}_{0.52}\text{Zn}_{0.48}\text{O}$, $\text{In}_{0.77}\text{Zn}_{0.23}\text{O}$ and $\text{In}_{0.85}\text{Zn}_{0.19}\text{O}$ thin films, respectively, as summarized in table 3.5.1. This effect of the indium incorporation on the oxygen vacancy defect concentration was consistent with the theoretical calculation, in that the formation energy of oxygen vacancies decreases with increasing number of neighboring In atoms in a multi-component metal oxide semiconductor.⁶⁵ Figure 3.5.2 shows XP spectra (surface) of metal cations of the four IZO films. In view of the peak

positions, the data of two metal atoms have quite different appearance. As In content increased, In $3d$ peaks moved toward lower binding energy, while Zn $2p$ peaks were at the same position. It indicates that In atoms became less oxidized and oxygen vacancies were formed near In atoms rather than near Zn atoms. This is also consistent with the theoretical calculation, and can be accepted as strong evidence proving experimentally the relationship between addition of In atoms and generation of oxygen vacancies.

To obtain more acceptable chemical states of the films, XPS measurement was carried out once again, after Ar etching to depth of ~8 nm, which enables confirming the channel bulk property. In the case of O $1s$ peaks, the shoulder region (531~532 eV) was decreased drastically for all the samples, so meaningful deconvolution analysis was not easy. However, in the case of metal cations, both binding energy positions of Zn and In were same with the surface result. Even after etching, In $3d$ XP spectra showed same shift toward low binding energy about 0.3 eV. The chemical shift of In $3d$ XP spectra would be attributed to charge state transition of In ion, accompanied by generation of oxygen vacancy sites with increasing In content in the IZO films. The In $3d_{5/2}$ peak can be de-convoluted with two sub peaks of 444.9 and 444.3 eV corresponding In³⁺ and In⁺ charge state, respectively.⁶⁶ The de-convolution results of In peaks are shown in fig. 3.5.3. As the peak position moved from 444.8 to 444.5 eV, the relative area of In⁺ increased

monotonically and was 16.9, 20.9, 38.2 and 48.8 % for $\text{In}_{0.16}\text{Zn}_{0.84}\text{O}$, $\text{In}_{0.52}\text{Zn}_{0.48}\text{O}$, $\text{In}_{0.77}\text{Zn}_{0.23}\text{O}$ and $\text{In}_{0.85}\text{Zn}_{0.19}\text{O}$ films, respectively. From the increase in lower oxidation state of In in etched XPS data, it can be confirmed that oxygen vacancy concentration increases with In content in the bulk region as well as the film surface. The increase in In atoms surrounding oxygen atoms would increase the possibility of the formation of V_{O} , which caused the displacement of In peak.

Recently, it was reported that the oxygen vacancy defect plays a critical role in determining the V_{th} instability under the application of NBIS conditions.⁵⁹ The photon irradiation onto the IZO bulk film would excite the pre-existing neutral oxygen vacancies, V_{O} , to the V_{O}^{2+} charged state.^{67 68} A negative shift in V_{th} can be expected because such a photo-transition contributes to two delocalized electrons into the conduction band.^{57 59} On the other hand, the ionized V_{O}^{2+} defect itself can migrate toward the channel/gate insulator interface by the attractive columbic force, which is due to the negative bias stress applied to the underlying gate electrode.⁵⁸ Both processes can result in a negative V_{th} shift under NBIS conditions. Based on the oxygen vacancy transition mechanism, it can be understood that the proportional relationship between the indium content and ΔV_{th} in **Regions I and III** (see fig. 3.4.2) is due to the increasing oxygen vacancy concentration. Nevertheless, **Region II** in fig. 3.4.2 cannot be explained by the oxygen vacancy mechanism.

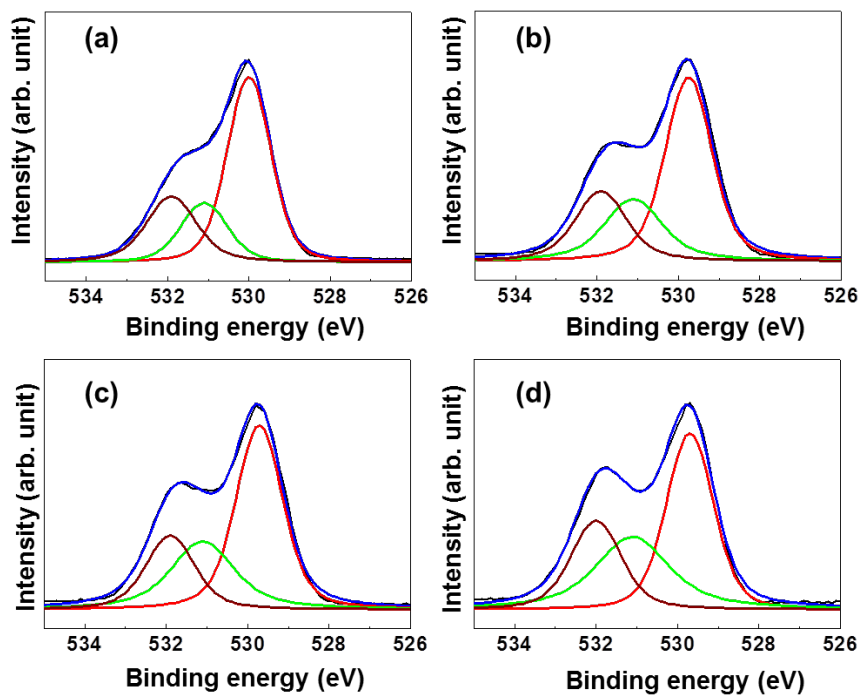


Fig. 3.5.1 O $1s$ XP spectra (surface) for the (a) $\text{In}_{0.16}\text{Zn}_{0.84}\text{O}$, (b) $\text{In}_{0.52}\text{Zn}_{0.48}\text{O}$, (c) $\text{In}_{0.77}\text{Zn}_{0.23}\text{O}$ and (d) $\text{In}_{0.85}\text{Zn}_{0.19}\text{O}$ thin films

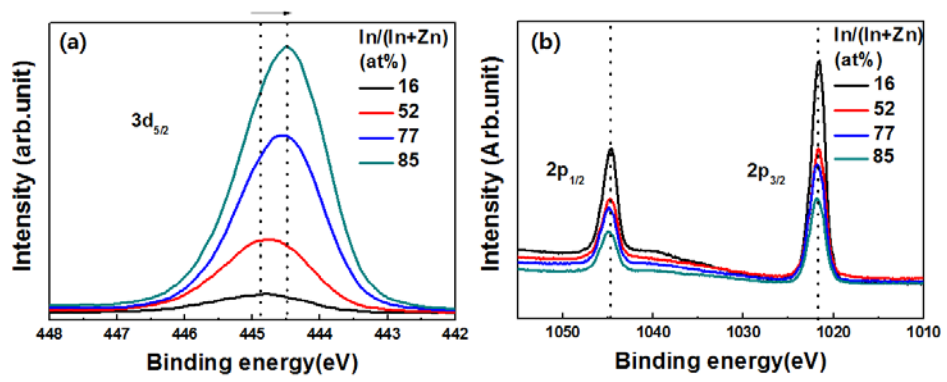


Fig. 3.5.2 XPS spectra (surface) of metal cations: (a) In $3d$, and (b) Zn $2p$

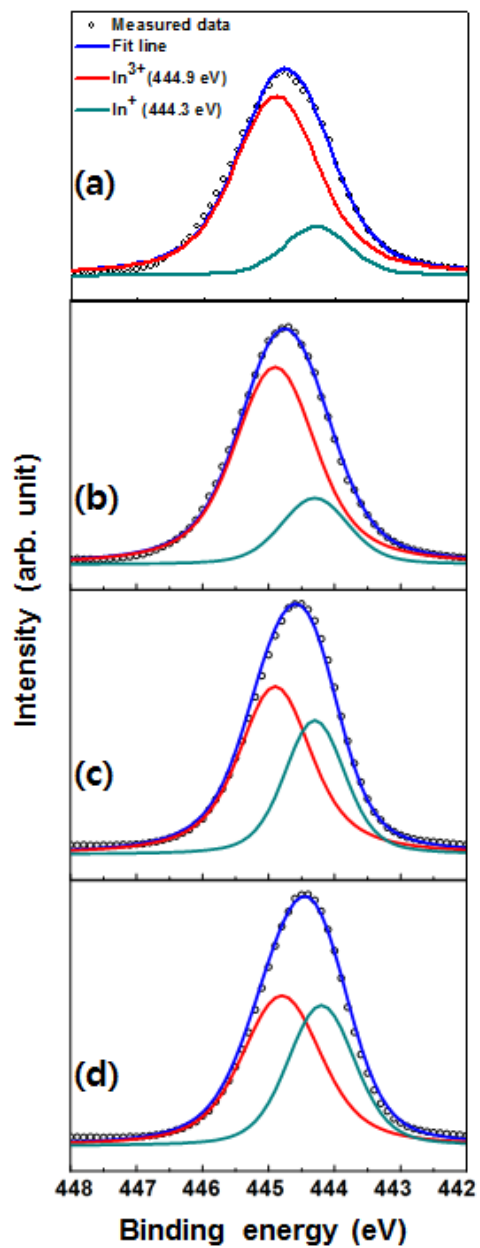


Fig. 3.5.3 In 3d XP spectra (bulk) for the (a) In_{0.16}Zn_{0.84}O, (b) In_{0.52}Zn_{0.48}O, (c) In_{0.77}Zn_{0.23}O and (d) In_{0.85}Zn_{0.19}O thin films

Table 3.5.1 Comparison of portions of the O *1s* peaks de-convoluted from the XP spectra of the InZnO thin films with different In contents

Samples	O <i>1s</i> peak [eV]		
	Lattice	Oxygen	
	Oxygen	deficient	Hydroxyl
	(529.8 ± 0.02)	(531.1 ± 0.01)	(531.9 ± 0.01)
In_{0.16}Zn_{0.84}O	0.565	0.201	0.234
In_{0.52}Zn_{0.48}O	0.535	0.236	0.229
In_{0.77}Zn_{0.23}O	0.511	0.273	0.216
In_{0.85}Zn_{0.19}O	0.443	0.312	0.245

Table 3.5.2 Comparison of portions of the In $3d_{5/2}$ peaks de-convoluted from the XP spectra of the InZnO thin films with different In contents

Samples	In $3d_{5/2}$ peak [eV]	
	In $^{3+}$ (444.9 ± 0.02)	In $^{+}$ (444.3 ± 0.01)
In_{0.16}Zn_{0.84}O	0.831	0.169
In_{0.52}Zn_{0.48}O	0.791	0.209
In_{0.77}Zn_{0.23}O	0.618	0.382
In_{0.85}Zn_{0.19}O	0.512	0.488

3.6. Crystalline structure of IZO films

Figure 3.6.1 shows the 2D GIXD patterns of the IZO films with different In fractions. The GIXD pattern for the pure ZnO film clearly showed a typical ring pattern corresponding to poly-crystalline ZnO with a hexagonal wurzite structure, as determined by $Q = 2.212, 2.396$ and 2.531 \AA^{-1} , corresponding to X-ray reflections of (100), (002) and (101) planes, respectively.⁶⁹ The thickness of ZnO and IZO films were approximately 16 nm based on the X-ray reflectivity profiles along the Q_z axis (see the inset in Fig. 3.6.1 (d)). Interestingly, strong X-ray reflections of the (002) and (101) planes were indicated at the Q_z (out-of-plane) and Q_{xy} (in-plane) axes, respectively, whereas the (101) reflection was tilted approximately 57° with respect to the (002) planes. This suggests that the prepared ZnO film has a columnar crystal structure with the c-axis normal to the film surface (See the inset in fig. 3.6.1 (a)): $a = 3.250 \text{ \AA}$ and $c = 5.242 \text{ \AA}$. On the other hand, the preferential crystal structure was lower for the IZO film with 52 at% In (See fig. 3.6.1 (b)). This is related to the incorporated In component, which weakened the crystal structure and orientation of ZnO. As a result, IZO films with a higher In content (65 and 73 at.%) showed only an amorphous hollow in the GIXR pattern (See fig. 3.6.1 (c) and (d)). This composition of the $\text{In}_{0.65}\text{Zn}_{0.35}\text{O}$ film corresponds to **Region II** showing an inverse relationship between the In fraction and NBIS-induced ΔV_{th} (fig. 3.4.2).

The In-dependent crystalline structures of the IZO films were also confirmed by glancing angle XRD, as shown in fig. 3.6.2. The diffraction peak position of ZnO (002) plane was not changed up to 16 at.%In. When In content was > 16 at.%, the Bragg angle for the (002) reflection decreased with increasing In fraction up to 65 at.%. Here, the constant peak position of low In content films indicates that the crystal structure of ZnO was maintained up to In content of 16 at.% and In atoms was included as impurities such as interstitial or substitutional defects. Considering the peak position was constant and the decrease in intensity, In atoms would exist in grain boundary region of poly crystalline structure of ZnO and restrain grain growth. Therefore, the exceptionally high electron concentration of the IZO film with 16 at.%In (See fig. 3.3.2) can be explained by the In atoms in grain boundary, expected to act as donor impurities. When the In composition was > 16 at.%, the diffraction peak was found at different angle position, which suggests the films had crystal structure of IZO. Crystalline IZO is known to have homologous crystal structures ($\text{In}_2\text{Zn}_k\text{O}_{k+3}$, $k = 3\sim 15$),⁷⁰ consisting of k ZnO layers separated by two InO layers. When In content was 65~77 at.%, phase transition from poly-crystalline to amorphous was also observed.

From the XRD results, it is proposed that a crystalline to amorphous phase transition suppresses the NBIS-induced V_{th} instability. The photo-excited V_O^{2+} defects migrate much faster in the two dimensional grain boundaries of poly-

crystalline IZO films than those in amorphous IZO materials. The dopants in highly doped Si or metal alloy were reported to diffuse much faster in poly-crystalline materials than amorphous ones due to the faster diffusion along the grain boundaries (data of ref.28 shown in fig. 3.6.3).^{71 72 73} Therefore, oxygen vacancy-related degradation can be distinguished clearly into two processes. The first process involves the photo-transition from V_O to V_O^{2+} , leading to the donation of two delocalized electrons in the conduction band. Because this transition rate is proportional to the pre-existing $[V_O]$ concentration, increasing indium incorporation amplifies the NBIS-induced V_{th} instability. The second process would be related to the field-assisted migration of V_O^{2+} defects toward the interface between the gate insulator and channel layer, which strongly depends on the microstructure of the IZO thin films. Therefore, the V_{th} shift during the application of NBIS should be determined by the concentration of pre-existing $[V_O]$ and migration of $[V_O^{2+}]$ defects. When the In fraction is low, the vacancy concentration is also low meaning that the NBIS instability is not severe. On the other hand, as the In fraction increases, the $[V_O]$ increases and the migration of $[V_O^{2+}]$ defects is enhanced along the grain boundaries provided the poly-crystalline structure of the IZO material is maintained. This is what occurs in the **Region I** of fig. 3.4.2. As the In fraction is increased further to 77 at.%, the film becomes amorphous so that the field-induced $[V_O^{2+}]$ migration is suppressed and the NBIS reliability is improved. With a further

increase in the In fraction, defect generation in the oxygen sites was enhanced further and the NBIS reliability degraded again. Based on the result of the indium content-dependent NBIS instability, it can be inferred that that the usage of grain boundary-free channel in IZO system improves NBIS stability while the high mobility is still preserved. Indium induced oxygen vacancy defect in IZO channel layer can be reduced by the intentional oxygen supply such as high pressure oxygen annealing,⁵⁹ oxygen plasma⁷⁴ and ozone treatment,⁷⁵ leading to further improvement in NBIS stability.

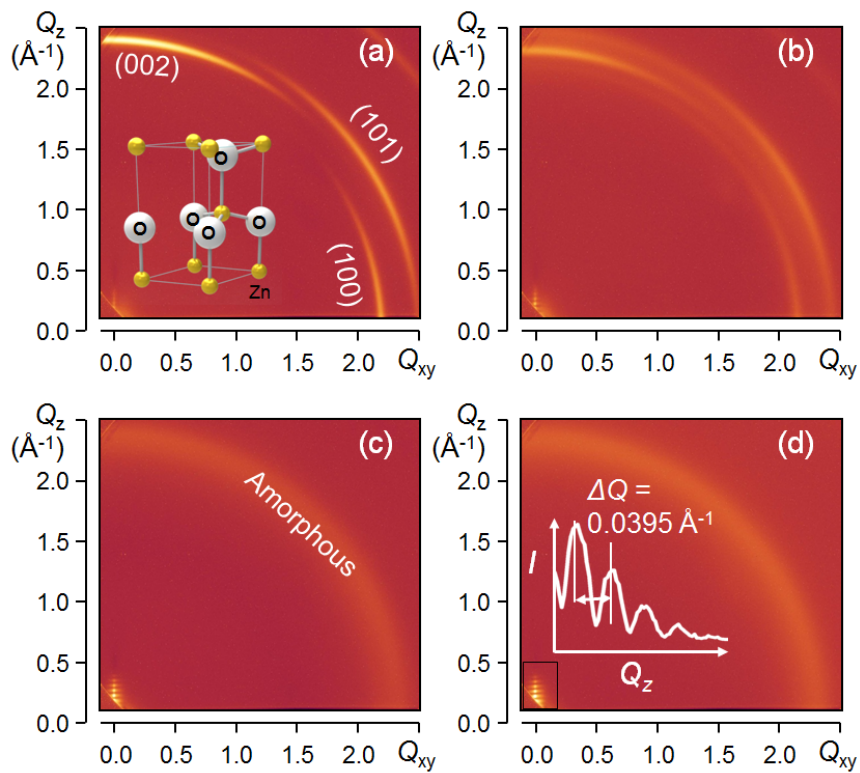


Fig. 3.6.1 2D GIXD patterns of the (a) ZnO, (b) $\text{In}_{0.52}\text{Zn}_{0.48}\text{O}$, (c) $\text{In}_{0.65}\text{Zn}_{0.35}\text{O}$, and (d) $\text{In}_{0.73}\text{Zn}_{0.27}\text{O}$ film.

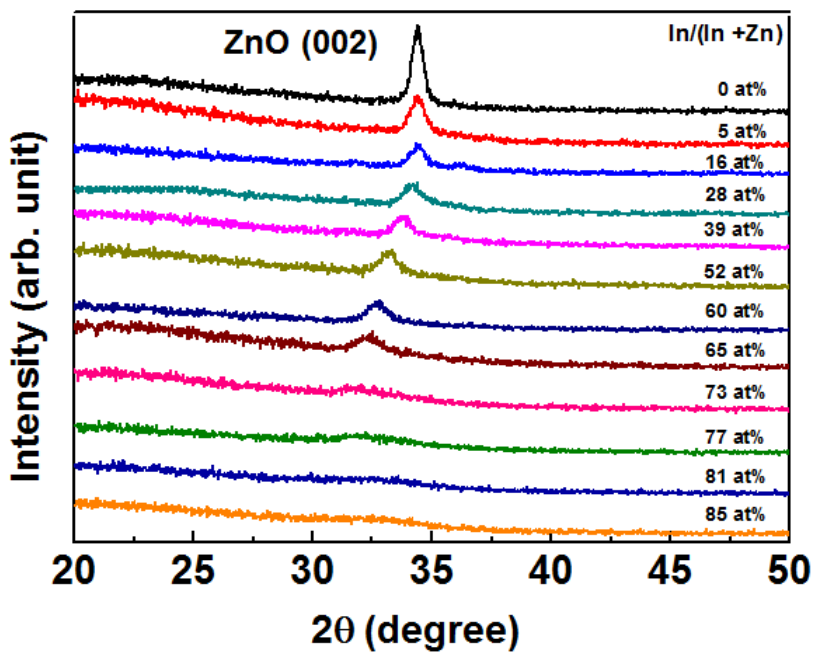


Fig. 3.6.2 Glancing-angle X-ray diffraction patterns of $\text{In}_x\text{Zn}_{1-x}\text{O}$ thin films with different In fractions on the SiO_2/Si substrate

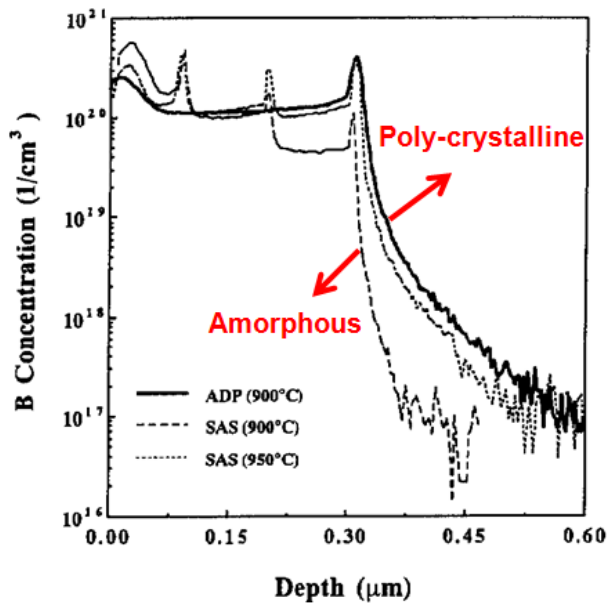


Fig. 3.6.3 Boron concentration as a function of depth in amorphous and poly-crystalline Si after ion implantation ⁷¹

3.7. Microstructure of IZO films

As a further work proving again the concept of grain boundary effect in the NBIS condition, TEM analysis was conducted. Figure 3.7.1 shows cross-section TEM images of IZO films with In content of 52, 65 and 77 at.%, which corresponds to the transition region. The IZO film with 52 at.%In shows a polycrystalline structure. The IZO film with 65 at.%In is composed of amorphous and crystalline phases, so it can be called a partially crystallized film. Finally, the IZO film with 77 at.%In shows perfect amorphous structure, where well-arranged atom group cannot be seen at all, and broad ring is observed in the diffraction pattern image. From these TEM images, it was confirmed clearly that in transition region, In content increasing, portion of crystalline region comprising the IZO film is decreased, so grain boundaries are decreased. Therefore, the effect of nanocrystallization in transition region, which can induce increase in grain boundary area and V_{th} displacement under NBIS, can be excluded.

Figure 3.7.2 (a) shows SEM top images of 16 nm-thick $I_xZ_{1-x}O$ films. In the surface of the ZnO film, circle-shape grains were observed obviously, and average grain size was ~10 nm. As In content increased up to 65 at.%, the grain size was decreased gradually, and grain boundary became faint. In the IZO films with In > 77 at.%, which correspond to amorphous state, clear grain-like morphology was not

observed. Figure 3.7.2 (b) shows cross-section images of 130 nm-thick $I_xZ_{1-x}O$ films. Below 77 at.% In, all the samples had similar columnar structure, but the film with In content of 73 at.% had somewhat different morphology, which had two sections: i) ~27 nm-thick non-columnar layer near interface between IZO and SiO_2 , ii) ~100 nm-thick columnar layer. As In was incorporated more than 77 at.%, the columnar shape disappeared, and only smooth and uniform film morphology was observed.

In the respect of NBIS instability, the columnar structure is detrimental factor because the structure can facilitate defect migration such as oxygen vacancies. The boundaries between the columns can be regarded as huge grain boundary region, and the boundaries are parallel to the direction of V_o^{2+} migration under the negative gate voltage. In silicon industry, it was reported that diffusion depth of implanted ion was much deeper in poly-Si than in amorphous Si due to columnar structure in poly-Si, and impurity diffusion at high temperature mainly occurred to vertical direction while lateral diffusion was only about ~20 %.^{72 76} Therefore, the extinction of the columnar structure in amorphous IZO films would be one of major reason for improvement of NBIS instability in transition region.

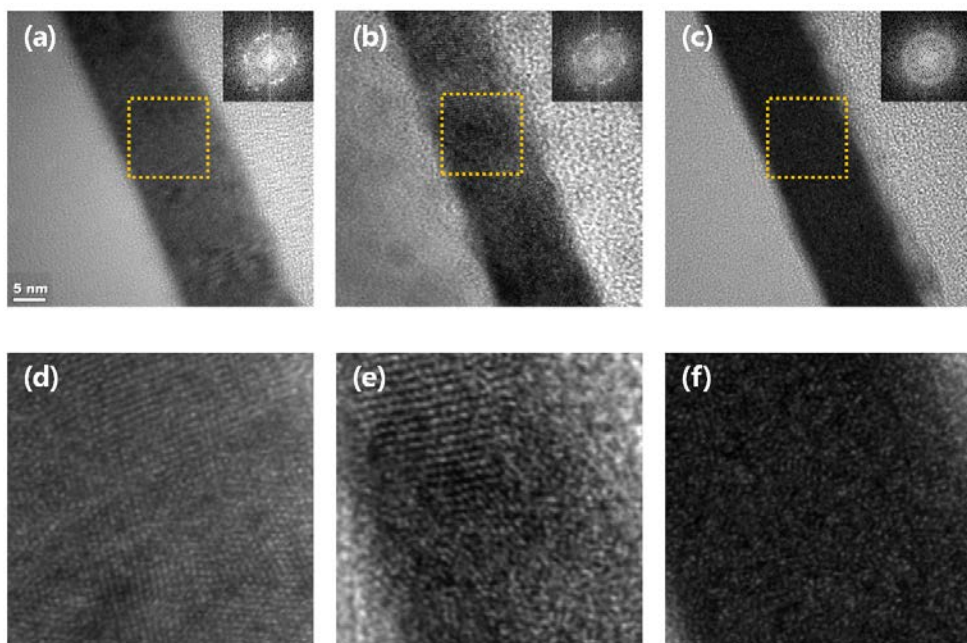


Fig. 3.7.1 Cross-section TEM images of IZO films of (a) 52, (b) 65, and (c) 77 at.%In, respectively. Inset shows diffraction pattern of the selected area, and (d), (e), (f) are magnified images of the selected area

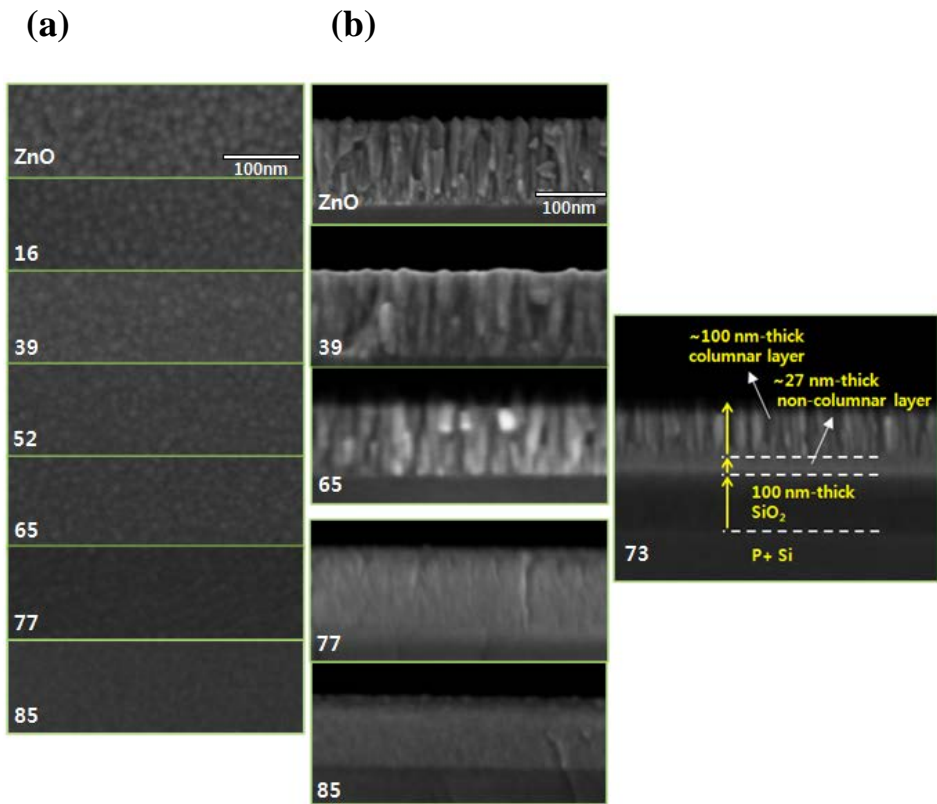


Fig. 3.7.2 SEM images of $I_xZ_{1-x}O$ films: (a) top view of 16 nm-thick films and (b) cross-section view of 130 nm-thick films. White numbers represent In content (at.%) of the films

3.8. Quantitative analysis for ΔV_{th}

In this section, the quantitative relationship between the ΔV_{th} under NBIS and the affecting factors (grain boundary and oxygen vacancy concentration) is confirmed. First, to quantify the grain boundary effect, average grain size of the ZnO and IZO films was calculated from grazing incidence XRD data (fig. 3.6.2) using the Scherrer's equation ($d = 0.9\lambda/B\cos\theta_B$) and the values are shown in fig. 3.8.1 (a) and table. 3.8.1. The grain size of 18.5 nm in the ZnO film was decreased gradually with increasing In content, and the grain size in $In_{0.65}ZnO_{0.35}O$ film was 10.6 nm. Using the relationship that grain boundary area is proportional to $1/d^2$, the change ratio of grain boundary area and ΔV_{th} were obtained, shown in fig. 3.8.1 (b). It is seen that there is a correlation between grain boundary area and V_{th} displacement in crystalline region. As the grain boundary area was increased by ~2.5 times, the ΔV_{th} was increased by almost four times. This result can be said to be appropriate, considering that increase in oxygen vacancy concentration can also amplify the V_{th} degradation. In transition region, the effect of the increase in oxygen vacancy concentration and calculated grain boundary area was negligible, because the extension of amorphous structure in the films much improved the NBIS instability. In the amorphous region (See fig. 3.4.2), where only oxygen vacancy concentration would affect the instability, the drastic increase in ΔV_{th} was observed.

Relatively small change of In content of 8 at.% induced severe degradation of ΔV_{th} characteristic from -3.65 to -7.94 V. Similar variation in defect concentration was observed in fig. 3.8.2 (a) and (b). The increase rate of oxygen vacancy concentration and In^+ is relatively steeper in high In composition films, which is consistent with the drastic increase in ΔV_{th} . Following the first-principle simulation results,^{77 78 44} the formation energy of oxygen vacancy near In atom is lower than near other metal atoms (Zn, Ga, ...) due to the relatively weak bond of In-O, so that an IZO film with high In content can easily form oxygen vacancies. In addition, while O atom surrounded many In atoms has a high possibility of being vacancy defect, its energy level could be shifted toward the shallow level direction (toward C.B.M).⁷⁹ In this In cation combinatorial study, when In content > ~77 at.%, it is expected that the remarkable V_O energy level shift occurred. Therefore, electron concentration could be increased drastically (See fig. 3.3.2 (a)) at In content above 77 at.% due to smaller ionization energy of V_O . In the respect of NBIS instability mechanism, the more portion of total V_O can be ionized to V_O^{2+} under same light irradiation (2.07 eV, 600 nm) by the V_O energy level shift toward C.B.M.

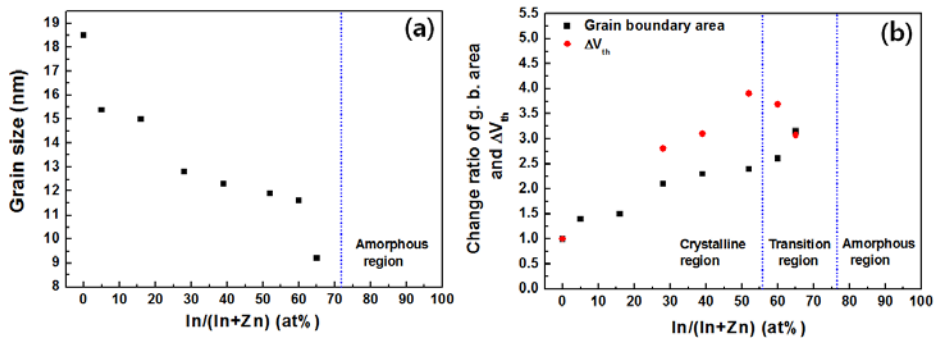


Fig. 3.8.1 (a) Average grain size by Scherrer's equation, (b) Change ratio of grain boundary area and ΔV_{th} under NBIS with increasing In content

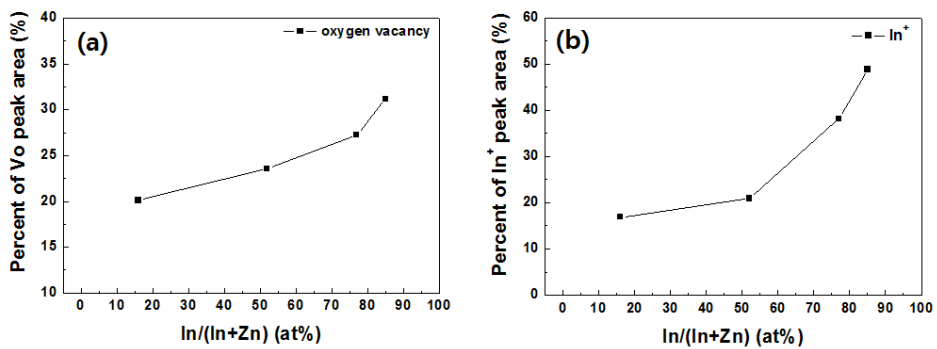


Fig. 3.8.2 Percent of (a) oxygen vacancy peak and (b) 1+ charged In peak area with increasing In content

Table 3.8.1 Values of grain size, ΔV_{th} and change ratio of grain boundary area and ΔV_{th} for various In content. (The devices with 5 and 16 at.%In did not show appropriate TFT operation)

In content (at.%)	G.b size, d (nm)	$(1/d^2)/$ $(1/d_{ZnO}^2)$	ΔV_{th} $/\Delta V_{th, ZnO}$	ΔV_{th} (V)
0	18.5	1	1.0	2.04
5	15.4	1.4	-	-
16	15	1.5	-	-
28	12.8	2.1	2.8	5.73
39	12.3	2.3	3.1	6.23
52	11.9	2.4	3.9	7.89
60	11.6	2.6	3.7	7.52
65	10.6	3.1	3.1	6.26

3.9. Summary

In summary, this study examined the effect of the In fraction on the device performance and photo-bias instability of the resulting IZO TFTs. The addition of In_2O_3 by co-sputtering on the ZnO film resulted in significant improvement in the transport properties, such as the SS factor and $I_{\text{on/off}}$ ratio. Therefore, the $\text{In}_{0.85}\text{Zn}_{0.15}\text{O}$ TFTs exhibited a high μ_{FE} , low SS and high $I_{\text{on/off}}$ of $41.0 \text{ cm}^2/\text{Vs}$, 0.20 V/decade and of 6.4×10^8 , respectively. On the other hand, the NBIS instability in the V_{th} shift was degraded with increasing In fraction when it was lower than ~ 60 at %, where the poly-crystalline structure was maintained. This was attributed to the increased formation of oxygen vacancies and electric field induced migration of ionized vacancies with increasing In fraction. On the other hand, the NBIS instability in the V_{th} shift was minimized near an In fraction of ~ 75 at%, which is related to a poly-crystalline to amorphous phase transition. Further increases in the In fraction deteriorated the reliability due to the increased vacancy concentration. This suggests that the migration of photo-excited V_O^{2+} defects also plays an important role in determining the overall V_{th} instability, and the absence of grain boundary defects is desirable for securing the photo-bias stability of the IZO TFTs.

Chapter 4. Dynamics of negative bias thermal stress-induced threshold voltage shifts in indium zinc oxide transistors: impact of the crystalline structure on the activation energy barrier

4.1. Introduction

Metal oxide thin film transistors (TFTs) have attracted considerable interest for applications in the next generation active matrix displays, such as liquid crystal displays, organic light-emitting diodes, transparent and flexible displays because of their high field-effect mobility ($\mu_{FE} > 10 \text{ cm}^2/\text{Vs}$), good electrical uniformity, low processing temperature, and good transparency to visible light.^{17 80 47} The gate bias thermal stress (BTS)-induced instabilities of metal oxide TFTs is still one of major concerns for their practical applications in backplane electronics.⁸¹ The origin of threshold voltage (V_{th}) instability can be classified as either extrinsic or intrinsic. The injection of charge carriers to the gate dielectric^{82 83 84} and the dynamic interactions of a back channel surface with oxygen and moisture^{85 86} under gate bias stress conditions are rather extrinsic, which can be resolved substantially using a high quality gate insulator and passivation films, such as SiO_2 or Al_2O_3 .^{87 88 89} However, oxygen vacancy (V_O)-related instability is intrinsic because it originates

from the non-stoichiometry.^{90 91 92} BTS or light-enhanced BTS instability has been understood based on the concept of either the photo-ionization^{93 94 95} of V_O to V_O^{2+} or the migration^{96 97} of V_O^{2+} . The positive BTS (PBTS)-induced instability of metal oxide TFTs have been analyzed using the stretched-exponential model, where the comparable activation energies for the PBTS and recovery are extracted.⁹⁸ This suggests that rather than charge trapping at the channel/insulator, a defect creation or migration mechanism at the channel layer is responsible for the PBTS-induced V_{th} displacement. This type of framework is very useful for identifying the specific point defects as an origin of the BTS-induced V_{th} instability.⁹⁹ In particular, the extracted activation energies can be interpreted as either a defect formation energy or a migration energy barrier, which would be helpful for clarifying the metastability of such defects.^{68 100} Furthermore, a comprehensive understanding can be deepened further by comparing the experimental result with the theoretical calculations. Nevertheless, this type of approach for negative BTS (NBTS)-induced V_{th} instability has not been attempted for metal oxide TFTs.

Recently, the c-axis aligned crystal (CAAC) IGZO TFTs were reported to exhibit extraordinary stability against an external BTS and light.¹⁰¹ On the other hand, the microscopic origin for such improvement in the CAAC IGZO device compared to the conventional amorphous IGZO TFT was unclear. Therefore, the role of the grain boundary in the crystalline structure needs to be clarified. A

previous study reported that the In fraction-dependent structural properties of the IZO films and the light-enhanced NBTS instability of the resulting IZO TFTs were strongly correlated.⁹⁷

Interestingly, as the In fraction in IZO films increased from 52 to 77 at.%, the IZO film exhibited a poly-crystalline to amorphous phase transition: the V_{th} shift (ΔV_{th}) of the $In_{0.77}Zn_{0.23}O$ TFTs by photo-bias stress were suppressed to -3.0V compared to that (-7.9V) of the $In_{0.52}Zn_{0.48}O$ TFTs, even though they had a higher indium content. The specific stress conditions are: $V_{GS} = V_{th} - 15$ V, $V_{DS} = 10$ V, light intensity = 1.5 mW/cm², wavelength of the light = 600 nm, and the duration time = 2,000 s. This unexpected result for $In_{0.77}Zn_{0.23}O$ TFTs was attributed to the absence of grain boundary defects. However, very little is known about the kinetic behavior of the NBTS-induced V_{th} instability for metal oxide TFTs with different crystalline quality.

This study examined the NBTS-induced V_{th} instability for indium zinc oxide (IZO) TFTs based on the stretched exponential model, where three devices including a poly-crystalline and amorphous IZO channel were evaluated. The in-depth recovery behaviors for the three devices were also examined to clearly understand the relevant microscopic meta-stability. The activation energy of the temperature dependent V_{th} shift under NBTS conditions was reduced by approximately 0.6 eV for the poly-crystalline IZO device compared to that of the

amorphous IZO device. Nevertheless, the activation energy for the recovery was independent of the crystalline structure. A plausible physical mechanism was proposed to explain these results.

4.2. Experimental

The inverted staggered IZO TFTs were fabricated on highly-doped p-type Si wafers, which were used as the gate electrode. As a gate insulator, a 100-nm-thick SiO₂ layer was grown by wet thermal oxidation. Subsequently, the 16-nm-thick IZO channel layers with 52, 65 and 77 at.% In were prepared by radio-frequency (rf) magnetron co-sputtering using a ZnO target and In₂O₃-ZnO (90:10 wt.%) target. The In content of the devices was confirmed by X-ray fluorescence (XRF) spectroscopy. The channel area was defined using a shadow mask during IZO film deposition, and 100-nm-thick ITO source/drain (S/D) electrodes were deposited at room temperature using the same sputtering system. The channel width (W) and length (L) of the fabricated TFTs were 1000 μm and 300 μm, respectively. Post-deposition-annealing (PDA) of the devices was performed in air ambient at 350°C for 1 hour in a vertical-type tube furnace. A high quality Al₂O₃ passivation layer (15nm) was deposited by thermal atomic layer deposition to exclude the adverse ambient effect during bias thermal stress conditions.⁸⁶ In the ALD deposition process, ozone (O₃) was used as a oxidizing agent, which would fairly improve the quality of passivation layer and channel/passivation layer interface. The TFT structure is shown in fig. 4.2.1. The electrical measurements of the devices were carried out using an HP 4155A semiconductor parameter analyzer. In this

experiment, the temperature dependent measurements were performed on the same device. After each measurement at a given temperature, the devices were subjected to the thermal annealing at 180 °C for 30 min. The devices were completely recovered to the pristine state by the thermal annealing.

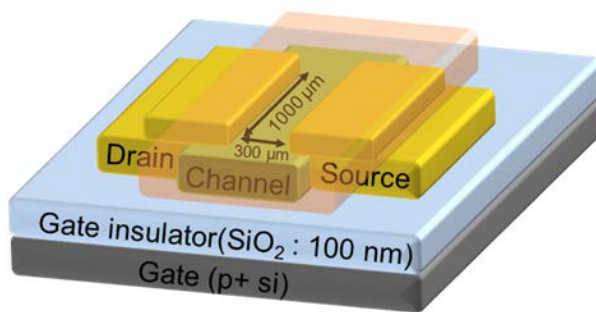


Fig. 4.2.1 Schematic of structure of the passivated IZO TFT

4.3 Electrical properties of IZO TFTs

Figure 4.3.1 shows the representative transfer characteristics of $\text{In}_{0.52}\text{Zn}_{0.48}\text{O}$, $\text{In}_{0.65}\text{Zn}_{0.35}\text{O}$ and $\text{In}_{0.77}\text{Zn}_{0.23}\text{O}$ TFTs. The electrical characteristics of the three devices are summarized in Table. 4.3.1. The $\text{In}_{0.52}\text{Zn}_{0.48}\text{O}$ TFTs exhibited a field-effect mobility (μ_{FE}), subthreshold gate swing (SS), threshold voltage (V_{th}), and $I_{\text{on/off}}$ ratio of $2.7 \text{ cm}^2/\text{Vs}$, 0.31 V/decade , -0.6 V , and 5×10^7 , respectively. The marginal μ_{FE} was attributed to the Schottky energy barrier at the grain boundary defects.¹⁰² As the In content increased from 52 to 65 at%, the μ_{FE} value of the $\text{In}_{0.65}\text{Zn}_{0.35}\text{O}$ TFT increased to $17.6 \text{ cm}^2/\text{Vs}$. In contrast, the $\text{In}_{0.77}\text{Zn}_{0.23}\text{O}$ TFTs showed significant improvement in the device performance: the μ_{FE} and SS values were improved to $33.5 \text{ cm}^2/\text{Vs}$ and 0.22 V/decade without any degradation of V_{th} (-0.4V) and $I_{\text{on/off}}$ ratio (3×10^8), which was attributed to the higher In fraction and the absence of grain boundary defects.

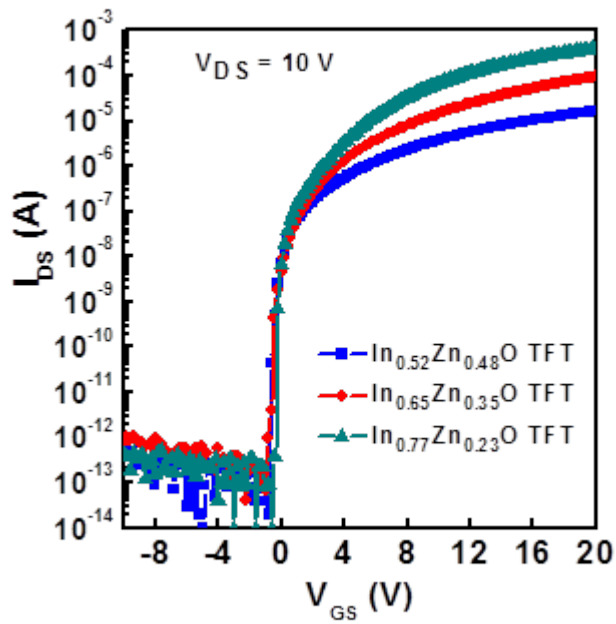


Fig. 4.3.1. Representative transfer characteristics for the three devices.

Table. 4.3.1 Electrical characteristics of the IZO TFTs with 52, 65 and 77 at. %In.

Samples	μ_{FE} [$\text{cm}^2\text{V}^{-1}\text{s}^{-1}$]	SS [Vdecade^{-1}]	V_{th} [V]	I_{on}/I_{off}
$\text{In}_{0.52}\text{Zn}_{0.48}\text{O}$	2.7	0.31	-0.6	5.0×10^7
$\text{In}_{0.65}\text{Zn}_{0.35}\text{O}$	17.6	0.34	-0.6	1.6×10^8
$\text{In}_{0.77}\text{Zn}_{0.23}\text{O}$	33.5	0.22	-0.4	3.0×10^8

4.4 Activation energy for the negative V_{th} displacement of IZO TFTs

The NBTS-induced instability for the three devices was examined. The devices were stressed under the following conditions: $V_{GS} = V_{th0} - 30$ V and $V_{DS} = 0$ V, where V_{th0} is the threshold voltage of the pristine device. Figure 2 shows the variations of the V_{th} values as a function of the NBTS time. No variations in the V_{th} value for the devices were observed when the temperature was less than 80°C (data not shown). This can be attributed to the prevention of dynamic interaction of the back channel surface with ambient gas such as O_2 or H_2O due to the high quality Al_2O_3 encapsulation. Therefore, the minimum temperature of the NBTS measurement was set to 80°C, and the evaluated temperature ranges (80, 105, 130 and 155°C) were rather high compared to that of other reports.^{98 99} The data was fitted with a stretched exponential of the form :

$$|\Delta V_{th}(t)| = V_0 \left\{ 1 - \exp \left[- \left(\frac{t}{\tau} \right)^\beta \right] \right\} \quad (1)$$

where τ is the relaxation time, β is the dispersion parameter of the barrier energy height, and V_0 is $V_{GS} - V_{th0}$ (V_{GS} is the applied gate bias stress). The fit of the stretched exponential to the data at 80 °C gave a relaxation time τ of 1.3×10^8 s and 4.0×10^9 s for the $In_{0.52}Zn_{0.48}O$ TFTs and $In_{0.65}Zn_{0.35}O$ TFTs, respectively. In contrast, the relaxation time τ was increased greatly to 1.5×10^{12} for the

$\text{In}_{0.77}\text{Zn}_{0.23}\text{O}$ TFTs, indicating that they have the superior resistance against NBTS.

The reason for such improvement is discussed below. The relaxation time (τ) is activated thermally according to the following equation :

$$\tau = \nu^{-1} \exp\left(\frac{E_{\tau}}{k_B T}\right) \quad (2)$$

Where E_{τ} is the activation energy for the process, ν is the frequency pre-factor for emission over the barrier, T is the absolute temperature, and k_B is the Boltzmann constant.

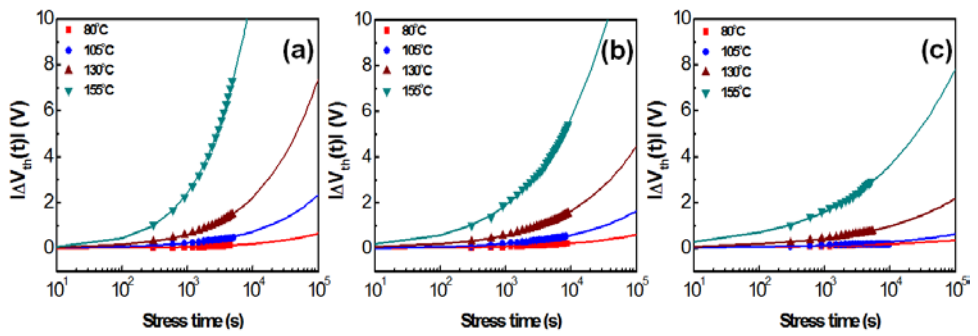


Fig. 4.4.1 Time dependence of $|\Delta V_{th}|$ under NBTS conditions for the (a) $\text{In}_{0.52}\text{Zn}_{0.48}\text{O}$, (b) $\text{In}_{0.65}\text{Zn}_{0.35}\text{O}$ and (c) $\text{In}_{0.77}\text{Zn}_{0.23}\text{O}$ TFTs at different temperatures. The solid lines are fits with a stretched exponential equation.

Figure 4.4.2 (a), (b) and (c) show the variations of $\ln r$ as a function of the reciprocal temperature for the three devices. The data was well fitted using Eq. (2), suggesting that the devices have a temperature dependence of τ and the NBTS-induced V_{th} shift is a thermally-activated process. The E_τ values for the three devices were calculated from the slope of the straight lines. The E_τ values for the $\text{In}_{0.52}\text{Zn}_{0.48}\text{O}$, $\text{In}_{0.65}\text{Zn}_{0.35}\text{O}$ and $\text{In}_{0.77}\text{Zn}_{0.23}\text{O}$ TFTs were 1.40, 1.72 and 2.04 eV, respectively. Tentatively, the extracted activation energy would correspond to the summation of the energy barriers for each process responsible for NBTS-induced V_{th} shift. First, the ionization of oxygen vacancies (V_O) can be suspected. Some portion of neutral V_O near the channel/insulator interface can be excited to the double charged V_O^{2+} state due to lowering of the Fermi level (E_F), leading to the two delocalized electrons to the conduction band¹⁰³. This process has been proposed as an origin for the photon-enhanced NBTS-induced V_{th} instability.⁸¹ Because the V_O^{2+} is a meta-stable state, the transition from the ground V_O state to excited V_O^{2+} requires a thermal energy barrier. The other process would be the migration of ionized V_O^{2+} defects by the applied NBTS.^{96 97} The migration energy barrier of V_O^{2+} was reported to be much lower than that of V_O in the electron calculation result of crystalline ZnO.⁶⁸ Given that both processes prevail simultaneously under NBTS conditions, it is reasonable that the experimentally observed energy barrier (E_τ) is the sum of the thermal ionization barrier of V_O to

V_O^{2+} and the migration barrier energy of V_O^{2+} . The E_τ difference between the devices can be attributed to different migration paths. The IZO film with 52 at.% In was poly-crystalline, consisting of many grains so that this film contains a large grain boundary area. When the V_O^{2+} drifted toward the channel/gate insulator interface due to the applied NBTS, V_O^{2+} is likely to migrate through the grain boundary region rather than through the bulk lattice. (see Fig. 4.4.3). The diffusivity of an atom or defect at the grain boundary is 3~4 orders of magnitude higher due to the lower energy barrier than that of the bulk lattice.¹⁰⁴ This explains the lower E_τ (1.40 eV) for the $In_{0.52}Zn_{0.48}O$ TFTs. The existence of crystallographic face-dependent migration barrier energies can be confirmed by the higher β values (0.53 ~ 0.75) for this device, as shown in Fig. 4.4.2 (a). The IZO film with 65 at.% In exhibited the intermediate state between a poly-crystalline and amorphous state. The increased activation energy of 1.72 eV compared to that (1.4eV) of $In_{0.52}Zn_{0.48}O$ device can be attributed to the enhanced volume portion of grain boundary-free amorphous phase. When the In content increased up to ~77 at.%, the IZO film showed a complete amorphous structure. In this amorphous film, the migration path of V_O^{2+} through grain boundary defects is prevented and the diffusion of V_O^{2+} via the homogeneous amorphous IZO matrix requires a higher migration energy barrier and narrow distribution of E_τ (β : 0.29 ~ 0.42). Therefore, the E_τ difference of 0.64 eV between $In_{0.52}Zn_{0.48}O$ and $In_{0.77}Zn_{0.23}O$ TFTs originates

from the different structure of IZO films, corresponding to the difference in migration barrier energy between the poly-crystalline and amorphous structure of IZO. It should be noted that the In content dependent bandgap variation of IZO films also affects the activation energy because the extended state conduction and band tail conduction in amorphous or nano-crystalline phase materials is strongly dependent on their optical bandgap. Figure 4.4.4 and table 4.4.1 show the optical band gap of IZO films with various In contents by using Tau plot from UV-visible transmittance data. As the In content increased, the band gap decreased from 3.31 up to 3.11 eV. However, the band gap difference was negligible in the range from 52 to 77 at.% In which was studied in this section. Therefore, it is speculated that the variation in the activation energy was mainly affected by difference of crystal structure and oxygen vacancy migration rather than change of band gap or electronic structure.

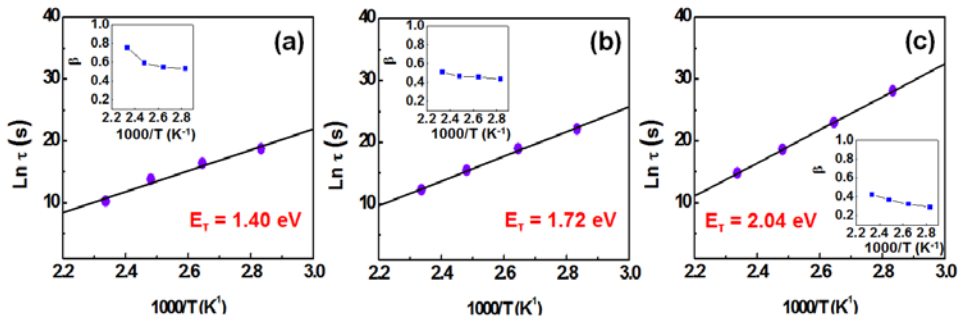


Fig. 4.4.2. Relaxation time τ as a function of the reciprocal temperature for the (a) $\text{In}_{0.52}\text{Zn}_{0.48}\text{O}$ (b) $\text{In}_{0.65}\text{Zn}_{0.35}\text{O}$ and (c) $\text{In}_{0.77}\text{Zn}_{0.23}\text{O}$ TFTs. The activation energies were obtained from the slope of the straight lines. The inset shows the corresponding dispersion parameter β as a function of the reciprocal temperature.

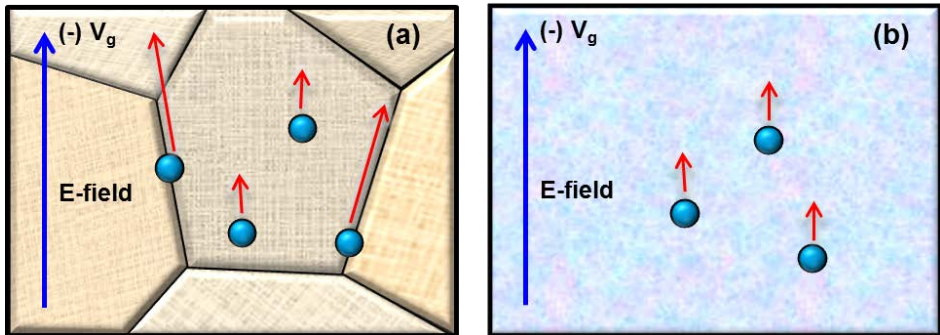


Fig. 4.4.3 Schematic diagram showing the migration of V_O^{2+} defects for (a) poly-crystalline and (b) amorphous IZO materials under the NBTS.

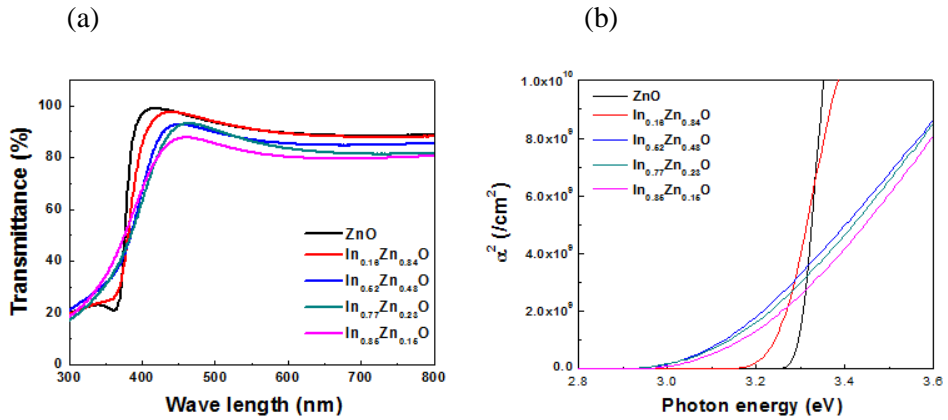


Fig. 4.4.4 (a) Transmittance of IZO films with different In contents. (b) Tau plot from the transmittance data for obtaining the optical bandgap.

Table. 4.4.1 Optical bandgap of the IZO films.

In content (at.%)	0	16	52	77	85
Eg.opt (eV)	3.31	3.25	3.11	3.13	3.18

4.5 Activation energy for the recovery process

To examine the recovery process, the devices were stressed by NBTS at 175°C for 2 h. After the stress, the V_{th} displacement were -10, -8 and -4 V for the devices containing 52, 65 and 77 at.% In, respectively. The chuck temperature was readjusted to the different temperature of 70, 90, 110, and 130°C. After the stabilization of chuck temperature (~5 min), the transfer curves for all devices were measured as a function of time. The V_{th} for the initial transfer curve ($t=0$) was extracted and defined as $V_{th0}(t=0)$. Because the applied gate bias stress is zero during recovery, the V_0 value is $-V_{th0}$. Therefore, the $\Delta V_{th}(t)$ was defined as the $V_{th}(t) - V_{th0}(t=0)$ in the relaxation process. Figure 4.5.1 shows the recovery time-dependent V_{th} variations and the relaxation time as a function of the reciprocal temperature. The E_r obtained from the recovery were 0.73, 0.77 and 0.75 eV for the devices with 52, 65 and 77 at.% In, respectively. Because the E_r values for the recovery are comparable, it can be inferred that the crystalline structure of the IZO films has no important role in the recovery process. In the recovery process, a reverse neutralization reaction of V_O^{2+} [$V_O^{2+} + 2e^- \rightarrow V_O$] would be dominant. During the neutralization process, the electrons induced by the V_O^{2+} near the channel/insulator interface would be partially consumed. This recovery picture would be similar to that for the IGZO channel. An activation energy of ~0.9 eV¹⁰⁵

¹⁰⁶ was estimated from the recovery of persistent photo-conductivity (PPC), where the meta-stable V_O was proposed as an origin. It is noted that the β values of polycrystalline $In_{0.52}Zn_{0.48}O$ device for recovery process is higher than those of amorphous $In_{0.77}Zn_{0.23}O$ devices. The activation energy for the neutralization from V_O^{2+} to V_O is likely to be different between the bulk lattice region and the grain boundary interfaces. Because the configuration and relaxation of the residing V_O^{2+} defects on the grain boundary would be dependent on the crystallographic faces, this variety in the polycrystalline phase compared to amorphous phase may result in the higher β value even though the average E_r value is comparable to each other.

It was confirmed that the three devices had comparable activation energies for recovery, but how it could be possible in different crystalline structure and Zn/In composition condition? The crystalline structure of the device with 52 and 77 at.%In was quite different as an entirely polycrystallized phase and perfect amorphous phase, respectively. When recovery process occurs in different crystal or crystalline structures, the energy barrier of inward/outward relaxation of oxygen vacancies can be affected. In first principle calculation of IGZO, somewhat different recovery barrier was reported.⁴⁴ However, the electronic properties (defect level, formation energy, charge transition level, *etc.*) of oxygen vacancies are also determined by local bonding nature in short range order. In ZnO and In_2O_3 crystal structure, Zn and In has tetrahedral and octahedral coordination, respectively.

Because of the property that Zn and In preserve their coordination states (ZnO_4 , and InO_6), IZO has a layered structure where InO_2 octahedral layers are interleaved between wurzite ZnO or In/Z-O layers. First principle calculation^{107 108} for IZO reported the coordination number (CN) of metal cations in crystalline IZO is comparable to amorphous IZO due to similar local bonding states, and CN of oxygen anion was also constant as ~ 4 with varying In/Zn composition. It is expected that the variation of In content from 52 to 77 at.% did not induce change in local bonding structure, so neutralization barriers of V_O^{2+} would be comparable. Increase in neighboring In atoms near oxygen can change the electronic properties of oxygen vacancies, but such an effect is considered to be significant in the case of higher In content region (> 77 at.%), judging from the result in chapter 3.

Figure 4.5.2 shows a plausible energy diagram to account for the experimental results. For a clear comparison between poly-crystalline and amorphous structures, only devices with 52 and 77 at.% In were described. The energy diagram represents the activation energy of the NBTS-induced V_th shift and recovery process. The V_O^{2+} is located at a higher meta-stable state than V_O under the equilibrium conditions. The transition from V_O to V_O^{2+} is responsible for the PPC phenomena.^{81 68} The different activation energy for both devices is related to the different migration path of V_O^{2+} . In the recovery process, however, both devices exhibit the same activation energies (~ 0.75 eV) because the recovery of V_th might result from the identical

neutralization of the V_O^{2+} . That is, the neutralization energy of V_O^{2+} would be independent of the In fraction and crystalline quality. The thermal neutralization of V_O^{2+} to V_O makes the value of V_{th} to move toward the pristine position. An excess V_O concentration presumably exists near the channel/insulator interface. This concentration gradient of $[V_O]$ will promote the diffusion of V_O toward the bulk region until an equilibrium state is reached, which corresponds to full recovery. Here, the diffusion of neutral V_O does not involve the V_{th} displacement. Therefore, a comparable recovery barrier energy can be expected.

If the excess V_O remains near the channel/insulator interface just after the V_{th} recovery, the repetition of NBTS measurement could induce the larger V_{th} displacement. To confirm the possibility, NBTS test was carried out three times for the device with In content of 65 at.%, where the V_{th} of device was recovered to pristine position after an each measurement. Temperature of first recovery was 170 °C, and the time to recover pristine V_{th} value was ~3 h. In second recovery before third NBTS test, the temperature was 120 °C, and the time was 5 days. Figure 4.5.3 shows the result of the repetition test, where the V_{th} shift values were almost same, and evidence of the excess V_O near the interface was not found. In first principle calculation of a-IGZO, V_O was reported to diffuse even at RT.⁶⁰ In twice the recovery, a quite high temperature or quite long time was required for recovering the pristine V_{th} . Therefore, it is expected that the excess V_O would diffuse away

simultaneously from the interface during recovery of V_{th} . The result of fig 4.5.3 can be explained by a different manner. When an NBTS test caused the negative ΔV_{th} , the number of trapped V_O^{2+} near channel/insulator interface were $1.08 \times 10^{12} / \text{cm}^2$. The value was calculated approximately using $\Delta Q = C_i \Delta V_{th}$ relation. (Capacitance of channel layer was ignored due to its much higher value than that of SiO_2 .) ΔQ is induced trapped charge, and C_i is capacitance of insulator. The value can be converted to $3.4 \times 10^{17} / \text{cm}^3$ by film thickness correction. Considering the V_O concentration of $\sim 10^{20} / \text{cm}^3$ in bulk,²⁵ the trapped quantity is very small in number. Therefore, after V_{th} recovery, the excess V_O near interface can be negligible even though the excess V_O did not diffuse toward bulk direction. Under following NBTS condition, at first, some portion of V_O are excited to V_O^{2+} in entire region of channel layer by thermal energy, here, most of the V_O^{2+} are generated from the bulk concentration ($\sim 10^{20} / \text{cm}^3$). Subsequently, the V_O^{2+} are attracted gradually toward interface by negative gate bias and accumulated near interface. In the overall process, the excess V_O near interface cannot have a significant effect on the V_{th} shift process because of its relatively small quantity compared to the bulk concentration.

Finally, there is one more thing to be discussed, why the reverse migration of V_O^{2+} did not occur? Two reasons would be responsible to the experimental result. First, the migration barrier (~ 1.4 eV) of V_O^{2+} is known to be much higher than neutralization barrier (0.2~0.9 eV) of that, so V_O^{2+} would capture two electrons

rather than migrate toward channel bulk in the recovery process. However, the possibility of simultaneous occurrence of the migration and neutralization of V_O^{2+} still remains. Second, the effective stress to recover pristine V_{th} would be weak in the recovery measurement. In NBTS measurement, the gate stress (or effective stress) was ~ -30 V, but in recovery, the effective stress are $-4 \sim -10$ V, because gate voltage was set to 0 V. The much lower effective stress in recovery would not induce reverse migration of V_O^{2+} , so the migration barrier was not included to the activation energy in recovery process. If the positive gate stress is applied in recovery process, the reverse migration would be expected. However, under the PBS condition, trapping or migration of electrons and negatively charged defects would also take place, so there is a limit to estimate only the reverse migration in recovery process.

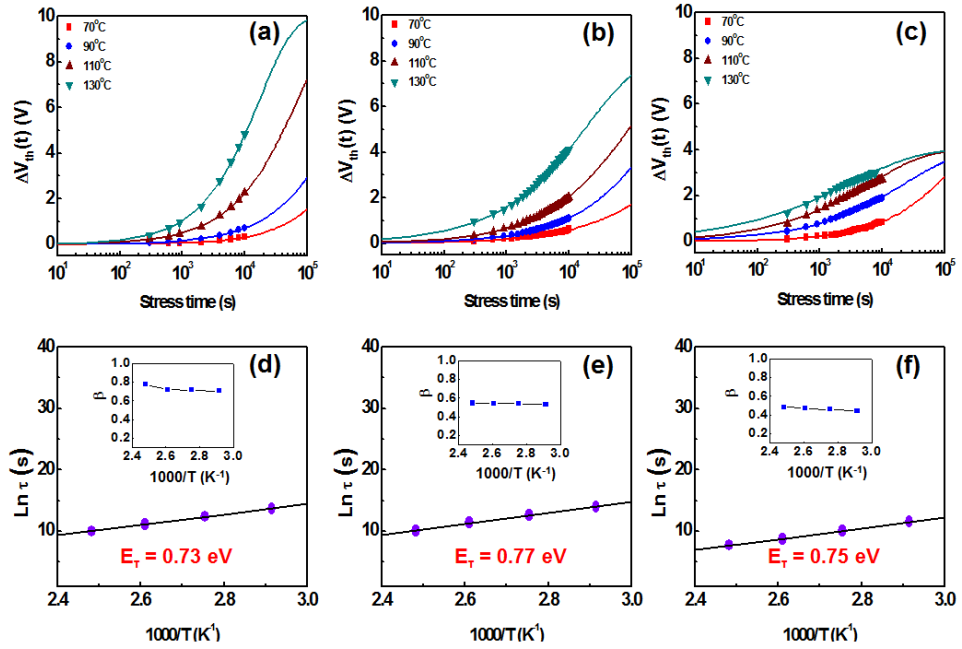


Fig. 4.5.1 Recovery time dependence of ΔV_{th} for the (a) $\text{In}_{0.52}\text{Zn}_{0.48}\text{O}$, (b) $\text{In}_{0.65}\text{Zn}_{0.35}\text{O}$ and (c) $\text{In}_{0.77}\text{Zn}_{0.23}\text{O}$ TFTs at different temperatures. The corresponding relaxation time variations as a function of the reciprocal temperature for the (d) $\text{In}_{0.52}\text{Zn}_{0.48}\text{O}$, (e) $\text{In}_{0.65}\text{Zn}_{0.35}\text{O}$ and (f) $\text{In}_{0.77}\text{Zn}_{0.23}\text{O}$ TFTs.

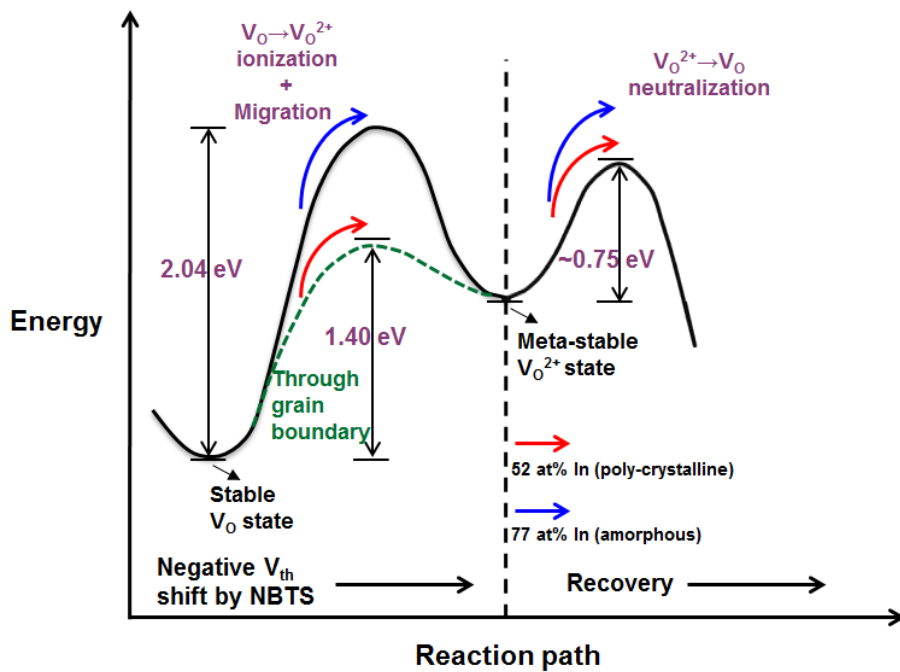


Fig. 4.5.2 Proposed energy diagram model showing the activation energy of the NBTS-induced V_{th} shift and their recovery process.

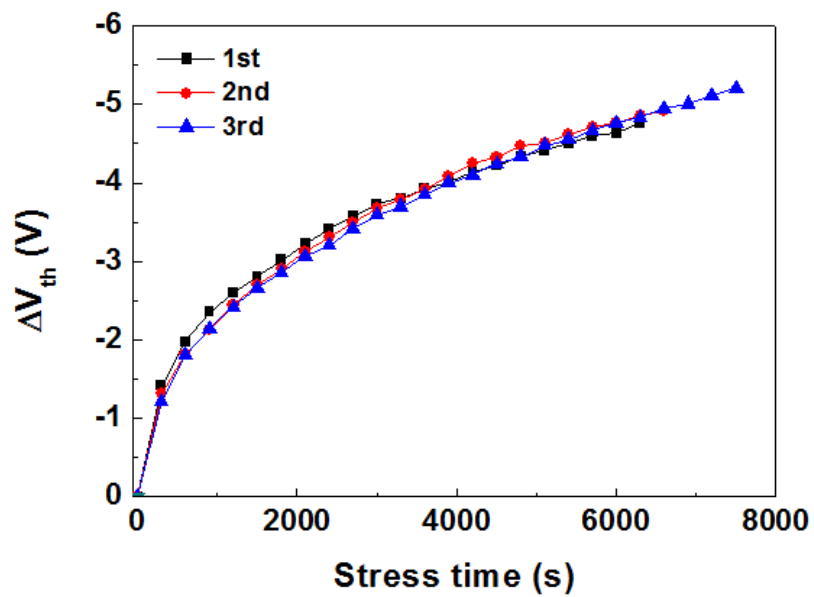


Fig. 4.5.3 Comparison of V_{th} displacement when NBTS and recovery was repeated.

The NBTS condition was $V_g = -30$ V, 170°C and ~ 2 h.

4.6 Summary

In summary, the NBTS-induced V_{th} instability of IZO TFTs with different crystalline structures was examined based on the stretched exponential formalism. All the obtained activation energy values are summarized in fig. 4.6.1. The calculated E_t value of the $In_{0.52}Zn_{0.48}O$ TFTs was 1.40 eV, whereas the $In_{0.65}Zn_{0.35}O$ and $In_{0.77}Zn_{0.23}O$ TFTs exhibited larger E_t values of 1.72 and 2.04 eV, respectively. This result indicates the transition from a poly-crystalline to amorphous structure induces the increase in migration energy barrier. Moreover, the E_t difference of 0.64 eV between two devices with 52 and 77 at.% In was attributed to the different migration paths of the V_O^{2+} defects, suggesting that the presence of grain boundary defects deteriorates the BTS-induced V_{th} instability of metal oxide TFTs. On the other hand, the energy barrier (~ 0.75 eV) for the recovery process was independent of the crystalline structure. This recovery behavior was attributed to a neutralization process ($V_O^{2+} + 2e^- \rightarrow V_O$).

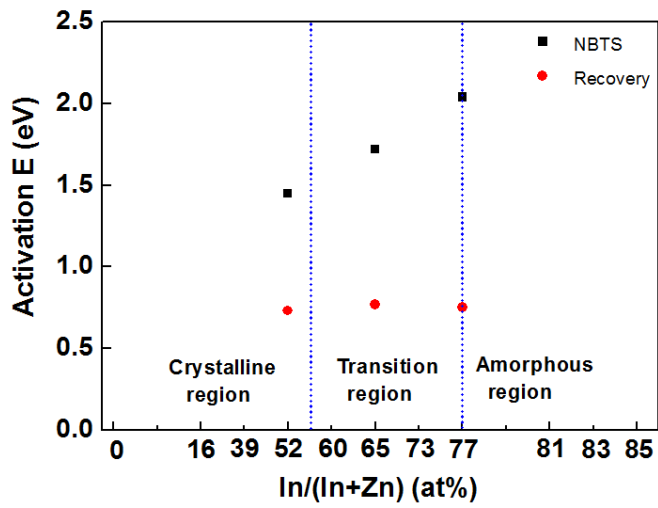


Fig. 4.6.1 Activation energy values of the three IZO TFTs for NBTS and recovery measurement.

5. Conclusions

The V_{th} instability of IZO TFTs under NBIS was investigated, and the effect of crystal structure of the channel layer on the instability was analyzed using stretched-exponential fitting method.

By co-deposition sputtering method, IZO TFTs with various In contents (0~85 at.%) were fabricated. Then, NBIS tests were carried out for all the IZO TFTs, so as to investigate the effect of atomic composition on the device performance and instability. The field-effect mobility and sub-threshold swing were much improved with increasing In fraction; $41.0 \text{ cm}^2/\text{Vs}$ and 0.2 V/decade , respectively, at 85 at.% In, compared to $1.1 \text{ cm}^2/\text{Vs}$ and 2.4V/decade of ZnO TFTs. On the other hand, the NBIS instability in the V_{th} shift was degraded with increasing In fraction when it was lower than 60 at.%, where the poly-crystalline structure was maintained. It was attributed to the increased formation of oxygen vacancies and electric field induced migration of ionized vacancies with increasing In fraction. In particular, columnar-type grain boundaries effectively facilitated the V_o^{2+} migration and degraded the NBIS instability. On the other hand, the NBIS instability in the V_{th} shift was minimized near an In fraction of 75 at.%, which is related to a poly-crystalline to amorphous phase transition. It suggests that the migration of photo-excited V_o^{2+} defects also plays an important role in determining the overall V_{th} instability, and

the absence of grain boundary defects and columnar structure is desirable for securing the photo-bias stability of the IZO TFTs. Further increases in the In fraction deteriorated the reliability due to the increased vacancy concentration and increase in shallow V_O , which induced the rapid increase in electron concentration as well. From this study, it can be confirmed that the effect of In atom and channel crystalline structure on the device instability, and the two factor are competing and determine the V_{th} displacement of the IZO TFTs. Moreover, the migration process of oxygen vacancy was considered also important as its concentration, which enabled to make clearer picture in oxygen vacancy model.

In study of chapter.4, the relationship between V_{th} instability and channel crystal structure was investigated quantitatively by extracting activation energy barrier. A poly-crystalline IZO device had a 0.64 eV lower activation barrier energy than an amorphous IZO device under NBTS conditions. It was attributed to the difference in the migration energy barrier between poly-crystalline and amorphous IZO films. For the recovery process, however, the activation energy barriers (~ 0.75 eV) were independent of the crystal structure. The recovery behavior was attributed to a neutralization process ($V_O^{2+} + 2e^- \rightarrow V_O$), and reverse migration of V_O^{2+} could be excluded. It is expected that local bonding nature in short range order was not changed. The result of the repetition of NBTS and recovery test indicated the effect of neutral V_O remained at channel/insulator interface on next time stress

measurement can be excluded.

These experimental results would be helpful for establishing the optimal fabrication condition of other ternary oxide material. In other ternary oxide system, the effect of channel crystallinity on the device performance and reliability is expected to be significant, and an appropriate cation composition for reducing oxygen vacancy quantity would be also important. Moreover, using a fitting method the migration barrier difference between poly-crystalline and amorphous was confirmed quantitatively, for the first time. From the temperature dependence of V_{th} displacement under negative gate bias, microscopic process of oxygen vacancy and recovery was established. This approach using stretched exponential fitting to identify certain defect behavior is expected to be useful to investigate the device instability and microscopic mechanism.

Bibliography

- ¹ H. Q. Chiang, Oregon state university, PhD thesis (2007).
- ² WE Spear and PG Le Comber, Solid state communications **17** (9), 1193 (1975).
- ³ Hiroyuki Uchida, Kazushige Takechi, Shinichi Nishida, and Setsuo Kaneko, Japanese journal of applied physics **30** (12S), 3691 (1991).
- ⁴ H Kiyama Kuriyama, S Noguchi, S Kuwahara, T Ishida, S Nohda, T Sano, and H Tsu K Iwata, 1991 (unpublished).
- ⁵ Tadatsugu Minami, Semiconductor Science and Technology **20** (4), S35 (2005).
- ⁶ Radhouane Bel Hadj Tahar, Takayuki Ban, Yutaka Ohya, and Yasutaka Takahashi, Journal of Applied Physics **83** (5), 2631 (1998).
- ⁷ Hans Hartnagel, AL Dawar, AK Jain, and C Jagadish, *Semiconducting transparent thin films*. (Institute of Physics Pub. Bristol, UK, Philadelphia, PA, 1995).
- ⁸ L Zhang, J Li, XW Zhang, XY Jiang, and ZL Zhang, Applied Physics Letters **95** (7), 072112 (2009).
- ⁹ John CC Fan and John B Goodenough, Journal of Applied Physics **48** (8), 3524 (1977).

- ¹⁰ G Lavareda, C Nunes de Carvalho, E Fortunato, AR Ramos, E Alves, O Conde, and A Amaral, *Journal of non-crystalline solids* **352** (23), 2311 (2006).
- ¹¹ Yuriy Vygranenko, Kai Wang, and Arokia Nathan, *Applied Physics Letters* **91** (26), 263508 (2007).
- ¹² Shiau-Shin Cheng, Chuan-Yi Yang, Chun-Wei Ou, You-Che Chuang, M Chyi Wu, and Chih-Wei Chu, *Journal of Physics D: Applied Physics* **41** (9), 092006 (2008).
- ¹³ N Itagaki, T Iwasaki, H Kumomi, T Den, K Nomura, TOSHIO Kamiya, and H Hosono, *physica status solidi (a)* **205** (8), 1915 (2008).
- ¹⁴ Matthew P Taylor, Dennis W Readey, Maikel FAM van Hest, Charles W Teplin, Jeff L Alleman, Matthew S Dabney, Lynn M Gedvilas, Brian M Keyes, Bobby To, and John D Perkins, *Advanced Functional Materials* **18** (20), 3169 (2008).
- ¹⁵ R Martins, P Barquinha, A Pimentel, L Pereira, E Fortunato, D Kang, I Song, C Kim, J Park, and Y Park, *Thin Solid Films* **516** (7), 1322 (2008).
- ¹⁶ R Martins, P Barquinha, A Pimentel, L Pereira, and E Fortunato, *physica status solidi (a)* **202** (9), R95 (2005).
- ¹⁷ Kenji Nomura, Hiromichi Ohta, Akihiro Takagi, Toshio Kamiya, Masahiro Hirano, and Hideo Hosono, *Nature* **432** (7016), 488 (2004).

- ¹⁸ Kenji Nomura, Hiromichi Ohta, Kazushige Ueda, Toshio Kamiya, Masahiro Hirano, and Hideo Hosono, *Science* **300** (5623), 1269 (2003).
- ¹⁹ Toshio Kamiya, Yujiro Takeda, Kenji Nomura, Hiromichi Ohta, Hiroshi Yanagi, Masahiro Hirano, and Hideo Hosono, *Crystal growth & design* **6** (11), 2451 (2006).
- ²⁰ Kenji Nomura, Akihiro Takagi, Toshio Kamiya, Hiromichi Ohta, Masahiro Hirano, and Hideo Hosono, *Japanese journal of applied physics* **45** (5S), 4303 (2006).
- ²¹ S. R. Elliott, London: Longman (1990).
- ²² K Shimakawa, S Narushima, H Hosono, and H Kawazoe, *Philosophical magazine letters* **79** (9), 755 (1999).
- ²³ Toshio Kamiya, Kenji Nomura, and Hideo Hosono, *Display Technology* **5**, 462 (2009).
- ²⁴ Toshio Kamiya, Kenji Nomura, and Hideo Hosono, *Applied Physics Letters* **96** (12), 122103 (2010).
- ²⁵ Toshio Kamiya and Hideo Hosono, *NPG Asia Materials* **2** (1), 15 (2010).
- ²⁶ Toshio Kamiya, Kenji Nomura, and Hideo Hosono, *Science and Technology of Advanced Materials* **11** (4), 044305 (2010).
- ²⁷ G. Yerubandi D. Hong, H. Chiang, M. Spiegelberg, J. Wager, *Crit. Rev. Solid State Mater. Sci.* **33**, 101 (2008).

- ²⁸ Kenji Nomura, Toshio Kamiya, Hiroshi Yanagi, Eiji Ikenaga, Ke Yang, Keisuke Kobayashi, Masahiro Hirano, and Hideo Hosono, *Applied Physics Letters* **92** (20), 202117 (2008).
- ²⁹ Dieter K Schroder, *Semiconductor material and device characterization*. (John Wiley & Sons, 2006).
- ³⁰ Jeong-Min Lee, In-Tak Cho, Jong-Ho Lee, and Hyuck-In Kwon, *Applied Physics Letters* **93** (9), 093504 (2008).
- ³¹ Mami Fujii, Hiroshi Yano, Tomoaki Hatayama, Yukiharu Uraoka, Takashi Fuyuki, Ji Sim Jung, and Jang Yeon Kwon, *Japanese Journal of Applied Physics* **47** (8R), 6236 (2008).
- ³² Seok-Jun Seo, Chaun Gi Choi, Young Hwan Hwang, and Byeong-Soo Bae, *Journal of Physics D: Applied Physics* **42** (3), 035106 (2009).
- ³³ Kenji Nomura, Toshio Kamiya, Masahiro Hirano, and Hideo Hosono, *Applied Physics Letters* **95** (1), 013502 (2009).
- ³⁴ MJ Powell, C Van Berkel, ID French, and DH Nicholls, *Applied physics letters* **51** (16), 1242 (1987).
- ³⁵ Martin J Powell, *Electron Devices, IEEE Transactions on* **36** (12), 2753 (1989).
- ³⁶ Sang-Hee Ko Park, Doo-Hee Cho, Chi-Sun Hwang, Shinhyuk Yang, Min Ki Ryu, Chun-Won Byun, Sung Min Yoon, Woo-Seok Cheong, Kyoung Ik

- Cho, and Jae-Hong Jeon, *ETRI journal* **31** (6), 653 (2009).
- ³⁷ Jae-Heon Shin, Ji-Su Lee, Chi-Sun Hwang, Sang-Hee Ko Park, Woo-Seok Cheong, Minki Ryu, Chun-Won Byun, Jeong-Ik Lee, and Hye Yong Chu, *Etri Journal* **31** (1), 62 (2009).
- ³⁸ Andrei Kolmakov and Martin Moskovits, *Annu. Rev. Mater. Res.* **34**, 151 (2004).
- ³⁹ Zhiyong Fan, Dawei Wang, Pai-Chun Chang, Wei-Yu Tseng, and Jia G Lu, *Applied Physics Letters* **85** (24), 5923 (2004).
- ⁴⁰ Jae Kyeong Jeong, Hui Won Yang, Jong Han Jeong, Yeon-Gon Mo, and Hye Dong Kim, *Applied Physics Letters* **93** (12), 123508 (2008).
- ⁴¹ Kwang-Hee Lee, Ji Sim Jung, Kyoung Seok Son, Joon Seok Park, Tae Sang Kim, Rino Choi, Jae Kyeong Jeong, Jang-Yeon Kwon, Bonwon Koo, and Sangyun Lee, *Applied physics letters* **95** (23), 232106 (2009).
- ⁴² Te-Chih Chen, Ting-Chang Chang, Tien-Yu Hsieh, Wei-Siang Lu, Fu-Yen Jian, Chih-Tsung Tsai, Sheng-Yao Huang, and Chia-Sheng Lin, *Applied Physics Letters* **99** (2), 022104 (2011).
- ⁴³ Kwang Hwan Ji, Ji-In Kim, Hong Yoon Jung, Se Yeob Park, Rino Choi, Yeon Gon Mo, and Jae Kyeong Jeong, *Microelectronic Engineering* **88** (7), 1412 (2011).
- ⁴⁴ Byungki Ryu, Hyeon-Kyun Noh, Eun-Ae Choi, and KJ Chang, *Applied*

- physics letters **97** (2), 022108 (2010).
- ⁴⁵ Himchan Oh, Sung-Min Yoon, Min Ki Ryu, Chi-Sun Hwang, Shinhyuk Yang, and Sang-Hee Ko Park, Applied physics letters **97** (18), 183502 (2010).
- ⁴⁶ Hisato Yabuta, Masafumi Sano, Katsumi Abe, Toshiaki Aiba, Tohru Den, Hideya Kumomi, Kenji Nomura, Toshio Kamiya, and Hideo Hosono, Applied Physics Letters **89** (11) (2006).
- ⁴⁷ Jae Kyeong Jeong, Semiconductor Science and Technology **26** (3), 034008 (2011).
- ⁴⁸ Jae Kyeong Jeong, Jong Han Jeong, Hui Won Yang, Jin-Seong Park, Yeon-Gon Mo, and Hye Dong Kim, Applied Physics Letters **91** (11) (2007).
- ⁴⁹ J. S. Park H. D. Kim, Y. G. Mo, and S. S. Kim, Digest of Int. Meeting on Information Display, **35** (2009).
- ⁵⁰ W. T. Lin M. C. Hung, J. J. Chang, P. L. Chen, C. Y. Wu, C. J. Lin, H. L. and C. Y. Huang Chiu, and Y. C. Kao, Int. Workshop on Transparent Amorphous Oxide Semiconductor 2010, Tokyo, Japan (2010).
- ⁵¹ Jin-Seong Park, Tae-Woong Kim, Denis Stryakhilev, Jae-Sup Lee, Sung-Guk An, Yong-Shin Pyo, Dong-Bum Lee, Yeon Gon Mo, Dong-Un Jin,

- and Ho Kyoong Chung, *Applied Physics Letters* **95** (1) (2009).
- ⁵² E. Fortunato, P. Barquinha, A. Pimentel, L. Pereira, G. Gonçalves, and R. Martins, *physica status solidi (RRL) – Rapid Research Letters* **1** (1), R34 (2007).
- ⁵³ Lian Wang, Myung-Han Yoon, Gang Lu, Yu Yang, Antonio Facchetti, and Tobin J. Marks, *Nat Mater* **5** (11), 893 (2006).
- ⁵⁴ B. Yaglioglu, H. Y. Yeom, R. Beresford, and D. C. Paine, *Applied Physics Letters* **89** (6) (2006).
- ⁵⁵ C. Y. Kagan and P. W. E. Andry, *Dekker, New York Part I, Ch. 3* (2003).
- ⁵⁶ Jae-Heon Shin, Ji-Su Lee, Chi-Sun Hwang, Sang-Hee Park, Woo-Seok Cheong, Minki Ryu, Chun-Won Byun, Jeong-Ik Lee, and Hye Yong Chu, *ETRI Journal* **31** (1), 62 (2009).
- ⁵⁷ Md Delwar Hossain Chowdhury, Piero Migliorato, and Jin Jang, *Applied Physics Letters* **97** (17) (2010).
- ⁵⁸ Himchan Oh, Sung-Min Yoon, Min Ki Ryu, Chi-Sun Hwang, Shinhyuk Yang, and Sang-Hee Ko Park, *Applied Physics Letters* **98** (3) (2011).
- ⁵⁹ Kwang Hwan Ji, Ji-In Kim, Hong Yoon Jung, Se Yeob Park, Rino Choi, Un Ki Kim, Cheol Seong Hwang, Daeseok Lee, Hyungsang Hwang, and Jae Kyeong Jeong, *Applied Physics Letters* **98** (10) (2011).
- ⁶⁰ Byungki Ryu, Hyeon-Kyun Noh, Eun-Ae Choi, and K. J. Chang,

- Applied Physics Letters **97** (2) (2010).
- ⁶¹ Jong Han Jeong, Hui Won Yang, Jin-Seong Park, Jae Kyeong Jeong, Yeon-Gon Mo, Hye Dong Kim, Jaewon Song, and Cheol Seong Hwang, Electrochemical and Solid-State Letters **11** (6), H157 (2008).
- ⁶² John C. C. Fan and John B. Goodenough, Journal of Applied Physics **48** (8), 3524 (1977).
- ⁶³ T. Ishida, H. Kobayashi, and Y. Nakato, Journal of Applied Physics **73** (9), 4344 (1993).
- ⁶⁴ S. Major, Satyendra Kumar, M. Bhatnagar, and K. L. Chopra, Applied Physics Letters **49** (7), 394 (1986).
- ⁶⁵ Hyeon-Kyun Noh, K. J. Chang, Byungki Ryu, and Woo-Jin Lee, Physical Review B **84** (11), 115205 (2011).
- ⁶⁶ MR Pai, AM Banerjee, SR Bharadwaj, and SK Kulshreshtha, Journal of materials research **22** (07), 1787 (2007).
- ⁶⁷ Stephan Lany and Alex Zunger, Physical Review B **72** (3), 035215 (2005).
- ⁶⁸ Anderson Janotti and Chris G. Van de Walle, Physical Review B **76** (16), 165202 (2007).
- ⁶⁹ O. García-Martínez, R. M. Rojas, E. Vila, and J. L. Martín de Vidales, Solid State Ionics **63–65** (0), 442 (1993).

- ⁷⁰ Toshihiro Moriga, Doreen D Edwards, Thomas O Mason, George B Palmer, Kenneth R Poeppelmeier, Jon L Schindler, Carl R Kannewurf, and Ichiro Nakabayashi, *Journal of the American Ceramic Society* **81** (5), 1310 (1998).
- ⁷¹ Shye Lin Wu, Chung Len Lee, Tan Fu Lei, JF Chen, and LJ Chen, *Electron Device Letters, IEEE* **15** (5), 160 (1994).
- ⁷² Min Cao, P Vande Voorde, Mike Cox, and Wayne Greene, *Electron Device Letters, IEEE* **19** (8), 291 (1998).
- ⁷³ B. L. Doyle, P. S. Peercy, J. D. Wiley, J. H. Perepezko, and J. E. Nordman, *Journal of Applied Physics* **53** (9), 6186 (1982).
- ⁷⁴ Shinhyuk Yang, Kwang Hwan Ji, Un Ki Kim, Cheol Seong Hwang, Sang-Hee Ko Park, Chi-Sun Hwang, Jin Jang, and Jae Kyeong Jeong, *Applied Physics Letters* **99** (10) (2011).
- ⁷⁵ Bong Seob Yang, Sanghyun Park, Seungha Oh, Yoon Jang Kim, Jae Kyeong Jeong, Cheol Seong Hwang, and Hyeong Joon Kim, *Journal of Materials Chemistry* **22** (22), 10994 (2012).
- ⁷⁶ TI Kamins, J Manoliu, and RN Tucker, *Journal of Applied Physics* **43** (1), 83 (1972).
- ⁷⁷ Kenji Nomura, Toshio Kamiya, Hiromichi Ohta, Tomoya Uruga, Masahiro Hirano, and Hideo Hosono, *Physical review B* **75** (3), 035212

(2007).

- ⁷⁸ Hideyuki Omura, Hideya Kumomi, Kenji Nomura, Toshio Kamiya, Masahiro Hirano, and Hideo Hosono, *Journal of Applied Physics* **105** (9), 093712 (2009).
- ⁷⁹ W-J Lee, B Ryu, and KJ Chang, *Physica B: Condensed Matter* **404** (23), 4794 (2009).
- ⁸⁰ Hisato Yabuta, Masafumi Sano, Katsumi Abe, Toshiaki Aiba, Tohru Den, Hideya Kumomi, Kenji Nomura, Toshio Kamiya, and Hideo Hosono, *Applied physics letters* **89**, 112123 (2006).
- ⁸¹ Jae Kyeong Jeong, *Journal of Materials Research* **28** (16), 2071 (2013).
- ⁸² A. Suresh and J. F. Muth, *Applied Physics Letters* **92** (3), 033502 (2008).
- ⁸³ Jang-Yeon Kwon, Ji Sim Jung, Kyoung Seok Son, Kwang-Hee Lee, Joon Seok Park, Tae Sang Kim, Jin-Seong Park, Rino Choi, Jae Kyeong Jeong, Bonwon Koo, and Sang Yoon Lee, *Applied Physics Letters* **97** (18), 183503 (2010).
- ⁸⁴ Kwang Hwan Ji, Ji-In Kim, Yeon-Gon Mo, Jong Han Jeong, Shinhyuk Yang, Chi-Sun Hwang, Sang-Hee Ko Park, Myung-Kwan Ryu, Sang-Yoon Lee, and Jae Kyeong Jeong, *IEEE electron device letters* **31** (12), 1404 (2010).
- ⁸⁵ Bong Seob Yang, Sanghyun Park, Seungha Oh, Yoon Jang Kim, Jae

- Kyeong Jeong, Cheol Seong Hwang, and Hyeong Joon Kim, *Journal of Materials Chemistry* **22** (22), 10994 (2012).
- ⁸⁶ Jae Kyeong Jeong, Hui Won Yang, Jong Han Jeong, Yeon-Gon Mo, and Hye Dong Kim, *Applied Physics Letters* **93** (12), 123508 (2008).
- ⁸⁷ Shinhyuk Yang, Doo-Hee Cho, Min Ki Ryu, Sang-Hee Ko Park, Chi-Sun Hwang, Jin Jang, and Jae Kyeong Jeong, *Applied Physics Letters* **96** (21), 213511 (2010).
- ⁸⁸ Kenji Nomura, Toshio Kamiya, and Hideo Hosono, *Applied Physics Letters* **99** (5), 053505 (2011).
- ⁸⁹ Joon Seok Park, Tae Sang Kim, Kyoung Seok Son, Kwang-Hee Lee, Wan-Joo Maeng, Hyun-Suk Kim, Eok Su Kim, Kyung-Bae Park, Jong-Baek Seon, and Woong Choi, *Applied Physics Letters* **96** (26), 262109 (2010).
- ⁹⁰ Himchan Oh, Sung-Min Yoon, Min Ki Ryu, Chi-Sun Hwang, Shinhyuk Yang, and Sang-Hee Ko Park, *Applied physics letters* **97** (18), 183502 (2010).
- ⁹¹ Byungki Ryu, Hyeon-Kyun Noh, Eun Choi, and KJ Chang, *Applied physics letters* **97** (2), 022108 (2010).
- ⁹² Yoon Jang Kim, Bong Seob Yang, Seungha Oh, Sang Jin Han, Hong Woo Lee, Jaeyeong Heo, Jae Kyeong Jeong, and Hyeong Joon Kim, *ACS*

- applied materials & interfaces **5** (8), 3255 (2013).
- ⁹³ Khashayar Ghaffarzadeh, Arokia Nathan, John Robertson, Sangwook Kim, Sanghun Jeon, Changjung Kim, U-In Chung, and Je-Hun Lee, *Applied Physics Letters* **97** (14), 143510 (2010).
- ⁹⁴ Kwang Hwan Ji, Ji-In Kim, Hong Yoon Jung, Se Yeob Park, Rino Choi, Un Ki Kim, Cheol Seong Hwang, Daeseok Lee, Hyungsang Hwang, and Jae Kyeong Jeong, *Applied Physics Letters* **98** (10), 103509 (2011).
- ⁹⁵ Hyeon-Kyun Noh, KJ Chang, Byungki Ryu, and Woo-Jin Lee, *Physical Review B* **84** (11), 115205 (2011).
- ⁹⁶ Himchan Oh, Sang-Hee Ko Park, Chi-Sun Hwang, Shinhyuk Yang, and Min Ki Ryu, *Applied Physics Letters* **99** (2), 022105 (2011).
- ⁹⁷ Seungha Oh, Bong Seob Yang, Yoon Jang Kim, Myeong Sook Oh, Mi Jang, Hoichang Yang, Jae Kyeong Jeong, Cheol Seong Hwang, and Hyeong Joon Kim, *Applied Physics Letters* **101** (9), 092107 (2012).
- ⁹⁸ Md Delwar Hossain Chowdhury, Piero Migliorato, and Jin Jang, *Applied Physics Letters* **98** (15), 153511 (2011).
- ⁹⁹ S. G J Mathijssen, M. Cölle, H. Gomes, E. C P Smits, B. de Boer, I. McCulloch, P. A Bobbert, and D. M de Leeuw, *Advanced Materials* **19** (19), 2785 (2007).
- ¹⁰⁰ Paul Erhart and Karsten Albe, *Applied Physics Letters* **88** (20), 201918

(2006).

- ¹⁰¹ Koji Kusunoki, Makoto Kaneyasu, Hikaru Harada, Haruki Katagiri, Koji Moriya, Hideto Ohnuma, Yoshiharu Hirakata, Jun Koyama, Shunpei Yamazaki, Yukinori Shima, and Daisuke Kurosaki, SID Symposium Digest of Technical Papers **43** (1), 217 (2012).
- ¹⁰² T. K. Gupta and W. G. Carlson, J Mater Sci **20** (10), 3487 (1985).
- ¹⁰³ Anderson Janotti and Chris G Van de Walle, Journal of crystal growth **287** (1), 58 (2006).
- ¹⁰⁴ Keunhyung Park, Shubneesh Batra, Sanjay Banerjee, Gayle Lux, and T. C. Smith, Journal of Applied Physics **70** (3), 1397 (1991).
- ¹⁰⁵ Dong Hee Lee, Ken-ichi Kawamura, Kenji Nomura, Toshio Kamiya, and Hideo Hosono, Electrochemical and Solid-State Letters **13** (9), H324 (2010).
- ¹⁰⁶ Ho-Hyun Nahm, Yong-Sung Kim, and Dae Hwan Kim, physica status solidi (b) **249** (6), 1277 (2012).
- ¹⁰⁷ Aron Walsh, Juarez LF Da Silva, and Su-Huai Wei, Chemistry of Materials **21** (21), 5119 (2009).
- ¹⁰⁸ Tatsuya Eguchi, Hiroyuki Inoue, Atsunobu Masuno, Koji Kita, and Futoshi Utsuno, Inorganic chemistry **49** (18), 8298 (2010).

List of publication

1. Journals (SCI)

1. Myung Soo Huh, Bong Seop Yang, **Seungha Oh**, Joohei Lee, Kapsuo Yoon, Jae Kyeong Jeong, Cheol Seong Hwang, and Hyeong Joon Kim, “Improvement in the Performance of Tin Oxide Thin film Transistors by Alumina Doping”, *Electrochem. Solid-State Lett.*, **12**(10) H385-H387 (2009).
2. Myung Soo Huh, Bong Seop Yang, **Seungha Oh**, Jeong-hwan Kim, Je-Hun Lee, Jae Kyeong Jeong, Cheol Seong Hwang, and Hyeong Joon Kim, “Improving the performance of tin oxide thin film transistors by using ultralow-pressure sputtering”, *J. Electrochem. Soc.*, **157**(4) H425-H429 (2010).
3. Myung Soo Huh, Seok-Jun Won, Bong Seop Yang, **Seungha Oh**, Myeong Sook Oh, Jae Kyeong Jeong, and Hyeong Joon Kim, “Improving the performance of thin film transistors with ZnO channel layer fabricated by ultralow-pressure sputtering”, *J. Vac. Sci. Technol.*, B, **29**, 031201 (2011)
4. Bong Seob Yang, Myung Soo Huh, **Seungha Oh**, Ung Soo Lee, Yoon Jang Kim, Myeong Sook Oh, Jae Kyeong Jeong, Cheol Seong Hwang, and Hyeong Joon Kim, “ Role of ZrO₂ incorporation in the suppression of negative bias illumination-induced instability in Zn-Sn-O thin film transistors”, *Appl. Phys. Lett.* **98**, 122110 (2011).
5. Bong Seob Yang, Sanghyun Park, **Seungha Oh**, Yoon Jang Kim, Jae Kyeong Jeong, Cheol Seong Hwang and Hyeong Joon Kim, “Improvement of the photo-bias stability of the Zn–Sn–O field effect transistors by an ozone treatment”, *J. Mater. Chem.*, **22**, 10994-10998 (2012)

6. **Seungha Oh**, Bong Seob Yang, Yoon Jang Kim, Myeong Sook Oh, Mi Jang, Hoichang Yang, Jae Kyeong Jeong, Cheol Seong Hwang, and Hyeong Joon Kim, “Anomalous behavior of negative bias illumination stress instability in an indium zinc oxide transistor: a cation combinatorial approach”, *Appl. Phys. Lett.*, **101**, 092107 (2012)
7. Yoon Jang Kim, Bong Seob Yang, **Seungha Oh**, Sang Jin Han, Hong Woo Lee, Jaeyeong Heo, Jae Kyeong Jeong, and Hyeong Joon Kim, “Photobias Instability of High Performance Solution Processed Amorphous Zinc Tin Oxide Transistors”, *ACS Appl. Mater. Interfaces*, **5**, 3255–3261 (2013)
8. Bong Seob Yang, **Seungha Oh**, Yoon Jang Kim, Sang Jin Han, Hong Woo Lee, Hyuk Jin Kim, Hui Kyung Park, Jae Kyeong Jeong, Jaeyeong Heo, Cheol Seong Hwang, and Hyeong Joon Kim, “Effect of sputter power on the photobias stability of zinc-tin-oxide field-effect transistors”, *J. Vac. Sci. Technol., B*, **32**, 011202 (2014)
9. **Seungha Oh**, Bong Seob Yang, Yoon Jang Kim, Un Ki Kim, Sang Jin Han, Hong Woo Lee, Hyuk Jin Kim, Sung Min Kim, Jae Kyeong Jeong, and Hyeong Joon Kim, “Dynamics of negative bias thermal stress-induced threshold voltage shifts in indium zinc oxide transistors: impact of the crystalline structure on the activation energy barrier”, *J. Phys. D: Appl. Phys.*, **47**, 165103 (2014)
10. Bong Seob Yang, **Seungha Oh**, Yoon Jang Kim, Sang Jin Han, Hong Woo Lee, Hyuk Jin Kim, Sungmin Kim, Hui Kyung Park, Jaeyeong Heo, Jae Kyeong Jeong, and Hyeong Joon Kim, “The Anomalous Effect of Oxygen Ratio on the Mobility and Photobias Stability of Sputtered Zinc–Tin–Oxide Transistors”, *IEEE Trans. Electron Devices*, **61**, 2071 (2014)

11. Bong Seob Yang, **Seungha Oh**, Yoon Jang Kim, Sang Jin Han, Hong Woo Lee, Hyuk Jin Kim, Sungmin Kim, Hui Kyung Park, Jaeyeong Heo, Jae Kyeong Jeong, Cheol Seong Hwang and Hyeong Joon Kim, “Effect of sputter power on the photobias stability of zinc-tin-oxide field-effect transistors”, *J. Vac. Sci. Technol.*, B, **32**, 011202 (2014)

12. Yoon Jang Kim, **Seungha Oh**, Bong Seob Yang, Sang Jin Han, Hong Woo Lee, Hyuk Jin Kim, Jae Kyeong Jeong, Cheol Seong Hwang, and Hyeong Joon Kim, “Impact of the cation composition on the electrical performance of solution-processed zinc tin oxide thin film transistors”, *ACS Appl. Mater. Interfaces*, **6**, 14026 (2014)

13. Hong Woo Lee, Bong Seob Yang, Yoon Jang Kim, **Seungha Oh**, Jong Hwan Lee, Jae Kyeong Jeong, and Hyeong Joon Kim, “Comprehensive studies on the carrier transporting property and photo-bias instability of sputtered zinc tin oxide thin film transistors”, *IEEE Trans. Electron Devices*, **61**, 3191 (2014)

2. Proceeding

1. Myung Soo Huh, Bong Sop Yang, **Seungha Oh**, Seok Jun Won, Jae Kyeong Jeong, Cheol Seong Hwang, and Hyeong Joon Kim, “Improvement in the Device Characteristics of Tin Oxide Thin film Transistors by Adopting Ultralow-Pressure Sputtering”, Electrochemical Society, 5-9 October 2009, Vienna, Austria.

2. Myung Soo Huh, Bong Sop Yang, **Seungha Oh**, and Hyeong Joon Kim, “Aluminum doped Tin Oxide based Thin Film Transistors”, The 6th international tin-film transistor conference, 28-29 January, Egret Himeji, Japan.

3. Myung Soo Huh, Bong Seob Yang, **Seungha Oh**, Seok-Jun Won, Sang Jin Han,

Cheoi Lae Roh, and Hyeong Joon Kim, “The surface morphological and electrical properties of ultralow-pressure sputtered tin doped indium oxide film”, 2010 53rd SVC annual technical conference, 17-22 April, Orland, Florida, USA.

4. Bong Seob Yang, **Seungha Oh**, Yoon Jang Kim, and Hyeong Joon Kim, “Improvement of the photo-bias stability of the Zn-Sn-O field effect transistors by an ozone treatment”, ECS 222nd Meeting, 7-12 October 2012, Honolulu, Hawaii.
5. **Seungha Oh**, Bong Seob Yang, Yoon Jang Kim, and Hyeong Joon Kim, “Composition Dependence of the Negative Bias Light Illumination Instability of Indium Zinc Oxide Transistors”, ECS 222nd Meeting, 7-12 October 2012, Honolulu, Hawaii.

3. Conferences

3.1 International

1. Myung Soo Huh, Bong Sop Yang, **Seungha Oh**, Seok-Jun Won, Jae Kyung Jeong, Cheol Seong Hwang, and Hyeong Joon Kim, “Aluminum Oxide Doped Tin Oxide Thin Film Transistors”, AVS-MPA, 21-23 July 2009, Manchester, United Kingdom.
2. Myung Soo Huh, Bong Sop Yang, **Seungha Oh**, Je-Hun Lee, and Hyeong Joon Kim, “Improved Electrical Properties of Sputtered Tin Oxide Films as the Active Layer of Thin Film Transistor”, ICMAP 2009, 20-25 September 2009, Busan, Korea.
3. Myung Soo Huh, Bong Sop Yang, **Seungha Oh**, Seok-Jun Won, Jae Kyung

- Jeong, Cheol Seong Hwang, and Hyeong Joon Kim, "Improvement in the Device Characteristics of Tin Oxide Thin-film Transistors by Adopting Ultralow-Pressure Sputtering", Electrochemical Society, 5-9 October 2009, Vienna, Austria.
4. Myung Soo Huh, Bong Sop Yang, **Seungha Oh**, and Hyeong Joon Kim, "Aluminum doped Tin Oxide based Thin Film Transistors", The 6th international tin-film transistor conference, 28-29 January, Egret Himeji, Japan.
 5. Myung Soo Huh, Bong Sop Yang, **Seungha Oh**, Seok-Jun Won, Sang Jin Han, Cheoi Lae Roh, and Hyeong Joon Kim, "The surface morphological and electrical properties of ultralow-pressure sputtered tin doped indium oxide film", 2010 53rd SVC annual technical conference, 17-22 April, Orland, Florida, USA.
 6. Bong Seob Yang, Myung Soo Huh, **Seungha Oh**, and Hyeong Joon Kim, "Influence of post-annealing conditions on the performances of zinc tin oxide thin-film transistors", 2010 53rd SVC annual technical conference, 17-22 April, Orland, Florida, USA.
 7. Bong Seob Yang, Myung Soo Huh, **Seungha Oh**, Byung Du Ahn, J. Lee, Jong Hoon Kim, and Hyeong Joon Kim, "Influence of channel thickness of zinc tin oxide films on the performances of thin-film transistors", The 7th AMF-AMEC, June 28- July 1, 2010, Je-ju, Korea.
 8. Myung Soo Huh, Bong Seob Yang, **Seungha Oh**, Byung Du Ahn, J. Lee, Jong Hoon Kim, and Hyeong Joon Kim, "Improved Surface Morphological Properties of Indium Tin Oxide films by Using Ultralow-pressure Sputtering Process" The 7th AMF-AMEC, June 28- July 1, 2010, Je-ju, Korea.
 9. **Seungha Oh**, Myung Soo Huh, Bong Seob Yang, Hyeong Joon Kim, "Influence of annealing temperature, Zn/Sn ratio and O₂ partial pressure on the performances

of zinc tin oxide thin-film transistors”, IUMRS-ICEM 2010, 22-27 August 2010, KINTEX, KOREA. (Poster)

10. Yoon Jang Kim, Bong Seob Yang, **Seungha Oh**, Jae Kyeong Jeong, Hyeong Joon Kim, “Effect of Annealing Temperature on the Electrical Characteristics of Solution Processed Zinc Tin Oxide Thin Film Transistors” Electrochemical Society 221th Meeting, 6-11 May 2012, Seattle, USA.
11. **Seungha Oh**, Bong Seob Yang, Yoon Jang Kim, and Hyeong Joon Kim, “Composition Dependence of the Negative Bias Light Illumination Instability of Indium Zinc Oxide Transistors”, Electrochemical Society 222th Meeting, 7-12 October 2012, Honolulu, Hawaii.
12. Bong Seob Yang, **Seungha Oh**, Yoon Jang Kim, and Hyeong Joon Kim, “Improvement of the photo-bias stability of the Zn-Sn-O field effect transistors by an ozone treatment”, Electrochemical Society 222th Meeting, 7-12 October 2012, Honolulu, Hawaii.
13. Yoon Jang Kim, Bong Seob Yang, Jong Ho Lee, **Seungha Oh**, Sang Jin Han, Hong Woo Lee, Jae Kyeong Jeong and Hyeong Joon Kim, “Negative bias illumination stress instability of solution processed amorphous zinc tin oxide transistors”, Latin Display 2012/IDRC 2012, 26-30 November 2012, Sao Paulo, Brazil.
14. **Seungha Oh**, Bong Seob Yang, Yoon Jang Kim, Sang Jin Han, Hong Woo Lee, Hyuk Jin Kim, and Hyeong Joon Kim, “Analysis for the hole migration behavior in InZnO thin film transistors using a stretched exponential fitting method”, Material Research Society, 6-6 December 2013, Boston, USA.
15. Yoon Jang Kim, Bong Seob Yang, **Seungha Oh**, Hyuk Jin Kim, and Hyeong

Joon Kim, “Photo-bias Instability of Solution Processed Zinc Tin Oxide Thin Film Transistors with Varying Zn:Sn Composition Ratio”, International Conference on Small Science, 15-18 December 2013, Las Vegas, USA.

3.2 Domestic

1. **Seungha Oh**, Bong Seob Yang, Yoon Jang Kim and Hyeong Joon Kim, “Indium 함량에 따른 Indium Zinc Oxide (IZO) transistor의 소자 특성 및 IZO 박막의 특성 변화”, The 2nd Semiconductor and Display Jeju Forum, 10-11 May 2012, Jeju Nat’l Univ., Korea.
2. **Seungha Oh**, Bong Seob Yang, Yoon Jang Kim, Sang Jin Han, Hong Woo Lee and Hyeong Joon Kim, “Composition Dependence of the Negative Bias Illumination Stress Instability of Indium Zinc Oxide Transistors”, The 3rd Semiconductor and Display, 10 October 2013, KINTEX, Korea.
3. **Seungha Oh**, Bong Seob Yang, Yoon Jang Kim, Sang Jin Han, Hong Woo Lee and Hyeong Joon Kim, “Reliability analysis for IZO TFTs by stretched exponential fitting”, The 4th Semiconductor and Display, 31 May 2013, Korea.

Abstract (in Korean)

In_2O_3 를 기반으로 하는 산화물 박막트랜지스터 (thin film transistor, TFT)는 상당히 높은 소자 이동도 ($\mu_{\text{FE}} > 30 \text{ cm}^2/\text{Vs}$)와 대면적 기판에서의 전기적 균일성, 낮은 공정 온도와 같은 장점들을 바탕으로 AMLCDs (active matrix liquid crystal displays), OLEDs (organic light emitting diodes), 유연성 디스플레이의 구동 소자로 널리 연구되고 있다. 이러한 In_2O_3 기반 산화물 TFT의 제작과 그 높은 이동도는 많이 보고되어 있지만, 본 연구에서 다룬 In-Zn-O (IZO) TFT의 광전압 신뢰성에 대해서는 별로 알려진 바가 없고, 채널막의 결정성이 광전압 신뢰성에 미치는 영향에 대해서도 연구된 바가 없었다.

이 논문에서는 다양한 In 조성에 대해 IZO TFT의 광전압 신뢰성을 평가하고, 또한 채널막의 결정성이 신뢰성에 주는 영향에 대해 깊이 있게 연구하였다.

두 개 타겟의 동시 스퍼터링을 통해 다양한 조성의 IZO 채널막을 증착, 높은 성능의 TFT를 제작하였고, 기본적인 소자 성능뿐만 아니라 negative bias illumination stress (NBIS) 신뢰성 특성을 확인하였다. In 함량 0에서 85 at.%로 증가하면서 소자 이동도와 sub-threshold swing (S.S)는 1.1에서 $41.0 \text{ cm}^2/\text{Vs}$ 로, 2.4에서 0.2 V/decade 로 크게 향상되었다. 그러한 소자 성능의 향상은 IZO 박막의 홀 (Hall) 측정 결과와도 큰

연관성을 보였다. In 함량 16 at.%을 제외하고는 In 함량이 증가할수록 전자 농도와 홀 이동도가 따라서 증가하였다. 전반적으로 전자농도와 홀 이동도의 증가는 산소 공공과 박막내 In 비율의 증가에 의존하였지만 16 at.% 조건의 경우는 ZnO에 In이 dopant로써 존재해서 그러한 구조적, 전기적 특성이 두드러졌다. NBIS 신뢰성 특성에서는 채널막이 다결정 구조에서 비정질 구조로 변화하는 과정에서 비롯된 특이한 결과가 관찰되었다. 우선 In 함량이 60 at.% 미만에서는 다결정 구조가 유지되었고, In 함량이 증가함에 따라 음의 게이트 전압 방향으로 threshold voltage (V_{th}) 이동이 증가하였다. 특히 원주형의 결정립 구조, 결정립계들이 전계에 의한 이온화된 산소 공공의 이동을 촉진시켰고, 결정립의 크기가 줄어들면서 넓어진 결정립계는 NBIS 신뢰성 특성을 더욱 악화시켰다. 반면에 In 함량 75 at.% 정도에서는 다결정 구조에서 비정질 구조로 변화하면서 V_{th} 이동이 최소화되었다. 이러한 결과는 빛에 의해 이온화된 산소 공공의 이동과정이 V_{th} 불안정성을 결정하는데 매우 중요한 역할을 한다는 것을 의미하며, 결정립계나 원주형 결정립 구조가 없는 경우가 IZO TFT의 더 나은 광전압 신뢰성을 확보하는데 유리하다고 할 수 있다. 75 at.% 이상으로 더욱더 In을 첨가할 시에는 산소 공공의 증가로 다시 소자 신뢰성이 크게 열화되었다.

채널막의 결정 구조와 V_{th} 불안정성 사이의 관계를 stretched exponential 피팅 기법을 통해 다시 한번 고찰하였다. 다결정 구조에서

비정질 구조로 변화가 일어나는 In 함량 52~77at.% 범위의 세가지 조성의 소자에 대해서 온도에 의존적인 V_{th} 이동에 대한 activation energy를 계산하였다. 다결정 구조의 경우 1.40 eV, 비정질의 경우 2.04 eV로 더 큰 값을 보였고, 다결정 보다 비정질 구조에서 산소 공공의 이동에 대한 에너지가 더 많이 필요함을 나타낸다. 그리고 activation energy 차이 0.64 eV는 이온화된 산소 공공의 이동하는 통로가 다른 것에서 기인하였으며 채널막 내부의 결정립계의 존재는 산화물 TFT의 신뢰성을 열화시킬 수 있음을 다시 한번 확인하였다. 한편, 열화된 V_{th} 의 회복 과정에서는 채널의 결정구조와는 관계없이 0.75 eV 정도로 서로 비슷한 activation energy 값을 보였다. 이를 토대로 회복 과정은 이온화된 산소 공공의 중성화 반응으로 이루어짐을 확인하였다.

Keywords : Indium Zinc Oxide (IZO), 박막트랜지스터, 광전압 신뢰성, negative bias illumination stress (NBIS), 결정립계, 결정 구조, In 함량, 스퍼터링

Student ID : 2009-20617

Seungha Oh